Low Temperature Electrodeposition of Epitaxial Films of Covalent Semiconductors

by

Joshua J. DeMuth

A dissertation submitted in partial fulfillment
of the requirements for the degree of
Doctor of Philosophy
(Chemistry)
in the University of Michigan
2018

Doctoral Committee:

Professor Stephen Maldonado, Chair
Professor Cagliyan Kurdak
Professor Adam Matzger
Professor Dominika Zgid

Joshua DeMuth
demuthj@umich.edu
ORCID iD:0000-0003-1516-6422

© Joshua DeMuth 2018

ACKNOWLEDGEMENTS

I thank my parents, family, friends, co-workers and mentors for their support and encouragement. I also express my gratitude to my parents, older siblings and brother-in-law for being outstanding role models. They provided me with invaluable advice that ultimately shaped my decision to pursue this degree.

TABLE OF CONTENTS

ACKNOWLEDGEMENTS ii
LIST OF FIGURES v
LIST OF TABLES xiv
ABSTRACT xv
CHAPTER 1. Introduction **1**
- A.Background 1
- B.Crystal Growth Methods for Covalent Semiconductors 2
- C.Aqueous Electrodeposition of Covalent Semiconductors 4
- D.ec-LLS Growth of Covalent Semiconductors 5
- E.Thesis Objectives and Content Description 7
- F.References 9

CHAPTER 2. Controlling Nucleation and Crystal Growth of Ge in a Liquid Metal Solvent **11**
- A.Introduction 11
- B.Methods 14
- C.Results 21
- D.Discussion 28
- E.Conclusion 36
- F.References 37

CHAPTER 3. Electrochemical Liquid Phase Epitaxy (ec-LPE): A New Methodology for the Synthesis of Crystalline Group IV Semiconductor Epifilms **39**
- A.Introduction 39
- B.Methods 41
- C.Results 46

D.Discussion....55
E.Conclusion....61
F.References....61
CHAPTER 4. Eutectic-Bismuth Indium as a Low Melting Point Liquid Metal for Electrochemical Liquid-Liquid-Solid Growth of Germanium Microwires and Coiled Nanowires 64
A.Introduction....64
B.Methods....65
C.Results....71
D.Discussion....83
E.Conclusion....89
F.References....90
CHAPTER 5. Electrochemical Liquid-Liquid-Solid Deposition of Crystalline Gallium Antimonide....92
A.Introduction....92
B.Methods....93
C.Results....95
D.Discussion....107
E.Conclusion....113
F.References....114
CHAPTER 6. Conclusions and Future Work....116
A.Conclusions....116
B.Ongoing Work....118
i.*Si ec-LPE*....118
ii.*GaSb ec-LPE*....124
C.References....134

LIST OF FIGURES

Figure 1.1 Schematics depict strategies for growing covalent semiconductor crystals. a) Growth occurs at high temperature to promote fast surface mobilities and b) Growth occurs in a fluid phase where a reversible pathway between solid and solution phase is developed. 3

Figure 1.2. Schematic of electrochemical liquid-liquid solid (ec-LLS) growth. 1) electrochemical reduction of ionic precursor, 2) dissolution of zero valent species, 3) homogeneous nucleation and 4)growth of covalent semiconductor. 6

Figure 2.1. Microwells patterned in photoresist on n^+-Si(100) (a) before and (b) after filling the with e-GaIn. (c) Schematic depiction of ec-LLS inside a shallow microwell filled with liquid metal. Solute can reach the bottom interface and preferentially nucleate and grow a crystal heterogeneously. (d) Same as in (c) except the microwell is sufficiently deep enough that no solute reaches the bottom interface and instead preferentially nucleates and grows crystals homogeneously within the liquid metal. 12

Figure 2.2. Calculated liquidus curve for Ge dissolved in e-GaIn using eq 7. Plots are shown on scale of Temperature vs Mole Fraction Ge (a) and Temperature vs Mole Fraction Ge x 10^{-3}. ...18

Figure 2.3 The activity coefficient as a function of the supersaturation of Ge on E-GaIn at T= 40 ºC, 60 ºC and 80 ºC 20

Figure 2.4. (a) Current–time data recorded for Ge ec-LLS experiments performed at E = −1.6 V and at T = 40, 60, and 80 °C in aqueous solution containing 50 mM GeO_2 and 10 mM $Na_2B_4O_7$. (b) Measured dependence of mass vs total charge passed at E = −1.6 V and at T = 40, 60, and 80 °C. 22

Figure 2.5. (a) (a) Scanning electron micrograph and EDS elemental map of a 8 μm and 27 μm liquid metal thickness at T = 80 ºC. (b) Scanning electron micrographs and EDS map of Ge ec-LLS experiments Scanning electron micrographs of Ge ec-LLS experiments performed in the same electrolyte as in Figure 2.4 at E_{appl} = −1.6 V for 30 min at T = 40, 60, and 80 °C and with

several e-GaIn thicknesses. In each pair, the scale bar for the left image is 10 μm and for the right image is 2 μm.. 23

Figure 2.6. (a–d) Cross sectional scanning electron micrographs after Ge ec-LLS performed in the same electrolyte as in Figure 2.4 with a liquid metal thickness of 8 μm, $E = -1.6$ V, and for either (a) 3 min, (b) 5 min, (c) 10 min, and (d) 30 min. (e) Powder X-ray diffractograms of the Ge(111) signal measured for samples at various times (indicated to the right of the trace). (Inset) A calibration plot for the integrated intensity of the Ge(111) diffraction signal as a function of Ge mass....25

Figure 2.7. (a) Integrated intensity of the Ge(111) diffraction signal as a function of the duration of the ec-LLS experiment. The conditions for each ec-LLS experiment are the same as in Figure 2.4 Each dashed line represents the linear least-squares best fit. The slopes from (a) for data collected at E = -1.6 V are plotted as a function of reciprocal temperature (b) 27

Figure 2.8. (a–c) The concentration of dissolved Ge in the liquid metal at every position inside an 8 μm thick film of E-GaIn at several times as predicted by a 1D finite difference model of diffusional transport at T = 80 °C and a flux of Ge into e-GaIn of 1.82×10^{-8} mol s^{-1} cm^{-2}. The y-axis shows the concentration both in units of supersaturation and driving force. The value of 0 μm on the x-axes corresponds to the E-GaIn/Si(100) substrate interface. The value of 8 μm corresponds to the electrolyte/E-GaIn interface. The profiles are shown for (a) 0.001 s, (b) 0.1 s, and (c) 10 s after the start of the Ge ec-LLS experiment. (d) A plot of the predicted supersaturation-time dependences for Ge ec-LLS experiments at the E-GaIn/Si(100) interface for T = 40, 60, and 80 °C under the experimental conditions described in Figure 2.3. The experimentally measured x-axis intercepts from Figure 2.6 are superimposed on each curves corresponding to the respective experimental conditions. 30

Figure 2.9. Calculated driving force for Ge nucleation at the top of the e-GaIn film when the driving force for Ge nucleation at the bottom E-GaIn/Si(100) interface is sufficient for heterogeneous nucleation. The values shown were determined through a 1D finite difference model of diffusional transport at each temperature, liquid metal thickness, and flux condition explored in Figure 2.4. 32

Figure 2.10. Concentration gradients at different time points throughout the simulation for Ge ec-LLS at T = 80 ºC with a thickness of 20 μm. Three different general time regions were chosen near nucleation (a) and after nucleation (b). The concentration of Ge in a 20 μm thick volume of e-GaIn at the liquid metal /substrate interface is plotted as a function of time for simulations implementing boundary conditions *eq 11* for T = (c) 40 ºC and (d) 80 ºC....25

Figure 3.1. (a) Summary view of an electrochemical liquid phase epitaxy (ec-LPE) film growth concept with a thin liquid metal electrode with thickness h. (b) Schematic depiction of the relevant steps in ec-LPE, where an oxidized species X^{n+} dissolved in the electrolyte is reduced to X^0 by heterogeneous electron transfer, partitions into the liquid metal film, and then diffuses some distance away from the liquid electrolyte/liquid metal interface before precipitating out. When h is sufficiently thin, preferential heterogeneous nucleation and crystal growth is possible at the bottom interface between the liquid metal and a seed substrate. 40

Figure 3.2. Schematic of the initial ec-LPE cell design (a, b). The cell was designed to form a liquid metal film electrode over a macroscopic area of an underlying substrate. Cross section of ec-LPE cell (b) where; 1) Compression plate (two-piece membrane), 2) Compression spacer, 3) Ga(l) channels, 4) Ohmic contact, 5) Cavity space above substrate filled with Ga(l) 43

Figure 3.3. (a) Exploded view of the ec-LPE cell developed for this work. The cell has a compression stack design to facilitate the formation of a stable liquid metal film over a large two-dimensional area. Upon assembly, liquid metal is flowed into a thin cavity with the side walls and bottom defined by photoresist patterned on a seed substrate, respectively, and the top comprised of a porous membrane that is permeable to electrolyte flow but resists infusion by the liquid metal. (b)Optical photograph of an ec-LPE cell for film areas ~ 4.8 cm^2. 44

Figure 3.4. ((a) Representative chronoamperometric trace of an ec-LPE deposition of a Ge film with the cell described in Figure 3.3 and the following conditions: $E = -1.6$ V vs E(Ag/AgCl), $T =$ 90 °C, and an aqueous electrolyte containing 70 mM $Na_2B_4O_7$ and dissolved GeO_2 at a formal concentration of 225 mM. (b) Optical photograph of a Ge film prepared by ec-LPE with the same conditions as in (a) on top of a n^+-Si(100) seed substrate. (c) Representative scanning confocal laser interferometry image depicting the surface roughness of the top of an as-prepared Ge film by ec-LPE with the same conditions as in (a). (d) Scanning electron micrograph of a cross-section of a Ge film prepared by ec-LPE with the same conditions as in (a). The underlying seed substrate is n^+-Si(100). (e) Overlaid elemental maps from energy dispersive X-ray spectroscopic measurements of the same section in (d) 47

Figure 3.5. Scanning electron micrographs of cross sections of Ge films prepared by ec-LPE with the same conditions as in Figure 3.4a except formal concentrations of dissolved GeO_2 of 50, 100, and 225 mM in (a), (b), and (c), respectively. (d) Measured film thicknesses of Ge films prepared by ec-LPE as a function of the formal concentration of dissolved GeO_2. (e) Measured charge-time profiles for the ec-LPE depositions of the Ge films in (a)–(c). 49

Figure 3.6. Top-down view scanning electron micrographs of initial Ge deposits in ec-LPE depositions performed with the same conditions as in Figure 3.24a with (a) n^+-Si(100) and (b) n^+-Si(111) seed substrates. (c) Grazing angle X-ray diffractograms of Ge films prepared by ec-LPE with n^+-Si(100) and n^+-Si(111) seed substrates. (d) A representative X-ray rocking curve of a Ge film prepared by ec-LPE on a n^+-Si(100) e) Color-coded electron back scatter diffraction (EBSD) map (top-down view) of a Ge film prepared by ec-LPE on n^+-Si(100). (f) Contour pole figures from the EBSD mapping shown along the 110 and 111 poles. Each pole figure is made from 5438 independently solved EBSD patterns taken from a mapped area of ~1.5 mm^2. 50

Figure 3.7. (a) Bright field transmission electron micrograph viewed along the ⟨211⟩ zone axis of a cross section of an epitaxial Ge film prepared by ec-LPE on n^+-Si(111) with the same conditions as in Figure 3.4a. Electron diffraction patterns for the Ge film and the Ge/Si interface are shown in (b) and (c), respectively. (d) Low magnification annular dark-field scanning transmission electron micrograph of a cross section of an epitaxial Ge film prepared by ec-LPE on a n^+-Si(111) with the same conditions as in Figure 3.4a. (e) Representative high resolution annular dark-field scanning transmission electron micrograph of the interface between the Ge film and Si substrate shown in (d). 53

Figure 3.8. (a) Measured electron channeling pattern (ECP) collected at low-magnification (47×) from a Ge film prepared by ec-LPE on a n^+-Si(100) substrate overlaid on top of a simulated Ge ECP. (b) Electron channeling contrast image displaying a population of surface-penetrating threading dislocations (seen as bright/dark point features). Magnification: 25 000×, g = [220] diffraction condition..........................54

Figure 3.9. Syringe barrel used to apply a slight positive pressure to the liquid metal film. (a) Schematic shown with out ec-LPE cell and (b) schematic of the syringe barrel. A pressure transducer inserted between the bolt and syrringe plunger (a) was used to keep consistency between trials..........................58

Figure 3.10. Optical photographs of frozen liquid metal films after control experiments were performed in the ec-LPE cell both without (b) and with (c) a positive pressure applied. 59

Figure 4.1. Pseudo-binary phase diagram of mixtures of Ge and e-BiIn at standard pressure. The relative fractions of Bi and In are constant as the amount of Ge is varied. 65

Figure 4.2. Schematic of the two methods used to produce e-BiIn droplets by (a) sequential evaporation of Bi and In and (b) spreading of the liquid eutectic. a) Arrays of nanowells were

photolithographically patterned on a Si substrate followed by sequential evaporation of first Bi then In. Subsequently, the bilayers were annealed at T = 120 °C to form droplets of e-BiIn. b) Liquid e-BiIn was applied and spread over a substrate with microwells patterned in photoresist prepared by photolithography. Excess liquid metal was removed, leaving arrays of microwells filled with e-BiIn. 67

Figure 4.3. Schematic for producing e-BiIn nanodroplets in hole arrays patterned into SiO_2. Steps are same as in Figure 4.2a except an 700 nm SiO_2 is first deposited on the substrate using plasma enhanced chemical vapor deposition (PECVD) and the lithographic pattern is transferred to the SiO_2 layer using reactive ion etching (RIE). 68

Figure 4.4. A cross sectional scanning electron micrograph (a) of a e-BiIn droplet formed by sequential evaporation followed by annealing at T = 120 °C. Corresponding EDS elemental maps of In (b) and Bi (c). Scale bar: 5 µm. 70

Figure 4.5. Voltammetric responses for a e-BiIn film electrode immersed in 0.01 M $Na_2B_4O_7$(*aq*) without and with 0.05 M dissolved GeO_2 at T = 50 °C. Scan rate= 0.05 V s^{-1} 72

Figure 4.6. a) Cross sectional scanning electron micrograph of E-BiIn droplets on a Si(100) substrate after applying a bias of E_{appl}= -1.2V for 1 hr at T=50 ºC. b) Chronoamperometry response for Ge ec-LLS experiments on e-BiIn microdroplets in electrolyte containing 50 mM GeO_2 and 10 mM $Na_2B_4O_7$ at T=95ºC and E_{appl}=-1.6V. c) Tilted SEM image of Ge microwires obtained under the conditions from b). Scale bar: a) 2.5 µm inset 500nm, c) 10 µm. 74

Figure 4.7. Scanning electron micrograph (left) of the precipitate that forms during ec-LLS experiments at E = -1.6 V. EDS spectrum (right) from a selected region on the precipitate (shown in red on micrograph). Scale bar is 2.5 µm. 75

Figure 4.8. Atom probe tomography and cluster analysis of Ge wires grown from e-BiIn electrodes. (a) 3D elemental map, (b) Cluster counts as a function of d_{max} between solute atoms for the randomized and experimental data. (c) Cluster counts as a function of the number of atoms in a cluster for the randomized and experimental data for a d_{max} of 0.265 nm order. From the 3D elemental map a domain without clustering (d) and with clustering (e) were reconstructed. 76

Figure 4.9. (a) Scanning electron micrograph of the APT sample taken from a segment of a Ge microwire mounted on a Si micro-post and shaped to a fine point for APT analysis. b) Map of the Ge APT sample from a) where the greyscale intensity corresponds to occlusions of solvent atoms identified from cluster analysis. c) Histogram (bin size 5 atoms) showing the size distribution (number of clusters vs size of cluster) for a majority of the identified occlusions. The full range of the cluster sizes was not shown for clarity. d) average composition of the occlusions as a function of cluster size. Atomic fractions were obtained by averaging the composition of clusters contained within a set size range (i.e. bin size 10 atoms). e) the bulk elemental concentrations of Ge, Bi and In as a function of depth into the interior of the Ge microwire. The point 0 on the *x-axis* corresponds to the tip of the APT sample as well as the surface of the Ge microwire and a distance > 0 corresponds to the radial position inward. 78

Figure 4.10. a) Chronoamperometric response of Ge ec-LLS performed in electrolyte containing 50 mM of GeO_2 50mM and 10 mM $Na_2B_4O_7$ at E = -1.2V V and T = 95 °C with e-BiIn nanodroplets on a n^+-Si(100) substrate. b) Scanning electron micrographs of Ge nanowires prepared by ec-LLS as in (a) at b) low and c) higher magnification cross-sectional view of a Ge nanowire film. d) High magnification of individual Ge nanowire highlighting a coiled section. Scale bars: b) 1 μm, c) 1 μm, and d) 250 nm respectively.. 80

Figure 4.11. (a) Tilted scanning electron micrograph of Ge nanowires prepared by ec-LLS at E = -1.2 V and T = 90 °C following a pre-electrolysis step. (b) Cross-sectional scanning electron micrograph of nanowires in (a) indicate the propensity of the nanowires to follow the [111] growth direction of the underlying Si (111) substrate. Scale bar is (a) 2 μm (b) 1 μm. 81

Figure 4.12. a) Transition electron micrograph of a straight section of a Ge nanowire prepared by ec-LLS with e-$BiIn_3$ at E = -1.6 V and T = 95 °C. Scale bar: 50 nm b) High resolution transition electron micrograph of the lower box in (a) highlighting the crystallinity of the nanowire section. Scale bar: 5 nm Inset: selected area electron diffraction image. c) High resolution transmission electron micrograph of the upper box in (a) that contained the interface between E-BiIn and Ge. The dashed line highlights the edge of the crystalline Ge. Scale bar: 5 nm. 82

Figure 4.13. a) Bright-field transmission electron micrograph of a coiled Ge nanowire section aligned along the <220> zone axis. b) Corresponding dark-field transmission electron micrograph of the same coiled Ge nanowire section. Scale bars: 50 nm 84

Figure 4.14. a) Current-potential responses for three separate Ge nanowire measured by two contacts. Inset: Scanning electron micrograph of Ge nanowire resistivity measurement. Scale bar: 2.5 μm b) Measured resistance vs electrode spacing for the data in (a). 85

Figure 5.1. Schematic depiction of GaSb ec-LLS. (*1*) The dissolved Sb_2O_3(aq) precursor is electroreduced to Sb^0. (*2*) Dissolution of Sb^0 into the pool of Ga and subsequent metallurgical alloying reaction with the liquid metal. (*3*) Supersaturation within the liquid metal phase leads to the formation of GaSb nuclei. (*4*) GaSb crystals grow and emerge from the liquid Ga pool........94

Figure 5.2. a) Voltammetric responses for a Ga(l) working electrode in an aqueous electrolyte containing 0.6 M NaOH with and without dissolved Sb_2O_3(aq) at various formal concentrations up to the solubility limit at 25 ºC with a scan rate of 10 mV/s. b,c) Optical photograph of a clean Ga(*l*) pool working electrode with a geometric surface area of 0.615 cm^2 housed in a glass bowl (V = 350 cm^3) before (b) and after (c) applying E = -1.47 V vs Ag/AgCl for 1 hour while submerged in an aqueous electrolyte containing 0.1 mM Sb_2O_3 and 0.6 M NaOH. Electrical contact was made through a top Pt wire insulated from the electrolyte by polytetrafluoroethylene. 96

Figure 5.3. Normalized Raman spectra for films deposited on Ga(l) after being immersed in aqueous 0.6 M NaOH with Sb_2O_3 dissolved at a formal concentration of 0.1 mM while being held at a constant applied potential for 60 min at T = 90 ºC. Spectra are offset vertically for clarity...98

Figure 5.4. Raman spectra of films deposited on the Ga(l) electrode submerged in an aqueous electrolyte of 0.6 M NaOH with several different concentrations of the Sb_2O_3 precursor and held at E = -1.47 V for 60 min at T= 90 ºC. Spectra are offset vertically for clarity. 99

Figure 5.5. (a) Raman spectra of GaSb films deposited on a Ga(l) pool electrode with each trace corresponding to a different temperature used in the deposition. The Ga(l) was held at a constant potential of -1.47 V in 0.6M NaOH with dissolved Sb_2O_3 at a formal concentration of 0.1 mM for 60 min. Spectra are offset vertically for clarity. (b) The observed Raman shift of the TO phonon mode of bulk crystalline GaSb (ν) vs the growth temperature of each deposition. Error bars represent the standard deviation for N = 3. 102

Figure 5.6. (a) Time-dependent Raman spectra of films deposited at a Ga(l) electrode at E = -1.47 V in aqueous 0.6M NaOH with dissolved Sb_2O_3 at a formal concentration of 0.1 mM at T= 90 ºC for the indicated deposition time. The intensity of the traces corresponding to the 0 and 0.5 min depositions have been multiplied by a factor of 5 and all of the spectra are offset for clarity. (b)Raman shift of the TO phonon mode of c-GaSb versus the deposition time. 103

Figure 5.7. Scanning electron micrographs of films deposited on a Ga(l) pool electrode submerged in an aqueous 0.6 M NaOH with Sb_2O_3 dissolved at a formal concentration of 0.1 mM and held at E = -1.47 V for 1 hr. (a-c) Shows cross sectional images of the visible portions of undisturbed films approximately 1 μm above the liquid metal surface. (d) An individual GaSb grain after removal from the liquid metal electrode. 105

Figure 5.8. Representative Powder X-ray diffractogram collected from a film deposited on a Ga(l) pool electrode after being submerged in an electrolyte containing 0.1 mM Sb_2O_3 and 0.6 M NaOH at 90°C while held at a constant potential of -1.47 V for 60 min. The 2θ values for the expected crystallographic planes of zinc blende GaSb are denoted at the top. 106

Figure 5.9. (a-d) Transmission electron micrographs and selected area diffraction patterns of GaSb crystallites prepared under conditions as described in Figure 8. The (a) experimental and (b) modeled electron diffraction patterns observed along the [111] zone axis of a GaSb crystallite. (c) A dark field transmission electron micrograph formed by selecting for the 2-20 diffracted beam. (d) The complementary two-beam bright field comprised of the 000 and 2-20 beams. Scale bars = (a)0.4 $Å^{-1}$, (c and d) 40nm...108

Figure 5.10. Schematic depiction of the first step and second steps in the proposed scheme for ec-LLS as influenced by conditions that favor high densities and low densities of electrodeposited Sb^0 nuclei. 110

Figure 6.1. (a) Cyclic voltammogram at a Ga film electrode for 0.2M TBAC in PC (red) and after the addition of 500mM $SiCl_4$ (blue). (b) Chronoamperometric response of Ga film electrode with an applied bias of -2.5V vs Ag/AgCl in an electrolyte of 0.2M TBAC and 500mM $SiCl_4$ dissolved in PC. 119

Figure 6.2. Scanning electron micrographs of Si film(left) and islands (right) deposited on a Si(100) substrate at E_{appl} = -2.3 V. 120

Figure 6.3. Height contrast image (a) collected using a laser confocal microscope of Si film. AFM image (b) and corresponding height profile (c). 121

Figure 6.4. Scanning electron micrograph of film grown on an Si (111) substrate (a); inset shows EBSDP. Pole figures (b) plotted from the film in (a) and the expected location of the corresponding crystal planes for a 2D projection down the [111] zone axis (c). 123

Figure 6.5. Photographs of test tube containing 0.7 mM Sb_2O_3 + 600 mM NaOH (pH ~ 13.5) (a) and 100 mM $Sb(tar)_2$ + 10 mM $Na_2B_4O_7$ (pH ~8.0) (b). Cyclic voltammogram at a Ga electrode of the blank (200 mM L-tartaric acid + 10 mM $Na_2B_4O_7$) and experimental (100 mM $Sb(tar)_2$ + 10 mM $Na_2B_4O_7$) electrolyte. 125

Figure 6.6. Scanning electron micrographs of GaSb ec-LPE with a E-GaIn electrode at $Sb(tar)_2$ concentrations of 1, 0.4 and 0.1 mM (a). Top panel shows SEM islands that formed on underlying substrate and bottom panel shows SEM of liq metal surface after deposition. EDS (b) and Raman spectra (c) of the islands that formed on the substrate where the EDS was taken from the location shown in (a) by the red box....................127

Figure 6.7. Moles of Sb^{3+} reduced as a function of time (a) for chronoamperometric depositions with 0.4 and 0.1 mM $Sb(tar)_2$. The point at which the electrolyte becomes depleted of $Sb(tar)_2$ is indicated for each concentration. Scanning electron micrographs of underlying substrate after ec-LPE deposition for 3 hrs in 0.1 mM $Sb(tar)_2$ (b). Under identical conditions the entire volume of the electrolyte was replaced (c) to replenish the $Sb(tar)_2$ concentration....................128

Figure 6.8. Thin film flow cell used for deposition of GaSb. (a) Schematic, (b) and (c) optical photographs of actual setup during a deposition....................130

Figure 6.9. Scanning electron micrograph (a) and Raman spectra (b) of films obtained from the deposition in the thin film flow cell....................131

Figure 6.10. Scanning electron micrographs of the GaSb films covered in liquid Ga after the deposition in the thin film flow cell....................132

LIST OF TABLES

Table 5.1. Raman spectra features at various concentrations of Sb_2O_3 101

Table 6.1. Methods attempted to selectively remove excess Ga(l) 133

ABSTRACT

This thesis describes two major advancements in electrodeposition by ec-LLS. The first is a new low temperature (< 90 °C) epitaxial growth technique, termed electrochemical liquid phase epitaxy (ec-LPE), for group IV covalent semiconductors. The ec-LPE technique is based on an electrodeposition strategy, electrochemical liquid liquid solid (ec-LLS) growth, to produce crystalline group IV and III-V materials from liquid metal electrodes, which is also discussed. The quintessential aspect that defines ec-LLS is the liquid metal electrode. The liquid metal acts as an electrode for reducing the ionic precursor, a solvent medium to promote crystal growth, and (in the case of binary semiconductors) a reactant. The second is the ec-LLS electrodeposition of Ge nanowires using a eutectic BiIn (e-BiIn) alloy as an electrode / solvent. This work represents the first case of ec-LLS with a liquid metal alloy that does not contain Ga or Hg.

This thesis describes both fundamental and practical aspects of ec-LLS. Critical parameters (e.g. growth rate and supersaturation) influencing the Ge crystal growth in ec-LLS were studied in relation to temperature, applied potential and the mode of nucleation. The competition between heterogeneous and homogeneous nucleation was analyzed and the conclusions are used to develop ec-LPE. This thesis then details the first demonstration of ec-LPE. Large area epitaxial films of Ge were grown at T = 90 °C out on the benchtop. This thesis also describes the ec-LLS growth of Ge nanowires using a eutectic BiIn alloy. These Ge nanowires displayed a unique coiled morphology that had not been observed by ec-LLS previously. A final achievement on the concept of growing group III-V semiconductors by ec-LLS is also discussed. Crystalline GaSb was grown by electrodepositing Sb^0 at Ga(l) electrodes, followed by a spontaneous reaction between Ga^0 and Sb^0 to form GaSb. The cumulative work is then contextualized, with further directions highlighted.

CHAPTER 1

Introduction

A. Background

Since the invention of the integrated circuit (IC) in 1958[1] society has become increasingly dependent on semiconductor devices. The need to improve modern semiconductor devices has driven research and development in microprocessors, memory devices, renewable energy, display and sensing applications; creating a global market that yielded $338.9 billion[2] in sales in 2016 alone.

Traditionally, semiconductor devices are fabricated monolithically from single crystalline wafers of covalent semiconductor material (group IV or III-V) through a series of subtractive processing steps (top-down method). However, as device architectures become more complex and more difficult to shrink, the traditional top-down approach is becoming less tenable.

In contrast to top-down methods, complex architectures can also be fabricated through bottom-up methods where the active semiconductor material in the device is formed additively, such as in the growth of nanostructured materials.[3] By growing the active semiconductor materials, additional control is afforded over physical, electrical and geometric properties. Additionally, bottom-up methods can significantly reduce the number of required processing steps to fabricate a given device architecture, increasing yield and lowering cost.

Bottom-up methods facilitate device miniaturization. Nanowire group IV and III-V semiconductor materials are attractive for scaling down complementary metal oxide semiconductor (CMOS) technology to the nanometer range while achieving highly reproducible critical device dimensions.[4]

Bottom-up methods also facilitate epitaxial films of group IV and III-V semiconductors. The pristine interface between epitaxial layers promotes facile charge transfer across the

film/substrate interface by reducing the number of trap states or recombination centers. In addition, epitaxial films allow for physical properties that differ from the substrate (i.e. dopant densities / types, composition and bandgap) to be utilized in a device. These two characteristics make epitaxial films critical in optoelectronic applications, for example in high efficiency multi-junction solar cells.[5,6] Epitaxial films are also beneficial for high performance IC's due to the lack C and O impurities which can reduce carrier lifetimes.[7]

B. Crystal Growth Methods for Covalent Semiconductors

There are two strategies that enable the growth of crystalline covalent semiconductors. The first strategy (Figure 1.1a), is to employ high temperatures during the crystal growth, affording adsorbed species (adspecies) a fast surface mobility.[8] Surface diffusion can promote facile rearrangement of the adspecies to adopt the correct position (i.e. a kink site) in the developing crystal lattice. This concept is the basis of vapor phase epitaxy (VPE) techniques which includes metal organic chemical vapor deposition (MOCVD)[9,10] and molecular beam epitaxy (MBE).[11-13]

The second strategy (Figure 1.1b) is to conduct the growth in a fluid medium that is capable of solvating the component atoms of the solid in order to develop a reversible pathway between the solid and fluid phase.[8] The reversible pathway allows for the atoms to continually deposit (or adsorb) and dissolve providing a route to correct for defectivity and form an ordered structure. Covalent semiconductors are insoluble in aqueous and organic solvents[14] and therefore these solvents are not suitable for growing covalent semiconductor crystals. However, this strategy has been employed by solid liquid solid growth (SLS)[8,15], liquid phase epitaxy (LPE)[16] and vapor liquid solid growth (VLS)[17-20] by exploiting the solvating power of liquid metals towards covalent semiconductors.

Currently the state of the art methods for growing epitaxial films of covalent semiconductors (MBE and MOCVD) suffer from three main drawbacks. First, the high temperatures employed limits the scope of compatible materials and pre-existing device architectures that can be used as substrates in the deposition. Second, these techniques use highly-processed and expensive gaseous precursors that are often extremely toxic, corrosive and/or pyrophoric. These precursors merit both safety and environmental concerns and add significant cost (e.g. disposal and engineering controls) when conducting VPE on large scales. Third, since moisture and O_2(g) contamination are detrimental to the film growth, VPE techniques are

a)

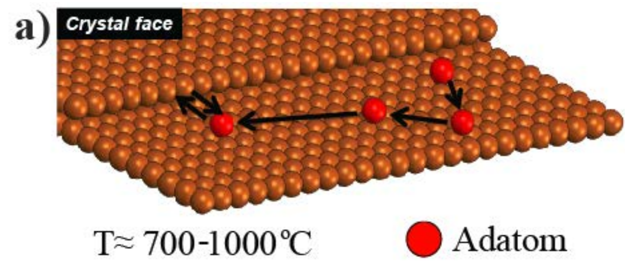

b)

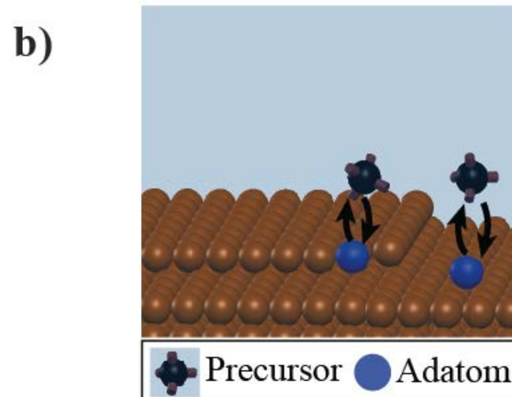

Figure 1.1. Schematics depict strategies for growing covalent semiconductor crystals. a) Growth occurs at high temperature to promote fast surface mobilities and b) Growth occurs in a fluid phase where a reversible pathway between solid and solution phase is developed.

conducted in strictly controlled atmospheres (ultra-high vacuum and inert gas environments). As a result, these VPE techniques require complex and expensive instrumentation. Due to a combination of these factors epitaxial growth is generally the most expensive processing step in the semiconductor industry costing ~50-100 $/wafer, whereas most other processing steps are closer to 1 $/wafer.[7] By identifying a low-cost alternative to grow epitaxial films of covalent semiconductors these complex devices (e.g. multi-junction solar cells) can become more viable for commercial applications.[21]

C. Aqueous Electrodeposition of Covalent Semiconductors

Electrodeposition is frequently used throughout industry to deposit metal plugs, films and coatings. For example, electrodeposition is used to deposit Cu interconnects for IC's as part of the Damascene process[22,23] and to deposit corrosion resistant metal coatings in the automotive industry.[24]

The appeal of conventional aqueous electrodeposition is based on the low-cost, scalability and simplicity of the technique. First, this technique is traditionally an aqueous process conducted in atmospheric ambients. Second, electrodeposition can be accomplished using benign precursors formed from non-energy intensive processes. Third, the instrumentation for electrodeposition is comparatively simple. In electrodeposition, the application of an external DC bias provides the energy necessary to reduce/oxidize ionic precursors. This aspect is in sharp contrast to the previously mentioned growth techniques for covalent semiconductors which use thermal energy to decompose precursors into the reaction product. The use of electrical energy to promote the precursor reactions allows electrodeposition to be performed at low temperatures.

Crystalline ionic II-VI semiconductor materials (i.e. (CdTe, CdSe) can be plated through aqueous electrodeposition.[25,26] A popular method of electrodepositing II-VI materials is through electrochemical atomic layer epitaxy (ECALE)[27] where monolayers of alternating group II and group VI materials are deposited using underpotential deposition. However, ECALE of crystalline group III-V semiconductors is extremely challenging and have not been successfully reported for Ga based III-V or group IV materials.[28,29]

Despite the widespread use of aqueous electrodeposition in depositing metal coatings this technique is not frequently employed for plating covalent semiconductors. This is because the

resultant deposits are amorphous and contain a significant level of impurities from the supporting electrolyte and solvent. There has been significant effort to deposit covalent semiconductors (Ge[30-32], GaAs[33,34] and GaSb[35,36]) through aqueous electrodeposition (including ECALE[29]), however, only amorphous deposits have been observed without a subsequent high temperature annealing step post-deposition. Since conventional aqueous electrodeposition results in amorphous deposits it is not considered a viable low temperature route.

D. ec-LLS Growth of Covalent Semiconductors

As shown by SLS[37], VLS[19] and LPE,[16] several liquid metals (e.g. Ga, In, Au, Ag and Bi) support growth of high quality covalent semiconductor crystals at temperatures > 500 ºC. Previously, our group has developed the notion of electroplating crystalline covalent semiconductors at or near room temperatures using liquid metal electrodes through a process termed electrochemical liquid-liquid solid growth (ec-LLS) (Figure 1.2). The quintessential aspect that defines ec-LLS is the liquid metal electrode. The liquid metal acts as an electrode for reducing the ionic precursor, a solvent medium to promote crystal growth, and (in the case of binary semiconductors) a reactant. We propose that the liquid metal enables a reversible pathway between the solid crystalline and liquid phase enabling the low temperature growth of crystalline covalent semiconductors. By combining the beneficial solvation properties that liquid metals display for covalent semiconductors with conventional electroplating we have demonstrated the low temperature (25ºC< T < 90ºC) growth of crystalline Ge,[38,39] Si,[40] GaAs[41] and GaSb[42] semiconductors.

The elementary steps in ec-LLS are as follows. First, an applied potential (E_{appl}) reduces an ionic precursor to form a zero-valent species that adsorbs onto the surface of the liquid metal. Then due to a finite solubility, the species dissolves into the liquid metal. Continued accumulation eventually results in a supersaturation which provides the driving force for homogeneous crystal nucleation and growth. ec-LLS can proceed through a homogeneous (within bulk of liquid metal pool) or heterogeneous (at the interface with a substrate) route.[43-45]

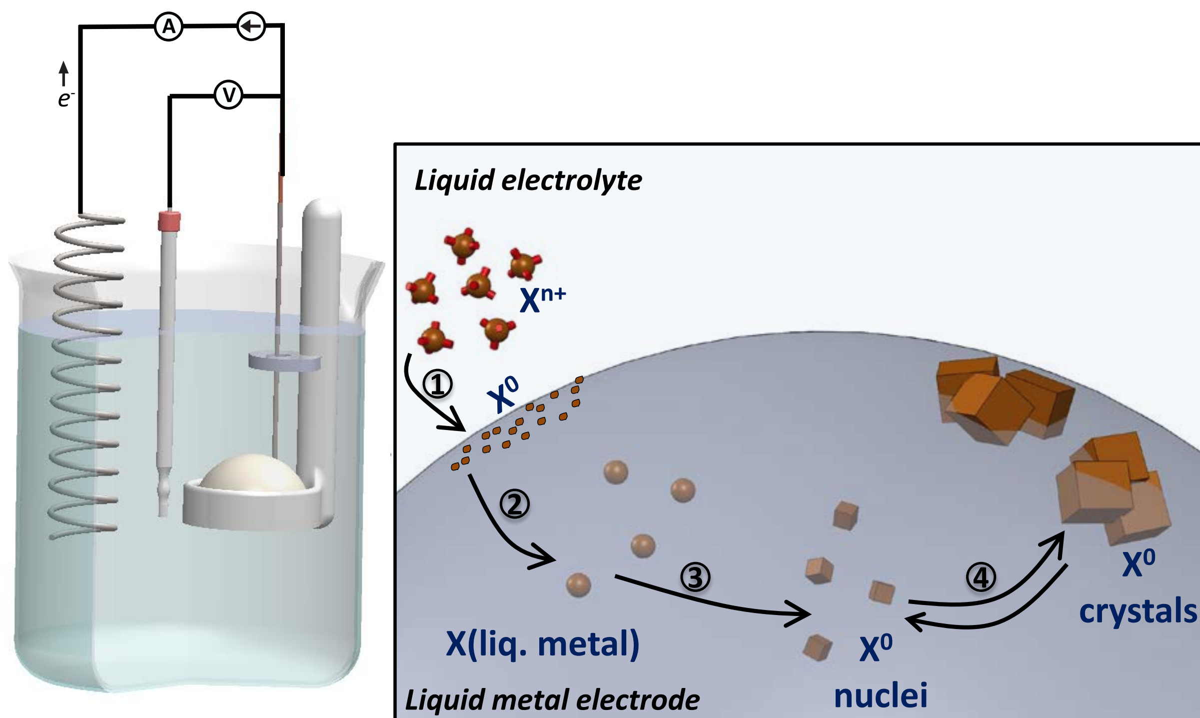

Figure 1.2. Schematic of electrochemical liquid-liquid solid (ec-LLS) growth. 1) electrochemical reduction of ionic precursor, 2) dissolution of zero valent species, 3) homogeneous nucleation and 4) growth of covalent semiconductor.

E. Thesis Objectives and Content Description

The work in this thesis can be split into two separate objectives. First, to better understand ec-LLS on a fundamental level, the individual steps of ec-LLS (Figure 1.2) are examined. Specifically, the crystal growth in ec-LLS from liquid metals solvents is analyzed by measuring growth rates and developing a kinetic model to describe ec-LLS. Critical crystal growth parameters such as the driving force for nucleation, solubility and concentration gradients are determined. The second objective of this thesis is to develop a new epitaxial film growth method based on ec-LLS, electrochemical liquid phase epitaxy (ec-LPE). In this thesis, the ec-LPE technique is demonstrated for Ge and Si.

Chapter 2 explores three main hypotheses of Ge ec-LLS. First, the thickness of a liquid metal film dictates where and how (homogeneous vs heterogeneous) a crystal nucleates and ultimately grows. This hypothesis was tested by setting up a matrix of experiments in which both the diffusional distance through the liquid metal and the growth temperature were varied. SEM and EDS mapping was then used to check for the presence homogenous growth where the Ge crystals would appear floating on the surface of the liquid metal. This was instrumental in determining the critical thickness of liquid metal needed to achieve exclusive heterogeneous growth which was used in developing ec-LPE in chapter 3. Second, crystal growth rates and levels of supersaturation needed to initiate crystal growth can be determined through time dependent measurements. Using time dependent powder X-ray diffraction (PXRD) and cross-sectional SEM the growth rate of the Ge crystal was measured. From the growth rate, the induction time for Ge nucleation could be extrapolated. Using the current attributed to $HGeO_3^-$(aq) reduction, the flux of Ge^0 into the liquid metal was determined and used in calculating the concentration profile within the liquid metal as a function of time. From the concentration gradient at the point of nucleation the supersaturation and driving force for heterogeneous nucleation could be determined and was found to be on the order of 100 times the equilibrium concentration of Ge in e-GaIn. Third, the different driving forces needed to initiate crystal growth at the liquid metal electrolyte interface (homogeneous) versus the liquid metal substrate interface (heterogeneous) can be determined. The observations made on homogenous nucleation were used to identify the conditions (diffusional distance, temperature and precursor influx) for which homogeneous nucleation first occurs. Under these conditions, the concentration gradient was calculated to find the supersaturation / driving

force for homogeneous nucleation. By comparing the driving force for heterogeneous and homogeneous nucleation a consistent difference in energy was observed.

Chapter 3 details a new method for depositing epitaxial films of covalent semiconductors, electrochemical liquid phase epitaxy (ec-LPE). Specifically, large area Ge epitaxial films were grown on Si substrates using a custom electrochemical cell. The cell allows for thin e-GaIn and Ga films to function as electrodes making the diffusional distance to the substrate small over macroscopic areas. The epitaxial character of the Ge film is demonstrated by X-ray diffraction and electron backscatter diffraction which showed single crystalline grains of over 3 mm^2. The density of threading dislocation defects was analyzed by electron channeling contrast imaging and found to be $1.7 \pm 0.2 \times 10^9$ cm^{-2} which is consistent with Ge heteroepitaxy on Si substrates. This work identifies a new method for growing large area epitaxial films of covalent semiconductors at low temperature out on the benchtop through the electrochemical reduction of a naturally occurring and benign precursor (GeO_2).

Chapter 4 demonstrates the ec-LLS growth of Ge nanowires (NW's) at 90 ^oC using a eutectic BiIn (e-BiIn) liquid metal. e-BiIn nanodroplets were fabricated on Si substrates by sequential metal evaporation into a SiO_2 template. Following the application of a potential, Ge NW's were electrodeposited and displayed a high aspect ratio. Furthermore, the wires showed a unique coiled morphology which has not been observed in ec-LLS previously. Atom probe tomography showed both In and Bi impurities formed clustered aggregates within the Ge crystal matrix rather than being homogeneously distributed. The cumulative results implied that the physical properties of the alloy, as a whole, can influence the tendency for an individual metal impurity atom to incorporate and should be considered when screening a new liquid metal alloy as a solvent for ec-LLS.

Chapter 5 explores the idea of forming III-V semiconductors by ec-LLS. Specifically, GaSb crystals were grown by electrodepositing Sb^0 at liquid metal electrodes, followed by a spontaneous reaction. The deposits were shown to be crystalline GaSb by powder X-ray diffraction (PXRD), Raman spectroscopy and electron diffraction. In addition, the influence that the temperature, applied potential, precursor concentration and deposition time had on the growth of GaSb was analyzed by Raman spectroscopy. The ec-LLS growth of GaSb and GaAs were compared to highlight similarities and differences and to identify critical physical properties that

influenced the growth and crystalline quality of the deposits. Several observations were noted. First, the concentration of the dissolved precursor strongly determined whether the electrodeposited film was composed of the target III–V compound or mainly the pure group V element. Second, the crystalline quality of the electrodeposited film was more sensitive to changes in the temperature than to changes in the applied potential. Increasing the overpotential used for ec-LLS did not affect a discernible change in the observable crystallite size. Third, a temperature threshold was apparent, below which only disordered binary semiconductors were observed. These cumulative observations support the general premise that ec-LLS for GaSb and GaAs operate by similar mechanisms. However, there were still significant differences between the ec-LLS of GaAs and GaSb that was attributed to the marked difference in solubility, where Sb is 10^5 times more soluble than As in Ga.

Chapter 6 summarizes additional efforts that remain ongoing. The ec-LPE thin film growth technique has been extended to include Si and GaSb. The progress and prospects of these efforts are discussed.

F. References

(1) Kilby, J. S. *IEEE Trans. Electron Devices* **1976**, *23*.
(2) Rosso, D.; Semiconductor Industry Association: 2017.
(3) Yang, P.; Yan, R.; Fardy, M. *Nano Lett.* **2010**, *10*, 1529.
(4) Lu, W.; Lieber, C. M. *Nat Mater* **2007**, *6*, 841.
(5) Grassman, T.; Chmielewski, D.; Carnevale, S.; Carlin, J.; A. Ringel, S. *IEEE J. Photovolt.* **2015**, *6*, 326.
(6) Yoshikawa, K.; Kawasaki, H.; Yoshida, W.; Irie, T.; Konishi, K.; Nakano, K.; Uto, T.; Adachi, D.; Kanematsu, M.; Uzu, H.; Yamamoto, K. *Nature Energy* **2017**, *2*, 17032.
(7) Xiao, H.; Society of Photo-optical Instrumentation, E. *Introduction to semiconductor manufacturing technology*; SPIE: Bellingham, Wash. (1000 20th St. Bellingham WA 98225-6705 USA), 2012.
(8) Trentler, T. J.; Hickman, K. M.; Goel, S. C.; Viano, A. M.; Gibbons, P. C.; Buhro, W. E. *Science* **1995**, *270*, 1791.
(9) Jing, Y.; Bao, X.; Wei, W.; Li, C.; Sun, K.; Aplin, D. P. R.; Ding, Y.; Wang, Z.-L.; Bando, Y.; Wang, D. *J. Phys. Chem. C* **2014**, *118*, 1696.
(10) Barrett, C. S. C.; Martin, T. P.; Bao, X. Y.; Kennon, E. L.; Gutierrez, L.; Martin, P.; Sanchez, E.; Jones, K. S. *J. Cryst. Growth* **2016**, *450*, 39.
(11) Manfra, M. J. *Annu. Rev. of Condens. Matter Phys.* **2014**, *5*, 347.
(12) Madiomanana, K.; Bahri, M.; Rodriguez, J. B.; Largeau, L.; Cerutti, L.; Mauguin, O.; Castellano, A.; Patriarche, G.; Tournié, E. *J. Cryst. Growth* **2015**, *413*, 17.
(13) Atkinson, P.; Eddrief, M.; Etgens, V. H.; Khemliche, H.; Debiossac, M.; Momeni, A.; Mulier, M.; Lalmi, B.; Roncin, P. *Appl. Phys. Lett.* **2014**, *105*, 021602.
(14) Buhro, W. E.; Hickman, K. M.; Trentler, T. J. *Adv. Mater.* **1996**, *8*, 685.

(15) Wang, F.; Dong, A.; Buhro, W. E. *Chem. Rev.* **2016**, *116*, 10888.
(16) Capper, P.; Mauk, M.; Wiley Online, L. *Liquid phase epitaxy of electronic, optical, and optoelectronic materials*; Wiley: Chichester, England ; Hoboken, NJ, 2007.
(17) Wagner, R. S.; Ellis, W. C. *Appl. Phys. Lett.* **1964**, *4*, 89.
(18) Sunkara, M. K.; Sharma, S.; Miranda, R.; Lian, G.; Dickey, E. C. *Appl. Phys. Lett.* **2001**, *79*, 1546.
(19) Schmidt, V.; Wittemann, J. V.; Gösele, U. *Chem. Rev.* **2010**, *110*, 361.
(20) Gutsche, C.; Lysov, A.; Regolin, I.; Blekker, K.; Prost, W.; Tegude, F.-J. *Nanoscale Res. Lett.* **2011**, *6*, 65.
(21) Essig, S.; Allebé, C.; Remo, T.; Geisz, J. F.; Steiner, M. A.; Horowitz, K.; Barraud, L.; Ward, J. S.; Schnabel, M.; Descoeudres, A.; Young, David L.; Woodhouse, M.; Despeisse, M.; Ballif, C.; Tamboli, A. **2017**, *2*, 17144.
(22) Andricacos, P. C. *Interface* **1999**, *8*, 32.
(23) Nguyen, N. T.; Boellaard, E.; Pham, N. P.; Kutchoukov, V. G.; Craciun, G.; Sarro, P. M. *J. Micromech. Microeng.* **2002**, *12*, 395.
(24) Song, G.-L. *Prog. Org. Coat.* **2011**, *70*, 252.
(25) Klein, J. D.; Herrick, R. D.; Palmer, D.; Sailor, M. J.; Brumlik, C. J.; Martin, C. R. *Chem. Mater.* **1993**, *5*, 902.
(26) Rajeshwar, K. *Adv. Mater.* **1992**, *4*, 23.
(27) Gregory, B. W.; Stickney, J. L. *J. Electroanal. Chem. Interfacial Electrochem.* **1991**, *300*, 543.
(28) Wade, T. L.; Vaidyanathan, R.; Happek, U.; Stickney, J. L. *J. Electroanal. Chem.* **2001**, *500*, 322.
(29) Villegas, I.; Stickney, J. L. *J. Electrochem. Soc.* **1992**, *139*, 686.
(30) Liang, X.; Zhang, Q.; Lay, M. D.; Stickney, J. L. *J. Am. Chem. Soc.* **2011**, *133*, 8199.
(31) Hall, J. I.; Koenig, A. E. *J. Electrochem. Soc.* **1934**, *65*, 215.
(32) Fink, C. G.; Dokras, V. M. *J. Electrochem. Soc.* **1949**, *95*, 80.
(33) Chandra, S.; Khare, N. *Semicond. Sci. Technol.* **1987**, *2*, 214.
(34) Yang, M. C.; Landau, U.; Angus, J. C. *J. Electrochem. Soc.* **1992**, *139*, 3480.
(35) Paolucci, F.; Mengoli, G.; Musiani, M. M. *J. Appl. Electrochem.* **1990**, *20*, 868.
(36) McChesney, J. J.; Haigh, J.; Dharmadasa, I. M.; Mowthorpe, D. J. *Opt. Mater.* **1996**, *6*, 63.
(37) Wang, F.; Dong, A.; Buhro, W. E. *Chem. Rev.* **2016**, *116*, 10888
(38) Carim, A. I.; Collins, S. M.; Foley, J. M.; Maldonado, S. *J. Am. Chem. Soc.* **2011**, *133*, 13292.
(39) Fahrenkrug, E.; Maldonado, S. *Acc. Chem. Res.* **2015**, *48*, 1881.
(40) Gu, J.; Fahrenkrug, E.; Maldonado, S. *J. Am. Chem. Soc.* **2013**, *135*, 1684.
(41) Fahrenkrug, E.; Gu, J.; Maldonado, S. *J. Am. Chem. Soc.* **2013**, *135*, 330.
(42) DeMuth, J.; Ma, L.; Fahrenkrug, E.; Maldonado, S. *Electrochim. Acta* **2016**, *197*, 353.
(43) Ma, L.; Lee, S.; DeMuth, J.; Maldonado, S. *RSC Adv.* **2016**, *6*, 78818.
(44) Fahrenkrug, E.; Biehl, J.; Maldonado, S. *Chem. Mater.* **2015**, *27*, 3389.
(45) Fahrenkrug, E.; Gu, J.; Jeon, S.; Veneman, P. A.; Goldman, R. S.; Maldonado, S. *Nano Lett.* **2014**, *14*, 847.

CHAPTER 2

Controlling Nucleation and Crystal Growth of Ge in a Liquid Metal Solvent

A. Introduction

Crystal growth in a saturated solution is a fundamental process in chemistry. As crystalline boules pulled from melts are the feedstock for semiconductor wafers, crystal growth is arguably also the bedrock of modern electronics.[1] A promising strategy to lower the energy cost involved in the preparation of crystalline semiconductors is the use of molten metals.[2-6] Liquid metals have long been identified as solvents for covalent Group IV semiconductors such as Ge and Si[7] and as physical catalysts for the conversion of amorphous semiconductors into crystalline materials.[8] Liquid metals have also been extensively utilized for the synthesis of Group IV micro-/nanowires through vapor–liquid–solid (VLS)[9,10] and solution–liquid–solid (SLS) methods.[11-13] Despite the importance, a detailed understanding is presently lacking regarding what properties in a liquid metal are most useful in the formation of a high quality semiconductor crystal.

The study of liquid metals as solvents is greatly facilitated by approaches where the crystal growth can be controlled easily and with precision. The electrochemical liquid–liquid solid (ec-LLS) process is a new liquid metal based growth method that is particularly suitable for this type of study. An applied electrochemical current/potential can define the flux of species into liquid metals in ec-LLS (Figure 2.1).[3,14-22] Since heterogeneous electrochemical reactions at an electrode surface are controlled precisely using simple electronics[23] rather than heat or pressure, ec-LLS offers a high degree of control that is atypical of most melt crystal growths. If properly exploited, ec-LLS offers a means to study crystal growth in liquid metals quantitatively.

We focus here on the ec-LLS process for crystalline Ge, a practically relevant covalent semiconductor used in multijunction photovoltaics,[24] infrared detection,[25] light emitting diodes,[26] and high-speed integrated circuits.[27] Ge ec-LLS by electroreduction of GeO2 dissolved in aqueous electrolyte (eq 1) at a liquid metal electrode was previously demonstrated.[15-17,19] In this work, we

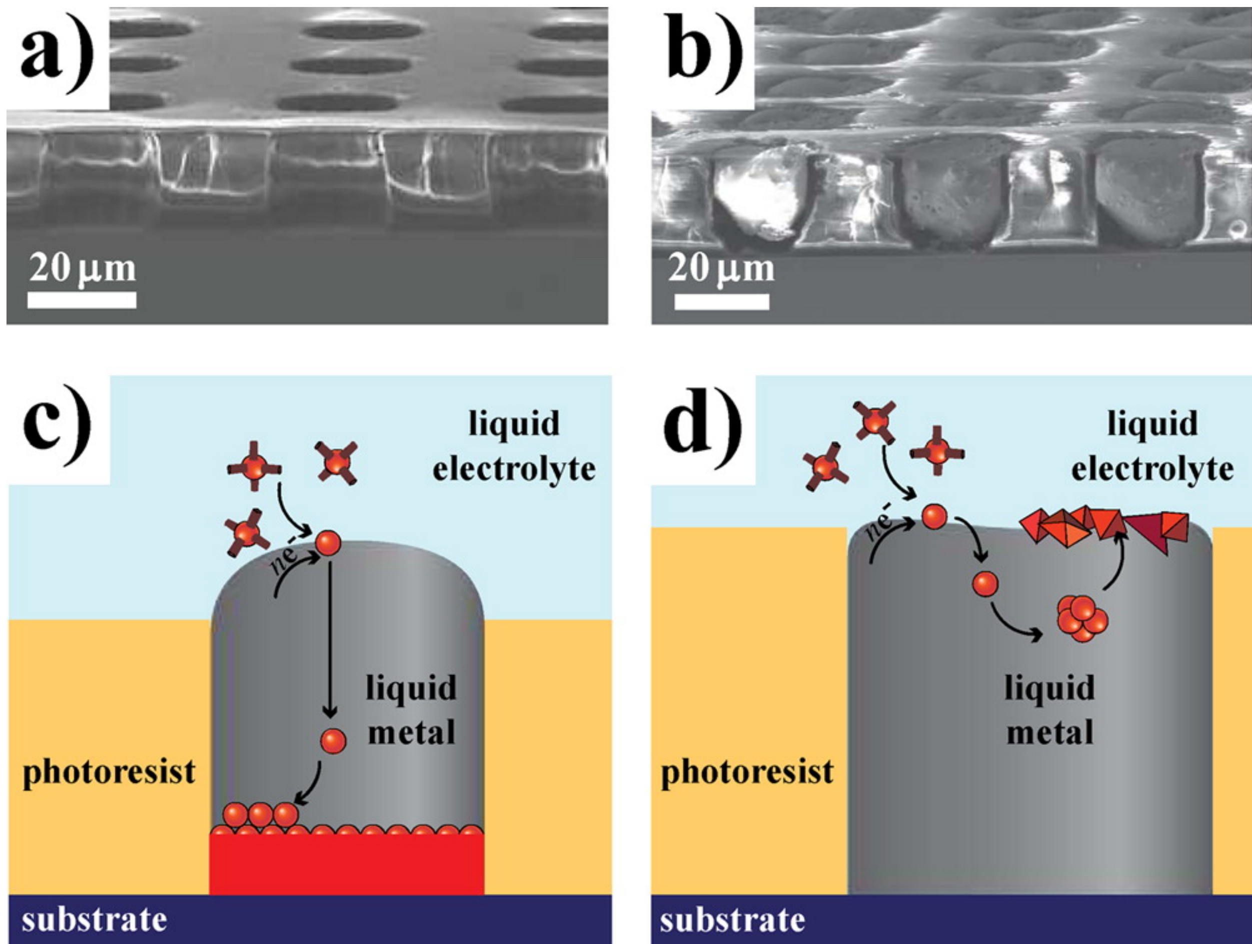

Figure 2.1. Microwells patterned in photoresist on n^+-Si(100) (a) before and (b) after filling the with e-GaIn. (c) Schematic depiction of ec-LLS inside a shallow microwell filled with liquid metal. Solute can reach the bottom interface and preferentially nucleate and grow a crystal heterogeneously. (d) Same as in (c) except the microwell is sufficiently deep enough that no solute reaches the bottom interface and instead preferentially nucleates and grows crystals homogeneously within the liquid metal.

choose an indium–gallium eutectic (e-GaIn, $Ga_{0.833}In_{0.167}$) as a representative liquid metal of interest. e-GaIn has many uses as a low melting point (melting point = 15.7 °C)[28] conductive fluid[29] and has recently been shown as a potential solvent for the growth of Group IV semiconductors.[16]

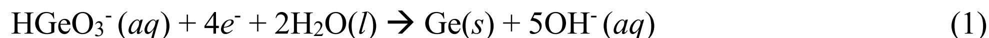

$$HGeO_3^-(aq) + 4e^- + 2H_2O(l) \rightarrow Ge(s) + 5OH^-(aq) \quad (1)$$

This paper identifies three fundamental aspects of the Ge ec-LLS process specifically and metal-based semiconductor crystal growth generally. The first hypothesis explored is that the thickness of a liquid metal film dictates where and how crystals nucleate and ultimately grow (Figure 2.1). The basic premise is that if the e-GaIn/Si interface is positioned far enough away from where the solute enters the liquid metal, nucleation of Ge at the e-GaIn/Si interface will not occur exclusively. We demonstrate the utility of photolithographically patterned microwell platforms that can be easily filled with liquid metal (Figure 2.1).[16] The geometry of the microwell ensures that all solutes enter the liquid metal only at the top plane and travel the same distance in order to reach the bottom interface. The microwell platform also avoids complications from electrocapillarity[29,30] or coalescence of unconfined liquid metal droplets. In addition, the thickness of the liquid metal can be varied easily by changing the photoresist thickness.

The second hypothesis explored herein is that the Ge crystal growth rates and the level of supersaturation needed to initiate crystal formation in ec-LLS can be determined through time-dependent measurements. Through chronoamperometry, X-ray diffraction, and electron microscopic analyses, data are presented that highlight production of crystalline Ge as a function of time and the delay time needed to induce crystalline Ge formation in ec-LLS as a function of temperature and applied potential.

The final point explored here is that, unlike other liquid metal based crystal growths, the driving force needed to start crystal nucleation at the interface between e-GaIn and Si(100) in ec-LLS can be estimated. The relevance of these points on advancing specifically new, low-temperature methodologies for crystalline semiconductor films and on understanding semiconductor crystal growth generally are discussed.

This chapter has previously been published in *Crystal Growth and Design*.[31] The text and figures have been reprinted in this thesis chapter with permission from the American Chemical Society (ACS).

B. Methods

Materials

Acetone (ACS grade, BDH), indium (99.99% Gallium Source), germanium dioxide (99.998% Sigma-Aldrich), sodium borate (>99.5% Sigma and Alderich), SU-8-2007 (MicroChem Corp.), SU-8-2025 (MicroChem Corp.), SU-8 developer (MicroChem Corp.) gallium (99.999%, Alfa Aesar), hydrofluoric acid (49%, Transene Inc.), methanol (ACS grade, BDH), 2-propanol (ACS grade, BDH), ethylene glycol (>99%, Sigma-Aldrich), hexamethyldisilazane (HMDS, Fischer Scientific), oxygen gas (Metro Welding, Detroit, MI). Si substrates for microfabrication and electrodeposition consisted of As-doped n-+Si(100) (Crysteco, < 0.007 Ω·cm, 0.625 ± 0.020 mm thick). Water with a resistivity >18.2 MΩ·cm (Nanopure Barnstead Water Purification) was used throughout.

Microfabrication and Preparation of Microwells Filled with e-GaIn

Photoresist films patterned with arrays of microwells with various depths were prepared on Si substrates following photolithography. The n^+-Si(100) wafers were diced into 1 in^2 squares and then degreased through sonication sequentially in hexanes, acetone, methanol, and water then drying with N_2(g). The substrates were then etched in 5% hydrofluoric acid for 1 min, rinsed with water and dried under an N_2(g) stream. Hexamethyldisilazane (HMDS) was spin-coated to act as a photoresist adhesion promoter. SU-8 2007 (for 8 µm thick films) or SU-8 2025 (for >10 µm thick films) was then spin-coated onto each substrate. The substrate was then heated for 3 min at T = 95 °C (for 10 µm thick films) or 2 min at T = 65 °C followed by 5–6 min at T = 95 °C (for >10 µm thick films). Following, the substrates were exposed (OAI model 30 lamp: 220–450 nm) at 26–30 W cm^{-2} through a custom contact photomask (Fineline Imaging, Colorado Springs, Co). The substrates were then heated on a hot plate for 5 min at T = 95 °C (for 10 µm thick films) and 1 min at T = 65 °C followed by 5–6 min at T = 95 °C (for >10 µm thick films) and allowed to sit at room temperature for 2 min prior to development. The substrates were then developed with agitation using developer (MicroChem) to remove the unexposed SU-8 for 5 min and then thoroughly rinsed with 2-propanol and dried under N_2(g) stream. To ensure the bottom of each microwell was free from any residual photoresist, each of the patterned substrates were subjected to an intensive O_2

plasma cleaning for 1.5 min (model PE-50, Plasma Etch Inc.) The substrates were then annealed in air at $T = 125$ °C for 25 min to fully cross-link the exposed photoresist.

The patterned substrates were mounted on a vacuum chuck, while a small droplet of e-GaIn was dispensed on the pattern substrate to fill the microwell array with liquid e-GaIn. The e-GaIn droplet was repeatedly spread and mechanically tapped into the wells for ~4 min. Excess e-GaIn was removed by wiping with a methanol soaked lint-free towel (Kimtech W4, Fisher).

Electrochemical Methods

Autolab (Metrohm), CHI420A, and CHI760C (CH Instruments) workstations and a Solartron 1286 (Ametek) potentiostat were used to apply a bias and measure current/charge. All measurements were performed in a three-electrode Teflon cell under ambient pressure that was immersed in a propylene glycol/water bath for temperature control. A Viton O-ring sealed the Teflon cell to the substrate. A platinum mesh counter electrode was used. A silver wire coated with silver chloride immersed in a 4 M KCl reference electrode was used for all experiments and all potentials are referenced to E(Ag/AgCl). No temperature correction was applied to the potential values since potential shift in E^0 induced by the change in temperature ($\frac{\Delta S^{\circ}}{nF}$; where ΔS° is the entropy involved in the $4e^-$ reduction of dissolved GeO_2 in water) was ~2.3×10^{-4} V per degree K.[32] This shift amounted to a difference of 9 mV in E^0 between $T = 40$ °C and $T = 80$ °C.

Materials Characterization

Scanning electron micrographs were obtained with either a FEI Nova Nanolab Dualbeam Focused Ion Beam Workstation or a JEOL-7800FLV equipped with a Schottky field emitter filament using an Everhart-Thornly Detector (ETD) or a through–the-lens detector (TLD). Energy dispersive spectroscopy (EDS) spectra and maps were collected using an Oxford X-MaxN silicon drift detector (Oxford Instruments). Powder X-ray diffractograms were obtained with a Bruker D8 Advance X-ray diffractometer with a Cu Kα X-ray source ($\lambda = 1.5406$ Å). The source slit was 2 mm, and the data were sampled at 0.040 deg/s at each interval; at $2\theta = 27.2°$ (~Ge(111) reflection) the beam was measured to be 5.6×23.8 mm by exposing an X-ray sensitive film which ensured the entire electrodeposition area 2.7 mm in diameter was exposed to the X-ray beam. The integrated XRD intensities of the Ge(111) reflection were converted to moles of Ge using a

calibration curve created from samples with known mass using a microbalance. Diffraction peak areas were determined through fitting with a pseudo-Voigt function in JADE.

Modeling

A one-dimensional, finite-difference model was developed to determine the concentration gradient of Ge in e-GaIn and to predict the local concentration at the induction time necessary to initiate crystal growth during ec-LLS. The implicit Crank-Nicholson method [33] with a time step of 0.001 s and a grid spacing of 0.2 μm in a code written in Python was used to model the diffusional transport of a solute (Ge) within a thin liquid metal according to Ficks' second law of diffusion (eq 2) with Dirichlet and Neumann boundary conditions.

$$\frac{dC}{dt} = D\frac{d^2C}{d^2z} \qquad 0 \leq z \leq L \tag{2}$$

$$C(z,0) = 0 \tag{3}$$

$$\left(\frac{dC}{dz}\right)_{z=L} = \frac{i}{DnFA} \tag{4}$$

$$\left(\frac{dC}{dz}\right)_{z=0} = 0 \quad for\ C(0,t) < C \tag{5}$$

The term C denotes the concentration of the solute (Ge) in the liquid metal (e-GaIn), C_{nuc} is the concentration at which nucleation occurs, z represents the vertical position along the liquid metal thickness, L is the vertical position at the liquid metal/liquid electrolyte interface, t is the time after the potential step in the ec-LLS experiment, i is the current for the reduction of $HGeO_3^-$ (*aq*) at the liquid electrolyte/liquid metal interface, n is the number of equivalents of e^- needed to produce one equivalent of Ge (i.e., 4), A is the area of the electrode that the current passes across (i.e., the geometric areas of the filled microwells), and F is Faraday's constant. The diffusion coefficient, D, for Ge in pure liquid Ga was calculated as 1.33×10^{-5} cm^2 s^{-1} at $T = 25$ °C from the Sutherland–Einstein equation.[34,35] This value was used for the diffusivity of Ge in e-GaIn since

the viscosities of e-GaIn and Ga are similar (1.99×10^{-3} and 2.04×10^{-3} Pa s at $T = 25$ °C respectively).[36] The Stokes–Einstein relation was used to adjust the diffusion coefficient for changes in temperature.[37] The overall volume expansion in the liquid droplet due to the addition of Ge was neglected.

Equation 3 represents the initial conditions within the liquid metal prior to the potential step where there was no Ge in the liquid metal. The boundary condition at the liquid metal/liquid electrolyte interface ($z = L$, eq 4) was set so that the flux of Ge into the liquid metal is defined exactly by the current flux. That is, the model assumes that the current flux for the reduction of species at the liquid metal/electrolyte interface determined the feed rate of Ge into the liquid metal. The interface between the liquid metal and the underlying substrate (i.e., $z = 0$) acts as an impermeable boundary (eq 5) until the critical concentration is reached for crystal nucleation. In this way, the amount of Ge in e-GaIn increases everywhere within the liquid metal until crystal nucleation and growth occur. After that time point, a new boundary condition would be necessary to describe the interface to account for heterogeneous crystal nucleation and growth.

The value of the equilibrium solubility (mol L^{-1}), C_{eq}, of Ge dissolved in e-GaIn was calculated using the regular solution model,[7]

$$N_A k_B T \ ln\left(\frac{C_{eq}M}{\rho}\right) = -\Delta G_{Ge}^{FUS} + \alpha_{Ge-Ga}(1-r) + \alpha_{Ge-In}\left(1-\frac{1}{r}\right) - \alpha_{Ga-In} \quad (6)$$

$$C_{eq}(T) = \frac{\rho}{M}\exp\left[\frac{-\Delta G_{Ge}^{FUS} - \alpha_{Ge-Ga} \times r - \frac{\alpha_{Ge-In}}{r} + (\alpha_{Ge-Ga} + \alpha_{Ge-In} - \alpha_{Ga-In})}{N_A k_B T}\right] \quad (7)$$

where k_B is Boltzmann's constant, N_A is Avogadro's number, ρ is the density of e-GaIn, M is the formula mass of e-GaIn, ΔG_{Ge}^{FUS} is the latent heat released during Ge crystallization,[38,39] α_{Ge-Ga}, α_{Ge-In}, α_{Ga-In} are the interaction parameters between two components[7] using values of −879, 3450, and 9414 J mol^{-1},[40-43] respectively, and r is the molar ratio of Ga to In in the liquid metal. For perspective, the solubility of Ge in e-GaIn at room temperature is 5.11×10^{-6} atom % (4.13×10^{-4} mol L^{-1}) and the liquidus line for Ge in e-GaIn calculated using eq 7 is shown in Figure 2.2.

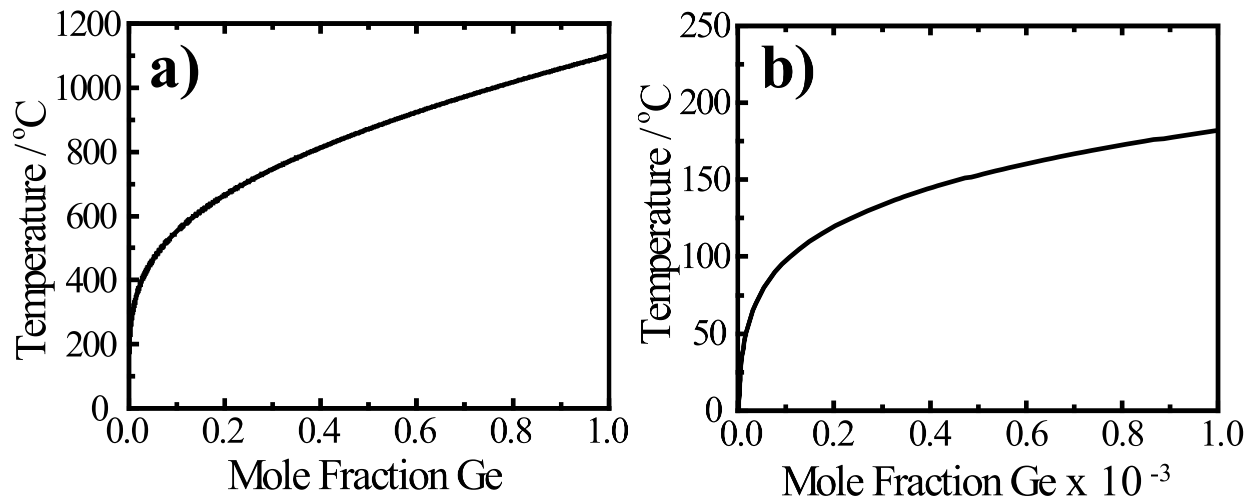

Figure 2.2. Calculated liquidus curve for Ge dissolved in e-GaIn using eq 7. Plots are shown on scale of Temperature vs Mole Fraction Ge (a) and Temperature vs Mole Fraction Ge x 10^{-3}.

Assumptions for Crystal Nucleation

The driving force, $\Delta\mu$, available for nucleation is defined by the level of supersaturation; i.e., the amount of solute that is dissolved is more than the thermodynamic solubility limit[44] and is given by eq. 8,

$$\Delta\mu = k_B T \ln\frac{a}{a_{eq}} = k_B T \ln\frac{\gamma C}{\gamma_{eq}\eta} \tag{8}$$

where a is the activity of the solute at nucleation, a_{eq} is the activity of the solute at the solubility limit, η is the mole fraction of the solute at the solubility limit, and γ and γ_{eq} are the activity coefficients at a given solute loading and the equilibrium solubility limit, respectively. If the absolute solute concentrations at nucleation and at the solubility limit are relatively small, then $\gamma \approx \gamma_{eq}$.[45,46] The activity coefficient of Ge in e-GaIn was calculated using eq 9 where the interaction parameters were approximated using the quasiregular solution models,[7]

$$RT ln(\gamma_i) = \sum_{\substack{j=1\\ i\neq j}}^{m} \alpha_{ij} X_j^2 + \sum_{\substack{k=1\\ k<j, j\neq 1}}^{m} \sum_{\substack{j=1\\ i\neq k}}^{m} (\alpha_{ij} + \alpha_{ik} - \alpha_{kj}) X_k X_j \tag{9}$$

where R is the ideal gas constant, T is the temperature in kelvin, α is the interaction parameter for a given component, γ_i is the activity coefficient and X is the mole fraction. The supersaturation range spans those expected in *ec-LLS* growth as determined from the main text. Since the amount of Ge in e-GaIn never exceeded a supersaturation of 250 in any trials, the approximation $\gamma \sim \gamma_{eq}$ is justified (Figure 2.3).

Accordingly, the driving force for nucleation can be approximated by just the solute concentration (relative to the solubility limit) directly.

$$\Delta\mu \approx k_B T \, ln\frac{C}{C_{eq}} \tag{10}$$

In the classical model of crystal nucleation,[1,44] the specific driving force, $\Delta\mu_{nuc}$, required for a stable nucleus is inversely related to the square root of the activation energy, ΔG_{nuc}, for nucleation.[1,47]

$$\Delta\mu_{nuc} = 4V\sqrt{\frac{\pi\alpha^3 f}{3\Delta G_{nuc}}} \approx k_B T \ln\frac{C_{nuc}}{C_{eq}} \tag{11}$$

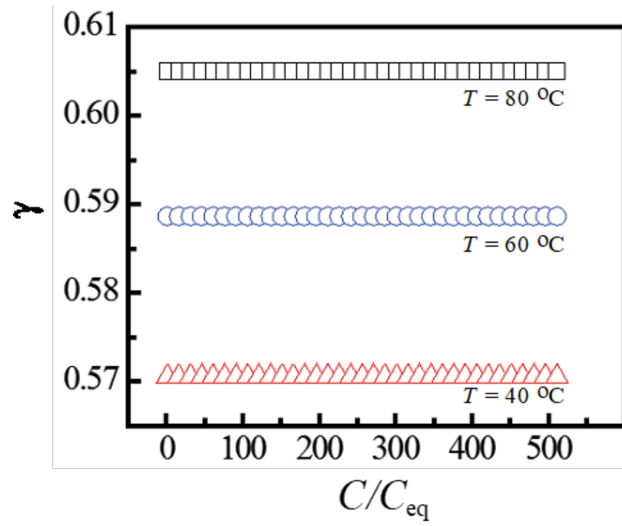

Figure 2.3 The activity coefficient as a function of the supersaturation of Ge on E-GaIn at T= 40 ºC, 60 ºC and 80 ºC

where α describes the surface free energy gained by forming of a new solid/liquid interface rather than being dissolved in the solvent, V is the solute molar volume, C_{nuc} is the solute concentration at the start of nucleation, and f is a wetting term describing the interaction of the solvent and solid precipitate.[47] For homogeneous nucleation, $f = 1$. For heterogeneous nucleation, $f < 1$.[47] Three key insights from eq 11 are pertinent to this work. First, stable nuclei will not form until a threshold supersaturation is reached. Second, different supersaturation values at the same temperature are required for different Ge nucleation pathways that have unequal activation barrier values. Third, nucleation at an interface could occur at lower driving forces than nucleation inside a solvent (i.e., homogeneous).

C. Results

Figure 2.4 presents the electrochemical data recorded for three different ec-LLS experiments performed with $E = -1.6$ V at $T = 40$, 60, and 80 °C using arrays of liquid e-GaIn microelectrodes with a nominal thickness of 8 μm. In general, each experiment in Figure 2.4 attained some nominal steady-state current. Upon integration, the corresponding charge-time plots for these data were linear with time. A series of samples were weighed after a known amount of charge was passed to determine the faradaic efficiency for Ge^0 production (Figure 2.4b). The charge-mass relation for each temperature was linear but the nonzero intercept implied a faradaic efficiency less than unity. The charge-mass values suggested a faradaic efficiency of ∼57%. Presumably, the primary competition for faradaic efficiency for the ec-LLS process was H^+ reduction at the liquid electrolyte/e-GaIn interface and at the liquid electrolyte/Ge^0interface. From these data, the corrected steady-state currents in Figure 2.4a corresponded to average fluxes of Ge to the liquid metal interface of each well giving 9.69×10^{-9}, 1.49×10^{-8}, and 1.82×10^{-8} mol s^{-1} cm^{-2} for $T = 40$, 60, and 80 °C, respectively.

Figure 2.5 summarizes observations from a series of Ge ec-LLS experiments under 12 different conditions. Each trial was performed for 30 min with $E = -1.6$ V and at either $T = 40$, 60, or 80 °C and with liquid metals possessing either 8, 16, 20, and 27 μm thickness. For a given set of liquid metal thickness and temperature, there are two representative scanning electron micrographs shown in a cross-sectional view at low and high magnification. These images are representative of what was observed across the entire array of microwells for each experiment.

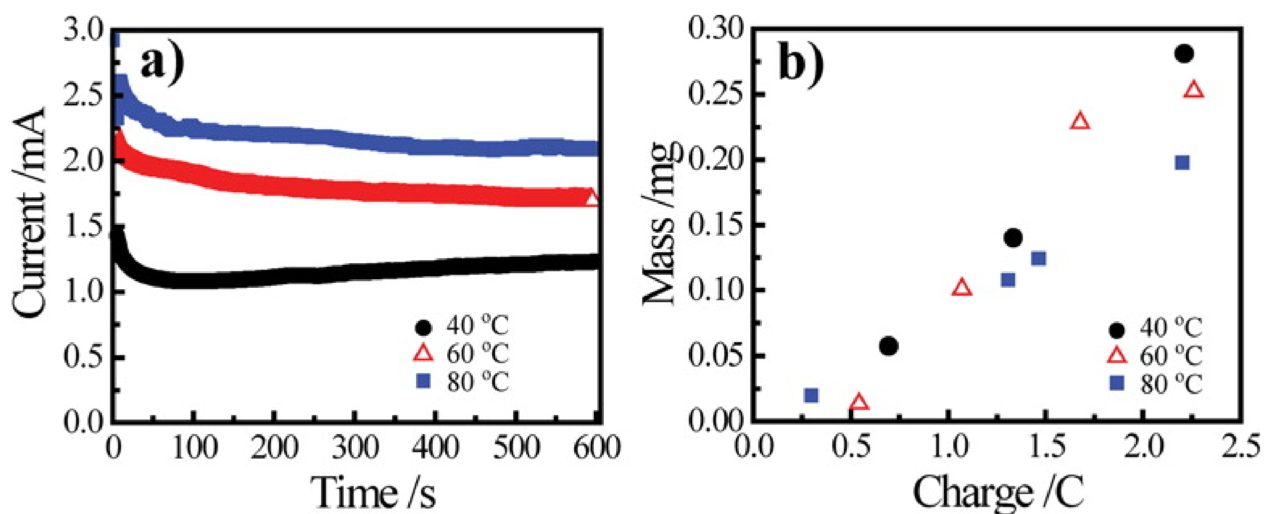

Figure 2.4. (a) Current–time data recorded for Ge ec-LLS experiments performed at $E = -1.6$ V and at $T = 40$, 60, and 80 °C in aqueous solution containing 50 mM GeO_2 and 10 mM $Na_2B_4O_7$. (b) Measured dependence of mass vs total charge passed at $E = -1.6$ V and at $T = 40$, 60, and 80 °C.

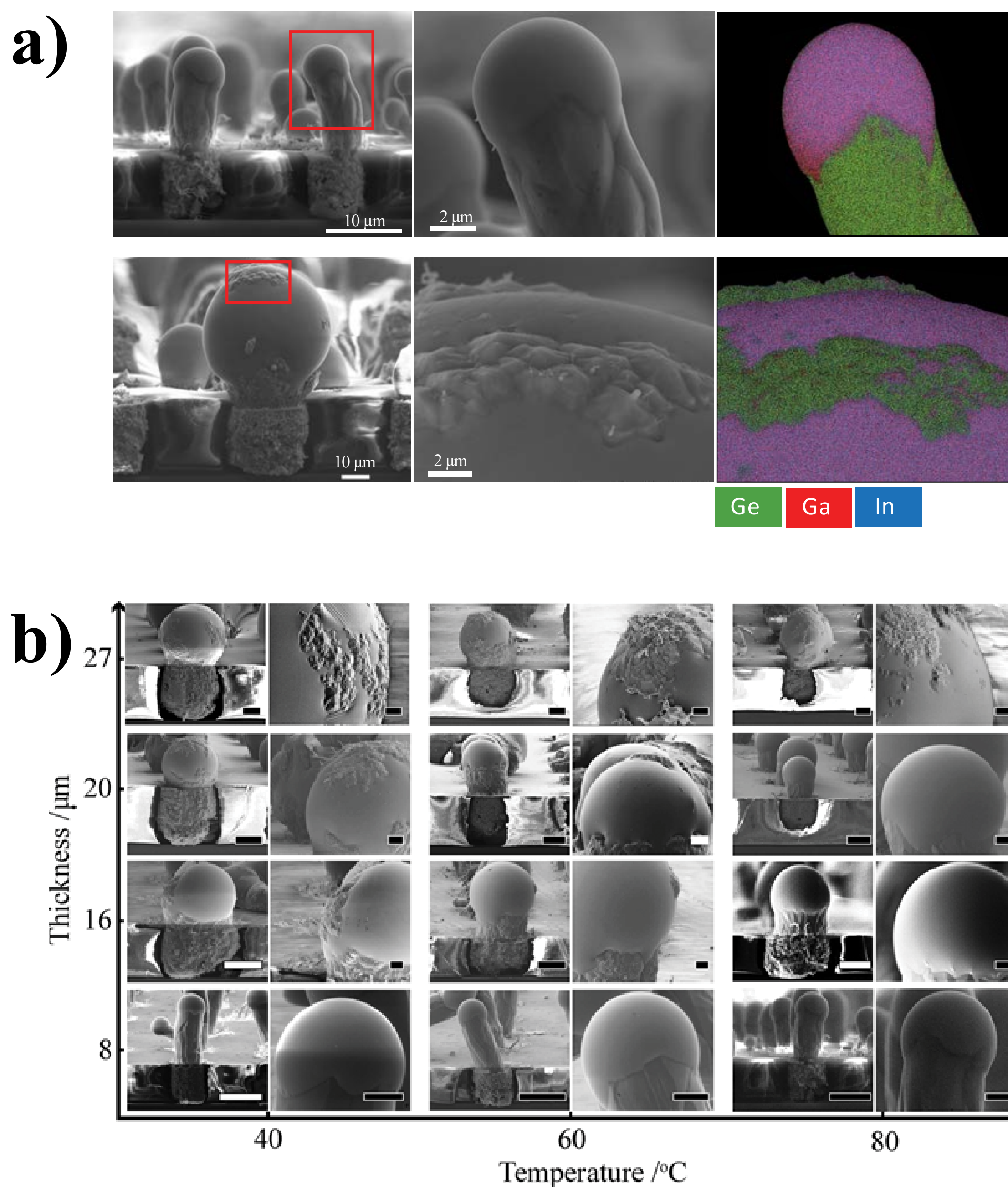

Figure 2.5. (a) Scanning electron micrograph and EDS elemental map of a 8 µm and 27 µm liquid metal thickness at T = 80 ºC. (b) Scanning electron micrographs and EDS map of Ge ec-LLS experiments Scanning electron micrographs of Ge ec-LLS experiments performed in the same electrolyte as in Figure 2.4 at E_{appl} = −1.6 V for 30 min at T = 40, 60, and 80 °C and with several e-GaIn thicknesses. In each pair, the scale bar for the left image is 10 µm and for the right image is 2 µm.

Two general observations are apparent in Figure 2.5. First, in all cases, the relative position of the liquid metal changed after ec-LLS. That is, a fraction or all of the liquid metal was displaced upward and out of the microwell. In every tested condition, the liquid e-GaIn then assumed a spherical (rounded) shape once outside of the microwell. Because of the different heights of the photoresist, the total displacement of liquid e-GaIn was not consistent in every tested condition set. At a thickness of 27 μm, the liquid metal rested just at the top of the microwell. In contrast, at a thickness of 8 μm, the liquid metal was displaced well outside of the photoresist by crystalline Ge that deposited underneath it. In this way, a Ge microwire formed that was capped by liquid e-GaIn.[19] Second, the surface of the liquid metal microdroplets did not look the same in all experiments. At a given temperature, ec-LLS experiments performed with the thickest liquid metals always yielded crystalline product on top. Specifically, aggregates of crystals and some nanowires covered some or most of the liquid metal surface. Energy dispersive X-ray elemental analysis showed that these materials were Ge (Figure 2.5a). In contrast, experiments performed with the thinnest liquid metals never yielded any observable crystal aggregates on top. The higher the temperature, the greater the thickness range for e-GaIn that exhibited a "pristine" interface.

The data in Figure 2.5 showed that ec-LLS proceeded exclusively through heterogeneous crystal nucleation and growth at a liquid metal thickness of 8 μm. Accordingly, microwell platforms with this characteristic thickness were studied in greater detail to elucidate information on the driving force for crystal nucleation and the rate-determining factors in ec-LLS. Figure 2.6a–d presents cross sectional scanning electron micrographs for four ec-LLS experiments conducted for different lengths of time. These ec-LLS experiments were performed at $E = -1.6$ V and $T = 80$ °C. The average heights of the Ge microwires appeared linearly related to the ec-LLS experiment time, with the lengths increasing at longer times. Although the Ge microwire height appeared uniform across the majority of the area of the microwell arrays, cross-sectioning samples was tedious and the various tilts of the microwires introduced uncertainty in measurement of height. As a result, a separate measure of the amount of crystalline Ge was pursued.

Although not typically used for quantitative detection, X-ray diffraction was employed here as an ensemble measurement of the amount of crystalline Ge produced by ec-LLS for four reasons: (1) unlike mass measurements, the intensity of any X-ray diffraction is proportional only to the total amount of *crystalline* material being probed;[48,49] (2) there are diagnostic diffraction

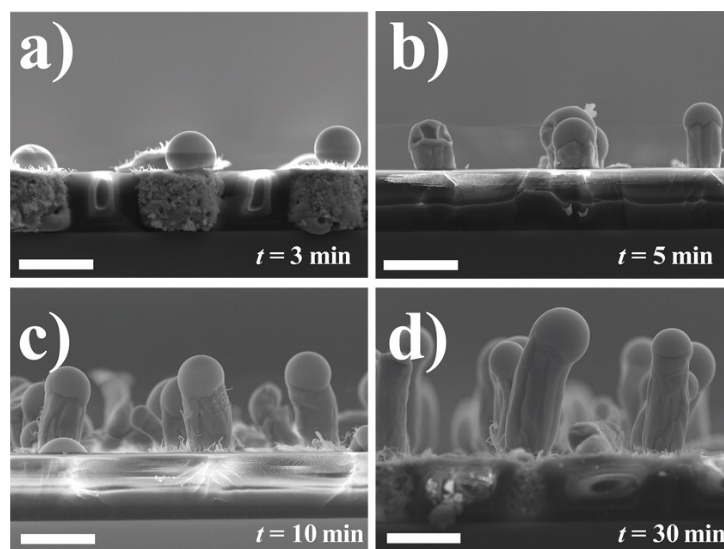

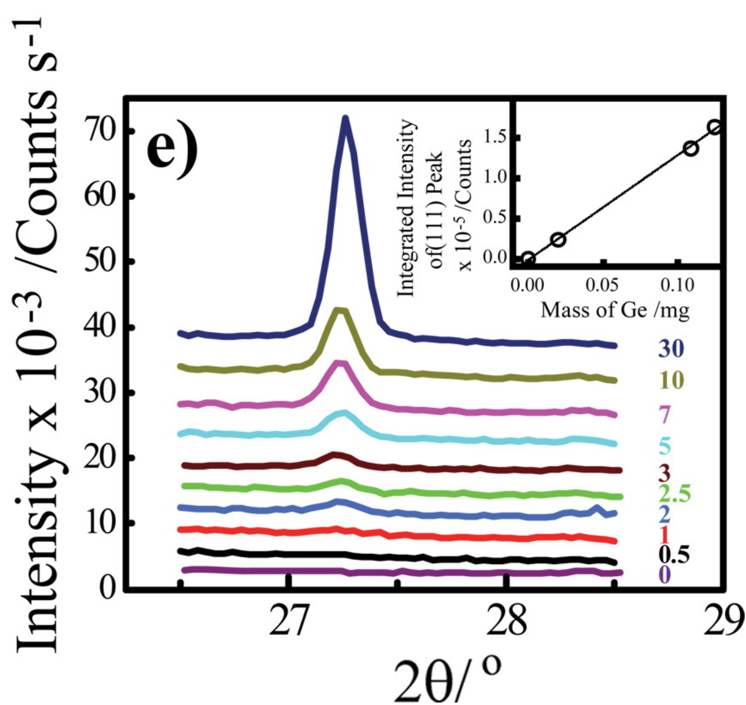

Figure 2.6. (a–d) Cross sectional scanning electron micrographs after Ge ec-LLS performed in the same electrolyte as in Figure 2.4 with a liquid metal thickness of 8 μm, $E = -1.6$ V, and for either (a) 3 min, (b) 5 min, (c) 10 min, and (d) 30 min. (e) Powder X-ray diffractograms of the Ge(111) signal measured for samples at various times (indicated to the right of the trace). (Inset) A calibration plot for the integrated intensity of the Ge(111) diffraction signal as a function of Ge mass.

peaks that identify crystalline Ge unambiguously;[15](3) X-ray diffraction measurements are high throughput and nondestructive, and (4) the liquid metal[36] and the photoresist layer[50] both have low X-ray mass absorption coefficients and therefore did not attenuate the Ge signal appreciably. Regarding attenuation, the intensity of the Si(400) reflection was compared to the same signal measured on a bare Si(100) substrate and therefore served as an internal standard. To assess whether the as-deposited crystalline Ge demonstrated a preferred orientation that could complicate X-ray diffraction intensity analysis, control experiments were performed in which the relative intensities of the Ge(111), Ge(220) and Ge(311) diffraction peaks were analyzed. A comparison was made between these data and diffraction data obtained for a polycrystalline Ge powder reference sample where the grains were randomly oriented. The data for the crystalline Ge materials prepared here by ec-LLS showed the same relative intensities as the reference sample at low and high temperatures, indicating the absence of any preferred orientation.

A set of diffractograms were first collected with different known amounts of Ge deposited in the wells to calibrate the X-ray diffraction peak intensity with mass of Ge (Figure 2.6e inset). The X-ray diffraction intensity was found to be linearly proportional with the amount of Ge. Figure 2.6e shows an overlay of several X-ray diffractograms obtained from the microwell array electrodes after ec-LLS experiments conducted for different lengths of time at $E = -1.6$ V and $T =$ 80 °C.

Figure 2.7 displays the moles calculated from the integrated intensity of the Ge(111) diffraction peak recorded as a function of time for four different sets of ec-LLS experiments conducted at different temperatures and either $E = -1.6$ V. The error on each data point in Figure 2.7 represents individual measurement error. Each data set showed the measured moles of crystalline Ge produced was directly proportional to experiment time, indicating that the growth rate was linear. Two additional aspects of the linear least-squares fitting of the data were noted. First, the slopes of each best fit line were different for the data sets compiled at $E = -1.6$ V, with the largest slope for the ec-LLS experiments at $T =$ 80 °C. These slopes are plotted in semilogarithmic form with respect to T^{-1} (Figure 2.7b). These data were also linear, i.e., the measured slopes showed an Arrhenius-type sensitivity toward temperature. Second, the best fit lines for all the data sets in Figure 2.7a did not have an intercept at $t = 0$. Instead, each data set had a unique, positive intercept on the time axis indicating that crystal growth did not initiate immediately at the start of any ec-LLS experiment. That is, every ec-LLS trial featured a delay time on the time scale of tens of seconds before nucleation of crystalline Ge occurred. During this

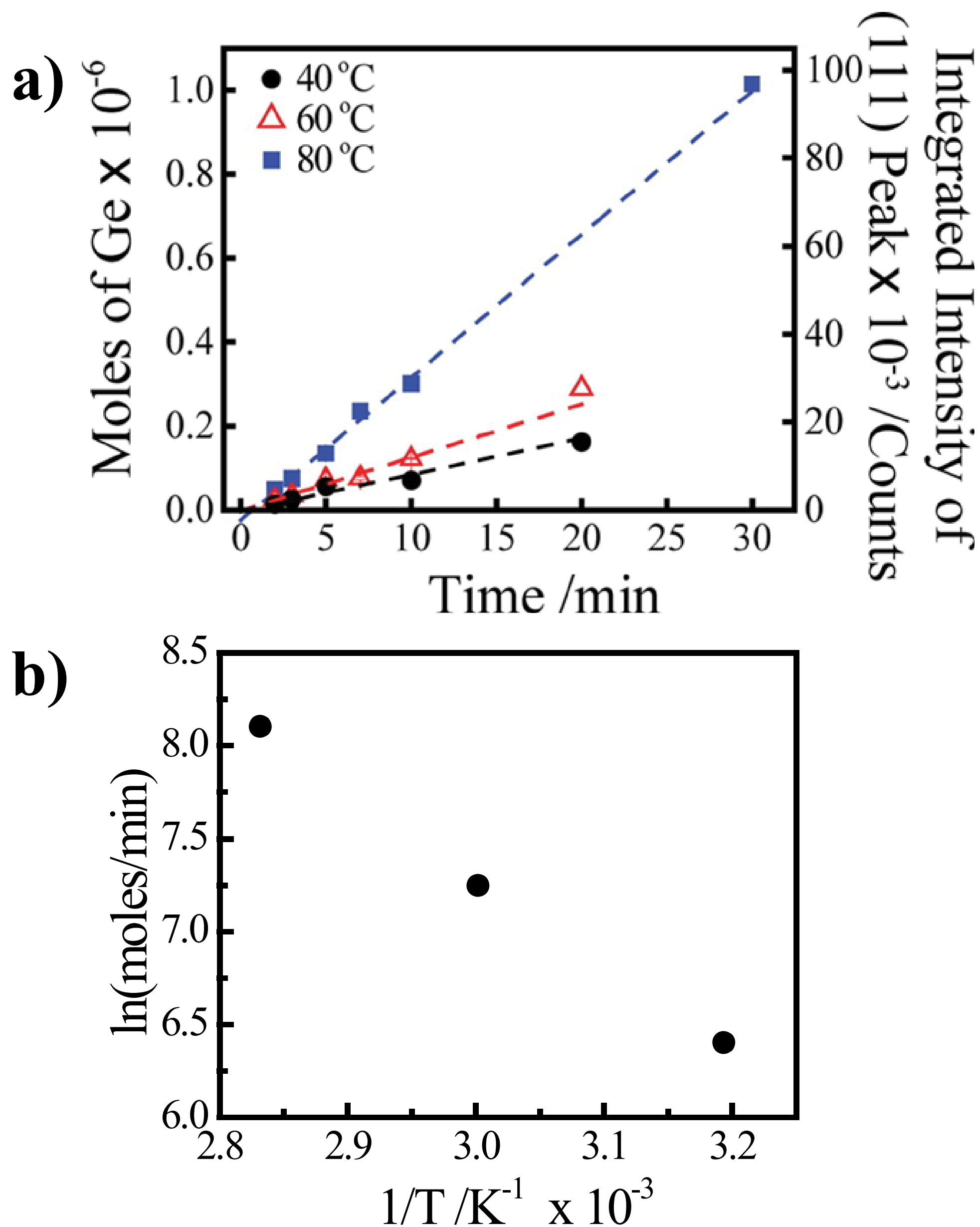

Figure 2.7. (a) Integrated intensity of the Ge(111) diffraction signal as a function of the duration of the ec-LLS experiment. The conditions for each ec-LLS experiment are the same as in Figure 2.4 Each dashed line represents the linear least-squares best fit. The slopes from (a) for data collected at E = -1.6 V are plotted as a function of reciprocal temperature (b).

time, the e-GaIn volumes accumulated Ge at a rate defined by the current flux for the electroreduction of dissolved GeO_2.

D. Discussion

The presented data, in conjunction with predictions from a one-dimensional (1D) model of transport in these liquid metal volumes, support three distinct points. First, nucleation at a specific interface can be favored exclusively in liquid metal films below a critical thickness. Second, the nucleation of Ge crystals in e-GaIn via ec-LLS must occur at large concentrations of Ge approximately 10^2 greater than the solubility limit. Third, the critical driving forces for Ge crystal nucleation are only slightly less at a Si surface than within e-GaIn. These points are described individually below.

Critical Liquid Metal Thickness

The microwell platform was effective in testing the competition between nucleation pathways at the bottom interface with the substrate and within the liquid metal electrode. The dimensions of these microwells were small relative to the diffusional transport and effected a transport time from the top to the bottom of less than 0.5×10^{-3} s in 8 μm droplets. Further, there were no signs of crystal growth/adhesion of Ge on the photoresist sidewalls. Accordingly, treating only the bottom interface as available for heterogeneous nucleation essentially rendered this a 1D system, greatly facilitating modeling and interpretation.

The critical thickness below which only heterogeneous nucleation occurred at the e-GaIn/Si(100) interface was strongly sensitive to temperature. Higher temperatures enabled thicker e-GaIn films to support Ge ec-LLS with only heterogeneous nucleation and crystal growth. That is, if a thicker e-GaIn liquid metal is used, higher temperatures are necessary to effect heterogeneous crystal deposition at the bottom interface *exclusively*. The data in Figure 2.5 are clear that only an e-GaIn thickness of 8 μm was sufficiently thin to promote heterogeneous nucleation exclusively throughout the entire temperature range.

Supersaturation at the Start of Ge Crystal Growth

The measured current (after correction for faradaic efficiency) in these deposition experiments was explicitly the electrochemical reaction rate for the formation of Ge^0. Since accumulation of amorphous Ge was not noticed here or in any previous Ge ec-LLS study,[3,15-17,19,22] the measured current necessarily also corresponded to the flux of Ge into the liquid e-GaIn solvent

in ec-LLS. A constant flux of Ge^0 into e-GaIn simplifies the expected concentration gradient throughout the liquid metal as a function of time. A 1D finite difference model was used to visualize this. Figure 2.8a–c shows the concentration of Ge in e-GaIn films as a function of position at several times prior to nucleation for a deposition run at $E = -1.6$ V and $T = 80$ °C. The gradient at all times is nonlinear and the concentration-position profile changes rapidly at early times. By 0.01 s, the concentration gradient reaches a characteristic shape that is maintained at longer times, as shown in Figure 2.8 b,c. That is, even though Ge concentration keeps increasing everywhere in the liquid metal, the difference between the concentrations at the top and bottom of the liquid metal remains unchanged. Correspondingly, the difference in driving forces, $\Delta\mu$, available for stable Ge nucleus formation at the bottom interface and anywhere else in the liquid metal remains constant as a function of time.

For a constant flux of Ge^0, there is a unique time point where the concentration of Ge in the liquid metal reaches a value that corresponds to a driving force sufficient for a stable Ge nucleus to form. Under the present conditions, although Ge solute reached the bottom interface in less than 1 ms after the start of the passage of current, tens of seconds passed before we observed the start of crystal growth, as inferred from Figure 2.7. Hence, we surmise that the transport time for solute to simply diffuse the whole volume of liquid metal is inconsequential (i.e., diffusion is not rate limiting).

If crystal growth is assumed to begin instantaneously after nucleation and that the delay times denoted by the x-axis intercepts in Figure 2.7 indicate the time points when crystal nucleation first occurs, then the supersaturation corresponding to nucleation of Ge at the underlying Si(100) substrate can be estimated. Figure 2.8d shows three sets of supersaturation-time lines derived from the 1D finite-difference model. The solid lines represent the model's prediction for the experimental time that must pass to reach the corresponding levels of supersaturation (i.e., C/C_{eq}) at the bottom liquid e-GaIn/Si(100) contact. These lines are dictated by the temperature, the diffusivity of Ge in e-GaIn, the solubility of Ge in e-GaIn, the thickness of the liquid metal, and the flux of Ge into the liquid metal electrode from Figure 2.4. The measured x-axis intercepts from Figure 2.7 are also superimposed as discrete points on these simulation results and indicate the approximate supersaturation of Ge in e-GaIn at nucleation. The x-axis error bars represent the propagated error from the errors in the slope and y-axis intercept of the linear-least-squares regression in Figure 2.7. By this analysis, the data globally suggest that

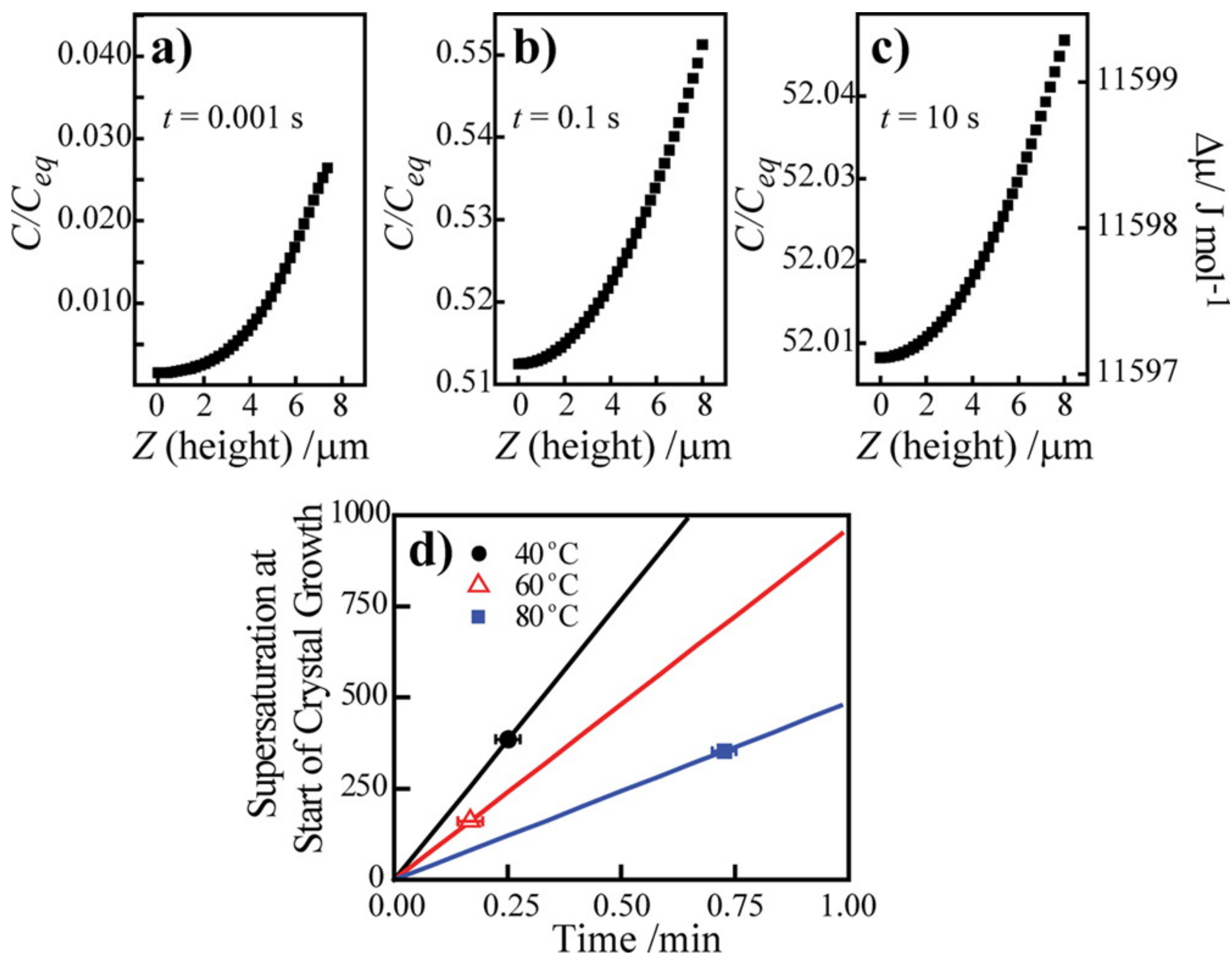

Figure 2.8. (a–c) The concentration of dissolved Ge in the liquid metal at every position inside an 8 µm thick film of E-GaIn at several times as predicted by a 1D finite difference model of diffusional transport at $T = 80$ °C and a flux of Ge into e-GaIn of 1.82×10^{-8} mol s^{-1} cm^{-2}. The *y*-axis shows the concentration both in units of supersaturation and driving force. The value of 0 µm on the *x*-axes corresponds to the E-GaIn/Si(100) substrate interface. The value of 8 µm corresponds to the electrolyte/E-GaIn interface. The profiles are shown for (a) 0.001 s, (b) 0.1 s, and (c) 10 s after the start of the Ge ec-LLS experiment. (d) A plot of the predicted supersaturation-time dependences for Ge ec-LLS experiments at the E-GaIn/Si(100) interface for $T = 40$, 60, and 80 °C under the experimental conditions described in Figure 2.3. The experimentally measured *x*-axis intercepts from Figure 2.6 are superimposed on each curves corresponding to the respective experimental conditions.

Ge nucleation in ec-LLS at these benchtop temperatures occurs at a supersaturation level of $\sim 10^2 \times C_{eq}$, i.e., a driving force of $\sim$13 500 J mol^{-1}.

The inferred supersaturation for nucleation at the e-GaIn/Si(100) interface is unexpectedly large. A consequence of nucleation under such large supersaturations is that no equilibrium can be established between the Ge crystal and Ge dissolved in the liquid metal, i.e., Ge(e-GaIn) → Ge(s).[51,52] We note, though, that the data here correspond only to form Ge nuclei and do not necessarily indicate the supersaturation of Ge in e-GaIn needed to sustain the growth of Ge crystals. For reference, supersaturations on the order of $10^0 \times C_{eq}$ have been described previously for the growth of Ge nanowires in molten metals.[7,53,54] Since there are no previous measurements of the supersaturation of Ge (or any other semiconductor) in a given liquid metal at the initial stage of nucleation, it is difficult to contextualize the values shown in Figure 2.8 at this time. We note that the equilibrium solubility for Ge in e-GaIn at these temperatures is low in comparison to liquid metals like Au which can dissolve up to about 0.2 atom % (0.2 mol L^{-1}).[54,55] A recent report suggests that liquid metals that are poorer solvents for Ge require higher supersaturations to grow Ge crystals.[56] Our data are consistent with this premise.

Activation Barriers for Ge Nucleation in ec-LLS

As noted above, different supersaturation values are required for Ge nucleation occurring at the same temperature through different pathways with distinct activation barrier values. In the presented platform for Ge ec-LLS, the only two available pathways involve Ge nucleation at the e-GaIn/Si(100) interface or nucleation somewhere within e-GaIn. For reasons stated above, the expectation is that the driving force for heterogeneous nucleation is lower than for nucleation in e-GaIn. Accordingly, if the Ge concentration at the bottom interface reaches the supersaturation level necessary for nucleation to occur heterogeneously before the supersaturation required for nucleation anywhere else in the liquid metal is reached, then heterogeneous nucleation and crystal growth at the bottom interface should occur exclusively. Alternatively, if the concentration of Ge becomes large enough inside e-GaIn to promote nucleation elsewhere, then Ge crystals will form away from the e-GaIn/Si(100) substrate. Because of density differences between Ge and the liquid metal,[57,58] any Ge crystals that form inside e-GaIn will reside up at the top liquid electrolyte/e-GaIn interface.

The competition between nucleation pathways for Ge shown in Figure 2.5 can be examined more comprehensively. Figure 2.9 displays the results from the 1D finite difference model that show the driving force for nucleation for Ge at the top liquid electrolyte/e-GaIn interface (i.e.,

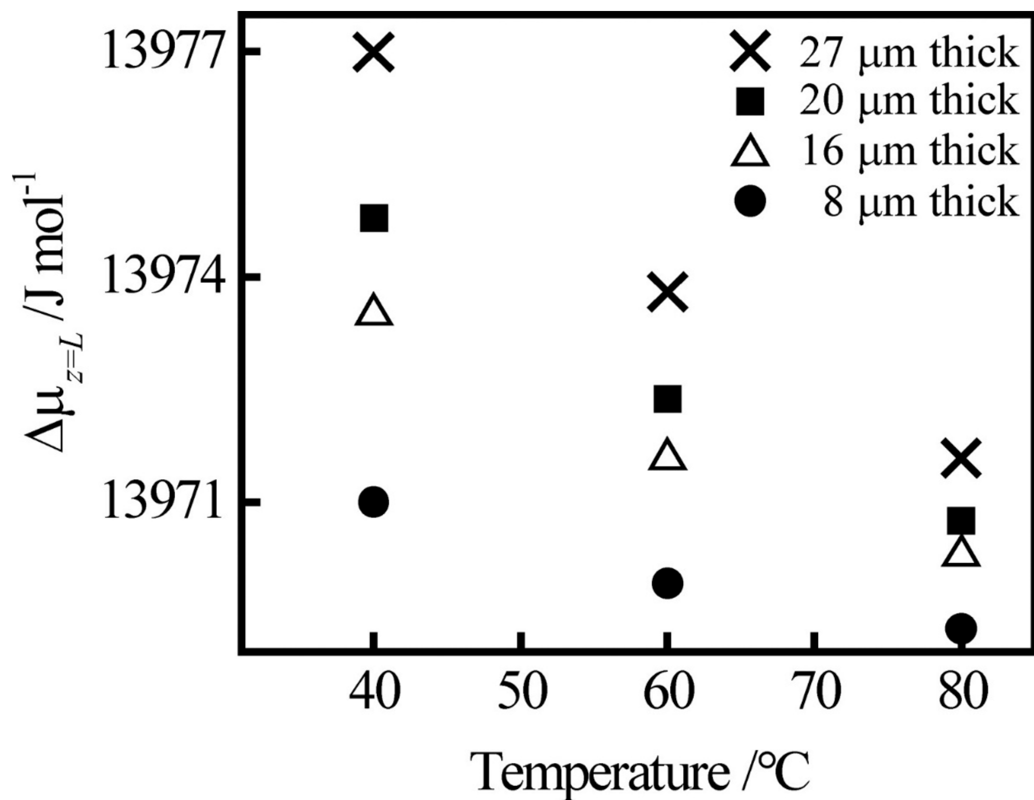

Figure 2.9. Calculated driving force for Ge nucleation at the top of the e-GaIn film when the driving force for Ge nucleation at the bottom E-GaIn/Si(100) interface is sufficient for heterogeneous nucleation. The values shown were determined through a 1D finite difference model of diffusional transport at each temperature, liquid metal thickness, and flux condition explored in Figure 2.4.

$\Delta\mu_{Z=L}$) when the driving force for nucleation at the bottom interface (i.e., $\Delta\mu_{Z=0}$) is sufficient to drive nucleation and crystal growth for all the 12 conditions explored in Figure 2.5. Using the driving force value of 13 971 J mol^{-1} determined for e-GaIn films with 8 μm thickness at T = 40 °C as a conservative estimate of the highest driving force that does **not** facilitate Ge nucleation in e-GaIn (i.e., as shown in Figure 2.5), Figure 2.9 illustrates two points. First, as the temperature increased, the driving forces for nucleation of Ge at the top liquid electrolyte/e-GaIn interface decreased for all thicknesses. As a result, the values of $\Delta\mu_{Z=L}$ for 16 and 20 μm thick e-GaIn fell below the threshold value of 13 971 J mol^{-1} as the temperature was raised from 60 to 80 °C. This feature matches the experimental observations in Figure 2.5 closely, where Ge nucleation and crystal growth was largely heterogeneous at 60 °C and was exclusively heterogeneous at 80 °C for 16 and 20 μm thick e-GaIn. Second, the data imply a sharp cutoff in driving force values for nucleation, i.e. the difference between values of Δμ that did and did not facilitate Ge nucleation in e-GaIn was surprisingly small. Comparing the driving force values for ec-LLS performed with 8 μm thick e-GaIn at T = 40 °C (where nuclei and crystal growth occurred exclusively at the e-GaIn/Si(100) interface) and ec-LLS with 20 μm thick e-GaIn at T = 60 °C (where nucleation was confirmed in e-GaIn), the inferred difference in activation barrier energies is much smaller than the thermal energy ($k_B T \approx 2933$ J mol^{-1} at T = 80 °C).

A small difference in activation barrier energies for Ge nucleation at the e-GaIn/Si(100) substrate and nucleation inside e-GaIn is challenging to comprehend fully at this juncture for several reasons. First, the activation barrier for nucleation depends on the wetting of the Ge nucleus by e-GaIn. The data collected here do not address the size and density of nuclei or how the liquid metal wets Ge clusters. X-ray spectroscopic measurements that show explicitly the sizes, locations, and solvent ordering in a liquid metal solvent are possible[59,60] but are well outside the scope of this work. Second, the prevailing view in crystal growth is that true homogeneous nucleation is exceedingly rare and may not be possible except under extremely exotic conditions.[1,61,62] Unintended low-level impurities suspended in e-GaIn instead could facilitate nucleation in e-GaIn that competes with the nucleation at the e-GaIn/Si(100) interface. Analogous experiments performed as a function of liquid metal purity may shed further light on this aspect.

The model predictions in Figures 2.7 and 2.8 correspond to time points up to Ge nucleation and crystal growth. In order to model the system at later points, the boundary conditions must be modified to account for the outflux of Ge^0 from e-GaIn, i.e., the growth of Ge crystals. Unfortunately, the experiments performed here do not provide any direct insight on the activation

barrier for crystal growth, limiting our knowledge of the new boundary condition for eq 5. Nevertheless, if the activation barrier for Ge crystal growth is lower than the barrier for Ge nucleation,[44,63] the concentration of Ge at the boundary between the new Ge crystal and the e-GaIn solvent must drop below the values indicated in Figures 2.7 and 2.8. That is, the interface of the new Ge crystal(s) will become a sink for Ge that lowers the concentration of Ge everywhere in e-GaIn.

The instant after Ge nucleation begins, the boundary condition at the bottom interface that describes the concentration of Ge must change to allow Ge crystal growth. Specifically, eq 5 no longer describes $\left(\frac{dC}{dz}\right)_{z=0}$. The appropriate boundary condition from this time forward (i.e. $t > t_{nuc}$) then has two possible values, with the value of $C(0,t)$ relative to the equilibrium solubility, C_{eq}, as the determining factor,

$$\left(\frac{dC}{dz}\right)_{z=0} = -\left(\frac{v}{AD}\right) \qquad \text{for } C(0,t) > C_{eq} \tag{12}$$

where v is the growth rate of crystalline Ge, A is the surface area at the interface where crystal growth occurs, and D is the solute diffusivity.

Using the slopes in Figure 2.8 as the rates of Ge crystal growth at the e-GaIn/Si(100), the 1D model suggests that the time that it takes for the concentration of Ge to drop is strongly dependent on temperature and liquid metal thickness. As the temperature is decreased or the liquid metal thickness increases, the supersaturation of Ge takes a significantly longer period of time to decrease below the maximum value reached at nucleation (Figure 2.10). As a result, this analysis suggests that the probability of Ge nucleation occurring somewhere other than at the e-GaIn/Si(100) interface likely increase at colder temperatures and thicker liquid metals. This analysis also suggests that if the rate of electroreduction of GeO_2 was decreased or stopped altogether just prior to nucleation, it may be possible to more quickly drop the supersaturation levels in the liquid metal. Doing so might increase the probability for exclusive heterogeneous nucleation and crystal growth in thicker liquid metals at lower process temperatures. Without more detailed information, success in that regard may be difficult. Still, this premise suggests there may be utility in performing ec-LLS (or any other melt crystal growth) with pulses rather than a constant solute feed rate if preferential nucleation and crystal growth are desired, e.g., for the deposition of crystalline films.

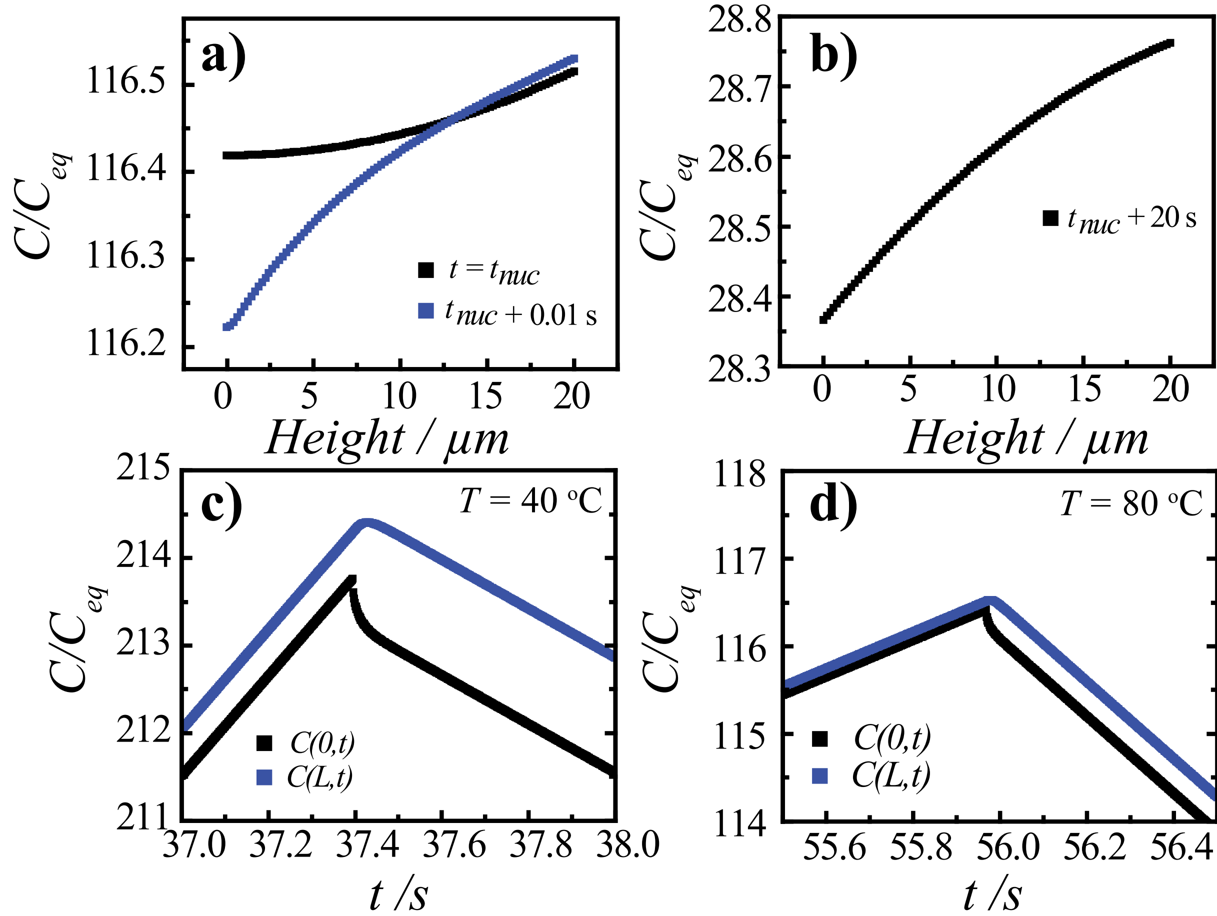

Figure 2.10. Concentration gradients at different time points throughout the simulation for Ge ec-LLS at $T = 80$ °C with a thickness of 20 µm. Three different general time regions were chosen near nucleation (a) and after nucleation (b). The concentration of Ge in a 20 µm thick volume of e-GaIn at the liquid metal /substrate interface is plotted as a function of time for simulations implementing boundary conditions *eq 11* for $T =$ (c) 40 °C and (d) 80 °C

E. Conclusion

This work leverages the use of an applied electrochemical bias in ec-LLS to reach supersaturation conditions in e-GaIn for semiconductor crystal formation as a means to understand fundamental aspects of Ge crystal nucleation and growth. Three novel insights were obtained. The first insight was the determination that e-GaIn films with thicknesses $\leq$ 8 μm will consistently facilitate heterogeneous nucleation at the interface with an underlying solid support. This work defines a critical length scale for e-GaIn film electrodes for the deposition of crystalline Ge films. That is, if strategies that enable large area thin-liquid-metal-film electrodes can be developed, then the possibility exists to electrochemically grow crystalline Ge films under entirely benchtop conditions, i.e., with an aqueous GeO_2 solution below the boiling point of water at ambient pressure. Given the generality of ec-LLS for other covalent inorganic semiconductor materials, we posit that this new mode of electrochemical deposition could become a useful preparation method for other covalent inorganic semiconductor thin films. The development of ec-LLS for this purpose is important because it would realize both the inherent simplicity and "low tech" advantages of electrodeposition and the material quality of melt crystal growths. Such a method could therefore provide high quality materials with minimal energy investment. The second insight was that the supersaturation level required for heterogeneous nucleation and growth of crystalline Ge in ec-LLS was large. This is the first report to define any aspect of nucleation in ec-LLS with rigor. Such basic information is helpful in understanding how ec-LLS parallels and differs from other related methods such as VLS or SLS.[9,12] The third understanding this work provides is the value of the microwell platform to estimate quantitatively activation energies for nucleation and crystal growth in liquid metals. Simply, this work provides a basis for future studies on liquid metal-based crystallization processes. How the metallurgical properties of different liquid metal electrodes affect the driving forces necessary for crystal nucleation and growth in ec-LLS is presently unknown. Although not performed here, further analyses of material quality (e.g., defect density, conductivity) also as a function of large and subtle changes in crystal growth rate would be informative. Accordingly, we expect that similar "competition" experiments can help illustrate differences and trends in other low melting point metals. The use of smaller liquid metal electrodes that facilitate even higher current densities would be useful to determine if the semiconductor crystal growth step can become rate-limiting and quantitatively measurable. Such work is ongoing in our laboratory. The virtues of the microwell platform in this work thus provide a path forward to test such hypotheses and help advance the premise of low temperature preparation of covalent inorganic semiconductor materials.

F. References

(1) Mullin, J. W. *Crystallization*; Butterworth-Heinemann: Oxford, 2001.
(2) Lobaccaro, P.; Raygani, A.; Oriani, A.; Miani, N.; Piotto, A.; Kapadia, R.; Zheng, M.; Yu, Z.; Magagnin, L.; Chrzan, D. C.; Maboudian, R.; Javey, A. *J. Electrochem. Soc.* **2014**, *161*, D794.
(3) Fahrenkrug, E.; Maldonado, S. *Acc. Chem. Res.* **2015**, *48*, 1881.
(4) Simanullang, M.; Seyhan, A.; Usami, K.; Kodera, T.; Kawano, Y.; Oda, S. *ECS Trans.* **2012**, *45*, 17.
(5) Han, C. F.; Hu, G. S.; Li, T. C.; Lin, J. F. *Thin Solid Films* **2016**, *599*, 151.
(6) Hu, S.; McIntyre, P. C. *J. Appl. Phys.* **2012**, *111*, 044908.
(7) Capper, P.; Mauk, M. *Liquid Phase Epitaxy of Electronic, Optical, and Optoelectronic Materials*; Chichester: England, 2007.
(8) Jang, J.; Oh, J. Y.; Kim, S. K.; Choi, Y. J.; Yoon, S. Y.; Kim, C. O. *Nature* **1998**, *395*, 481.
(9) Schmidt, V.; Wittemann, J. V.; Gösele, U. *Chem. Rev.* **2010**, *110*, 361.
(10) Kelzenberg, M. D.; Turner-Evans, D. B.; Putnam, M. C.; Boettcher, S. W.; Briggs, R. M.; Baek, J. Y.; Lewis, N. S.; Atwater, H. A. *Energy Environ. Sci.* **2011**, *4*, 866.
(11) Trentler, T. J.; Hickman, K. M.; Goel, S. C.; Viano, A. M.; Gibbons, P. C.; Buhro, W. E. *Science* **1995**, *270*, 1791.
(12) Wang, F.; Dong, A.; Buhro, W. E. *Chem. Rev.* **2016**, *116*, 10888.
(13) Laocharoensuk, R.; Palaniappan, K.; Smith, N. A.; Dickerson, R. M.; Werder, D. J.; Baldwin, J. K.; Hollingsworth, J. A. *Nat. Nanotechnol.* **2013**, *8*, 660.
(14) DeMuth, J.; Ma, L.; Fahrenkrug, E.; Maldonado, S. *Electrochim. Acta* **2016**, *197*, 353.
(15) Carim, A. I.; Collins, S. M.; Foley, J. M.; Maldonado, S. *J. Am. Chem. Soc.* **2011**, *133*, 13292.
(16) Fahrenkrug, E.; Biehl, J.; Maldonado, S. *Chem. Mater.* **2015**, *27*, 3389.
(17) Ma, L.; Gu, J.; Fahrenkrug, E.; Maldonado, S. *J. Electrochem. Soc.* **2014**, *161*, D3044.
(18) Gu, J.; Fahrenkrug, E.; Maldonado, S. *J. Am. Chem. Soc.* **2013**, *135*, 1684.
(19) Fahrenkrug, E.; Gu, J.; Jeon, S.; Veneman, P. A.; Goldman, R. S.; Maldonado, S. *Nano Lett.* **2014**, *14*, 847.
(20) Fahrenkrug, E.; Gu, J.; Maldonado, S. *J. Am. Chem. Soc.* **2013**, *135*, 330.
(21) Zhang, J.; Chen, S.; Zhang, H.; Zhang, S.; Yao, X.; Shi, Z. *RSC Adv.* **2016**, *6*, 12061.
(22) Mahenderkar, N. K.; Liu, Y. C.; Koza, J. A.; Switzer, J. A. *ACS Nano* **2014**, *8*, 9524.
(23) Smith, J.; Hinson-Smith, V. *Anal. Chem.* **2002**, *74*, 539A.
(24) Green, M. A.; Emery, K.; Hishikawa, Y.; Warta, W.; Dunlop, E. D. *Prog. Photovoltaics* **2015**, *23*, 1.
(25) Rogalski, A. *Infrared Phys. Technol.* **2002**, *43*, 187.
(26) Vescan, L.; Stoica, T. *J. Lumin.* **1998**, *80*, 485.
(27) Claeys, C. L.; Simoen, E. *Germanium-Based Technologies: From Materials to Devices*; Elsevier: Amsterdam, 2007.
(28) Anderson, T. J.; Ansara, I. *J. Phase Equilib.* **1991**, *12*, 64.
(29) Khan, M. R.; Trlica, C.; Dickey, M. D. *Adv. Funct. Mater.* **2015**, *25*, 671.
(30) Bard, A. J.; Faulkner, L. R. *Electrochemical Methods: Fundamentals and Applications*; Wiley: New York, 2001.
(31) DeMuth, J.; Fahrenkrug, E.; Maldonado, S. *Crystal Growth & Design* **2016**, *16*, 7130.

(32) Bard, A. J.; Parsons, R.; Jordan, J. *Standard Potentials in Aqueous Solution*; Dekker: New York, 1985.
(33) Crank, J. *The Mathematics of Diffusion*; Clarendon Press: Oxford, 1975.
(34) Kaptay, G. *Z. Metallkd.* **2005**, *96*, 24.
(35) Su, X.; Yang, S.; Wang, J.; Tang, N. Y.; Yin, F.; Li, Z.; Zhao, M. *J. Phase Equilib. Diffus.* **2010**, *31*, 333.
(36) Koster, J. N. *Cryst. Res. Technol.* **1999**, *34*, 1129.
(37) Donnelly, R. F.; Singh, T. R. R.; Wiley Online, L. *Novel Delivery Systems for Transdermal and Intradermal Drug Delivery*; John Wiley and Sons, Ltd.: Chichester, West Sussex, United Kingdom, 2015.
(38) Olesinski, R. W.; Abbaschian, G. J. *Bull. Alloy Phase Diagrams* **1984**, *5*, 180.
(39) Barin, I.; Knacke, O.; Kubaschewski, O. *Thermochemical Properties of Inorganic Substances Supplement*; Springer: Berlin, 1977.
(40) Stringfellow, G. B.; Greene, P. E. *J. Electrochem. Soc.* **1970**, *117*, 1075.
(41) Stringfellow, G. B. *Mater. Res. Bull.* **1971**, *6*, 371.
(42) Alonso, M. I.; Bauser, E. *J. Appl. Phys.* **1987**, *62*, 4445.
(43) Cremoux, B. *IEEE J. Quantum Electron.* **1981**, *17*, 123.
(44) De Yoreo, J. J.; Vekilov, P. G. *Rev. Mineral. Geochem.* **2003**, *54*, 57.
(45) Thurmond, C. D. *J. Phys. Chem.* **1953**, *57*, 827.
(46) Porter, J. D. *Science* **1951**, *113*, 450.
(47) Bonafede, S. J.; Ward, M. D. *J. Am. Chem. Soc.* **1995**, *117*, 7853.
(48) He, B. B. *Two-Dimensional X-Ray Diffraction*; John Wiley & Sons, Inc: Hoboken, New Jersey, 2009.
(49) Copeland, L. E.; Bragg, R. H. *Anal. Chem.* **1958**, *30*, 196.
(50) Nazmov, V.; Reznikova, E.; Mohr, J.; Schulz, J.; Voigt, A. *J. Mater. Process. Technol.* **2015**, *225*, 170.
(51) Kodambaka, S.; Tersoff, J.; Reuter, M. C.; Ross, F. M. *Phys. Rev. Lett.* **2006**, *96*, 096105.
(52) Kodambaka, S.; Tersoff, J.; Reuter, M. C.; Ross, F. M. *Science* **2007**, *316*, 729.
(53) Wu, Y.; Yang, P. *J. Am. Chem. Soc.* **2001**, *123*, 3165.
(54) Kim, B. J.; Wen, C. Y.; Tersoff, J.; Reuter, M. C.; Stach, E. A.; Ross, F. M. *Nano Lett.* **2012**, *12*, 5867.
(55) Schwalbach, E. J.; Voorhees, P. W. *Nano Lett.* **2008**, *8*, 3739.
(56) Biswas, S.; O'Regan, C.; Petkov, N.; Morris, M. A.; Holmes, J. D. *Nano Lett.* **2013**, *13*, 4044.
(57) Madelung, O.; Rössler, U.; Schulz, M. *Group IV Elements, IV-IV and III-V Compounds. Part b - Electronic, Transport, Optical and Other Properties*; Springer: Berlin, 2002.
(58) Xu, Q.; Oudalov, N.; Guo, Q.; Jaeger, H. M.; Brown, E. *J. Phys. Chem.* **2012**, *24*, 063101.
(59) Murphy, B. M.; Festersen, S.; Magnussen, O. M. *Nanoscale* **2016**, *8*, 13859.
(60) Elsen, A.; Festersen, S.; Runge, B.; Koops, C. T.; Ocko, B. M.; Deutsch, M.; Seeck, O. H.; Murphy, B. M.; Magnussen, O. M. *Proc. Natl. Acad. Sci. U. S. A.* **2013**, *110*, 6663.
(61) Liu, X. Y. *J. Chem. Phys.* **2000**, *112*, 9949.
(62) Sear, R. P. *J. Phys. Chem. B* **2006**, *110*, 4985.
(63) Huang, Y.; Tu, K. N. *Silicon and Silicide Nanowires Applications, Fabrication, and Properties*; Pan Stanford Publishing: Boca Raton, 2013.

CHAPTER 3

Electrochemical Liquid Phase Epitaxy (ec-LPE): A New Methodology for the Synthesis of Crystalline Group IV Semiconductor Epifilms

A. Introduction

Optoelectronic technologies hinge on the methods to synthesize crystalline inorganic materials and to fabricate their heterojunctions with extreme quality and fidelity.[1] The ability to deposit unstrained films of crystalline Ge on crystalline Si is particularly challenging due to the large lattice mismatch (4.2%).[2] Although some strategies exist for high quality Ge/Si heterojunctions based on multistep epitaxy and/or annealing,[2–4] aspect ratio trapping,[5] or compositionally graded $Si_{1-x}Ge_x$ buffers exist,[6,7] they are complex, involve high temperatures, and are time-consuming. The reliance on toxic/ corrosive gaseous precursors and elevated temperatures further complicate integrating Ge epilayers on preexisting Si device platforms.[8,9] We previously demonstrated the concept that bulk liquid metals can simultaneously facilitate the electroreduction of oxidized semiconductor precursors and the formation of zerovalent semiconductor nano- and microcrystals,[10–12] affording a pathway to simplify preparation of crystalline semiconductors. However, to date, an analogous process for macroscopic, crystalline semiconductor films has never been conceived. In this work, we describe the invention of a new approach specifically for the preparation of single-crystalline semiconductor films across macroscopic areas that can be intrinsically simple without sacrificing crystallographic quality. Herein, we show a hybrid strategy that avoids excessive temperatures and can be run under benign (benchtop) conditions with intrinsically inexpensive/simple equipment, nonflammable precursors, and no toxic waste products for the synthesis/deposition of epitaxial Ge thin films. We present for the first time the growth of Ge "epifilms" on Si wafers using large-area, thin liquid eutectic gallium indium (e-GaIn) films that act as dual electrodes/solvents in an electrochemical liquid phase epitaxial (ec-LPE) process (Figure 3.1). We first present a compression cell design that stabilizes liquid metal films for this purpose. We then show data that illustrate ec-LPE with this cell

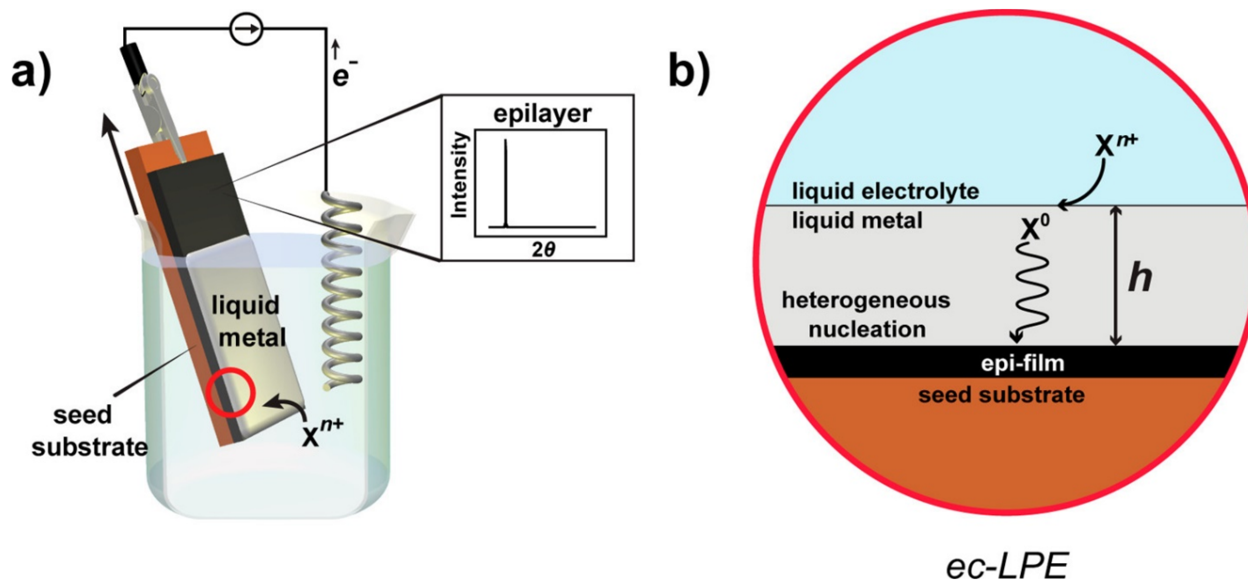

Figure 3.1. (a) Summary view of an electrochemical liquid phase epitaxy (ec-LPE) film growth concept with a thin liquid metal electrode with thickness *h*. (b) Schematic depiction of the relevant steps in ec-LPE, where an oxidized species X^{n+} dissolved in the electrolyte is reduced to X^0 by heterogeneous electron transfer, partitions into the liquid metal film, and then diffuses some distance away from the liquid electrolyte/liquid metal interface before precipitating out. When *h* is sufficiently thin, preferential heterogeneous nucleation and crystal growth is possible at the bottom interface between the liquid metal and a seed substrate.

performed at ambient pressure, with an aqueous feedstock solution, and only at temperatures below the boiling point of water. Although the conditions for ec-LPE are less extreme than, require less ancillary equipment than, and are at least as tunable as vapor/vacuum based deposition strategies, the results argue that the crystallographic properties of the as prepared Ge films and their heterojunctions with Si are of high quality. The prospects for ec-LPE as a realizable methodology for semiconductor film deposition that maintains the crystallographic quality of liquid-phase epitaxy growths[13] with the simplicity and control of low temperature electrodeposition[14] are discussed.

This chapter was published in the *Journal of the American Chemical Society*.[14] All text and figures are reprinted with permission from ACS.

B. Methods

Chemicals Indium (99.99% Gallium Source), germanium dioxide (99.998% Sigma-Aldrich), sodium borate (>99.5% Sigma and Aldrich), SU-8-2007 (MicroChem Corp.), SU-8 developer (MicroChem Corp.) gallium (99.999%, Alfa Aesar), copper pellets (99.999%, R.D. Mathis and company, hydrofluoric acid (49%, Transene Inc.), methanol (ACS grade, BDH), 2-propanol (ACS grade, BDH), and hexamethyldisilazane (HMDS, Fischer Scientific) were used as received. Water was purified from a Barnstead Nanopure III purification system (>18 MG cm) and was used throughout.

Degenerately doped, n-type Si(100) wafers (< 0.007 Ω·cm, 0.625 ± 0.020 mm thick, Crysteco) and n-type Si(111) (<0.006Ω·cm, 0.525 ± 0.015 mm thick, Wafer Works Corp) were diced into 4 x 8 cm sections and degreased through sequential sonication in hexanes, acetone, methanol and water followed by etching the native oxide in 5-10% HF for 1 min before continuing to the next step. For some trials, a thin copper film was deposited by thermal evaporation of ~ 200 nm of Cu prior to the photolithography step. The wafer pieces were then subject to photolithographic patterning before use as ec-LPE substrates. After lithography but immediately before use for ec-LPE, wafer sections were plasma etched (model PE-50, Plasma Etch Inc.) in O2 (20 sccm, 400 W) to clean the surface.

Photolithography Prior to depositing SU-8-2007, HMDS was spin coated to promote photoresist adhesion. SU-8-2007 was then spin coated onto Si wafer sections to achieve photoresist

thickness from 8-10 μm. The wafer sections were then heated on a hotplate at 95 °C for 3 min and then exposed to UV light (220 – 450 nm, OAI 30 Lamp) for 13-20 s at 30 W cm-2 through a custom photomask (Fineline Imaging, Colorado Springs, CO). An additional heating step at 95 °C for 5 min was then performed before developing for 4-5 min and then rinsed with isopropanol and dried with a stream of N_2. The resultant developed-photoresist film consisted of inlet and outlet channels bracketing a larger main cavity where films would be deposited by ec-LPE (Figure 3.2 and 3.3a). In this way, the photoresist also functioned as the physical spacer between the Si substrate and the underside of the porous membrane, defining the distance between the underside of the membrane and the exposed Si substrate. This gap accordingly set the maximum thickness for the liquid metal film in ec-LPE experiments.

Cell Assembly To form a contiguous liquid e-GaIn film with 10 μm thickness, liquid e-GaIn was pipetted onto a given patterned wafer section which rested on a flat conductive plate set into the solid bottom plate. A lint-free cloth was used to spread the liquid metal evenly so that the height in the main cavity was slightly above the photoresist layer. The ports on the membrane were optically aligned with the channels on the substrate and then the membrane was placed on top of the wafer section. The clamping plate was then used to secure this stack. This action typically caused excess liquid metal to flow out both ports. The stack was compressed and kept under tension by six steel screws. To ensure complete filling of the thin cavity with liquid metal, the exit port was then closed off and the liquid metal was kept under pressure with the syringe at a nominal pressure of 700 psi. The reservoir for the liquid electrolyte was then separately press fit onto the opening in the top clamping plate, with a Viton o-ring between the bottom edge of the electrolyte cell and the top-side of the porous membrane. Electrical contact to the ec-LPE substrate was made through a clip affixed to one of the screws.

Parameters for ec-LPE For all ec-LPE trials, either a CHI-760 or a CHI-420 potentiostat (compliance voltage = ±13 V for both models, CH Instruments Inc.) were used. The aqueous electrolyte for ec-LPE was prepared by adding 0.1 M of $Na_2B_4O_7$ and enough powdered GeO_2 to reach the target concentration. The solutions were metastable, without signs of precipitation for up to 11 days. After this point, the electrolyte became turbid and was not used. The counter electrode consisted of either a graphite rod or platinum mesh. A Ag/AgCl(4M KCl) reference electrode was used throughout. To set the temperature for each ec-LPE experiment, the cell was placed and

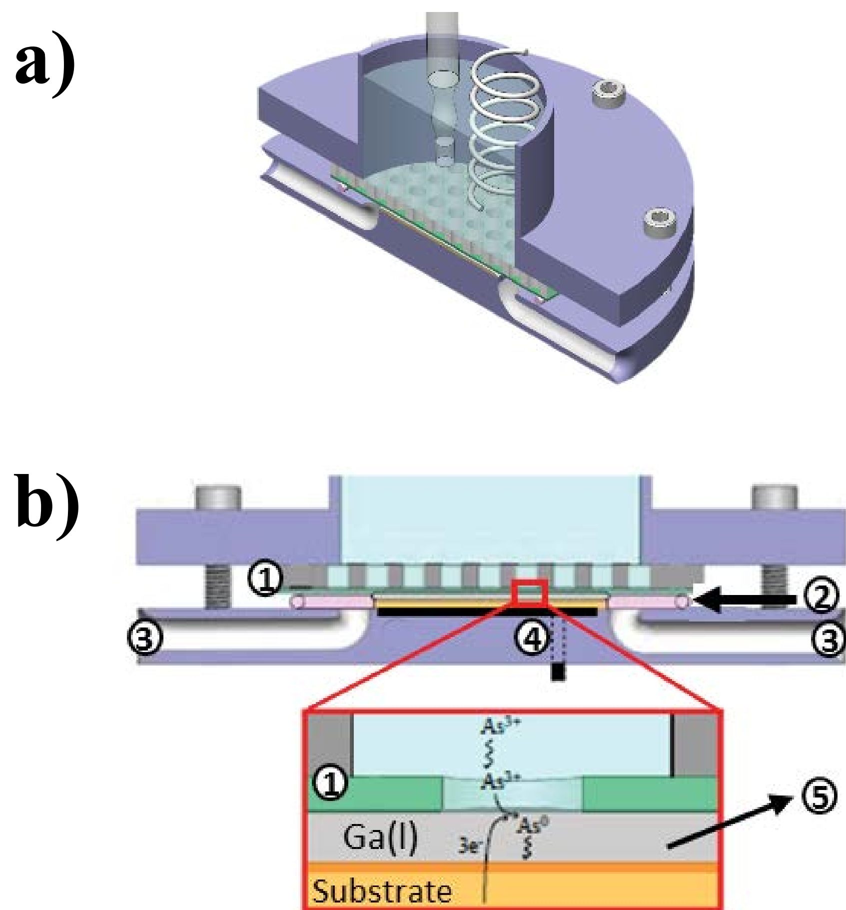

Figure 3.2. Schematic of the initial ec-LPE cell design (a, b). The cell was designed to form a liquid metal film electrode over a macroscopic area of an underlying substrate. Cross section of ec-LPE cell (b) where; 1) Compression plate (two-piece membrane), 2) Compression spacer, 3) Ga(l) channels, 4) Ohmic contact, 5) Cavity space above substrate filled with Ga(l)

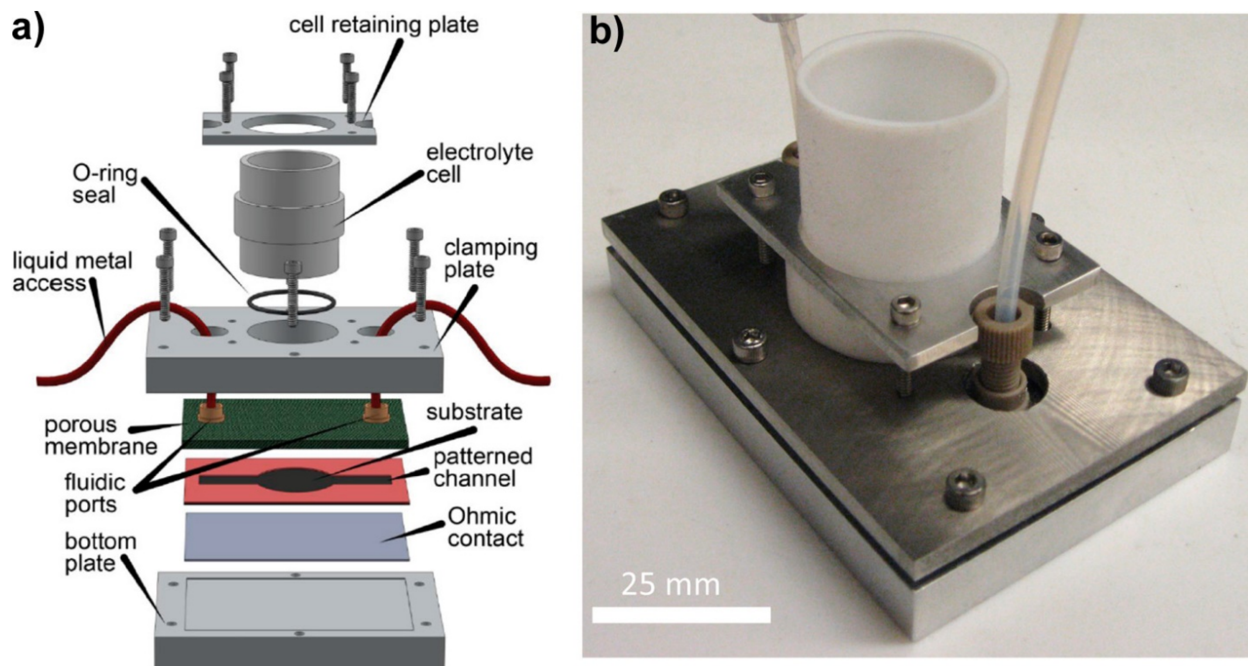

Figure 3.3. (a) Exploded view of the ec-LPE cell developed for this work. The cell has a compression stack design to facilitate the formation of a stable liquid metal film over a large two-dimensional area. Upon assembly, liquid metal is flowed into a thin cavity with the side walls and bottom defined by photoresist patterned on a seed substrate, respectively, and the top comprised of a porous membrane that is permeable to electrolyte flow but resists infusion by the liquid metal. (b) Optical photograph of an ec-LPE cell for film areas ~ 4.8 cm^2.

assembled on a hotplate set to 90 °C and allowed to equilibrate for equilibrate for 5 min. The temperature of the cell was measured with a thermocouple to be 90 ºC. Following deposition, excess liquid e-GaIn was removed from the as-deposited Ge films by an electrochemical etch at -0.097V vs E(Ag/AgCl) in 1M HCl at room temperature.

Materials Characterization Optical characterization of the as-prepared Ge films was performed with a laser confocal microscope (LEXT OLS 4000, Olympus) equipped with a differential interference contrast (DIC) polarizer-analyzer optics set.

Powder X-ray diffractograms were obtained with a Bruker D8 Advance X-ray diffractometer using a Cu Kα X-ray source (λ = 1.5406 Å). To further assess the quality of the as-prepared Ge films, a triple axis X-ray diffraction scan was performed to measure the intensity of the Ge(400) and Si(400) diffraction signals. Coupled scan (ω-2θ) diffraction data were collected with a three axis. Bede D1 high resolution X-ray diffractometer using a Cu Kα X-ray source (λ = 1.5406 Å) and Si(220) beam conditioner and a 0.5mm slit inserted before the detector

Scanning electron micrographs (SEM), electron backscatter diffraction patterns (EBSD), and energy dispersive spectra (EDS) were collected using a JEOL-7800FLV scanning electron microscope equipped with an Oxford X-MaxN silicon drift detector (Oxford Instruments) and a (Oxford NordlysMax2) detector. Focused ion beam (FIB) milling were conducted in FEI NOVA Nanolab Dualbeam and FEI Helios Nanolab 650 Dualbeam workstations, both equipped with Schottky field emitters and Ga focused ion beams. Sample preparation for transmission electron microscopy (TEM) was prepared by FIB milling and liftout using the following procedure. First, a protective Pt layer was deposited using electron beam assisted chemical vapor deposition and followed by deposition of a thicker Pt-layer (1- 2 μm) using an ion beam assisted chemical vapor deposition (IBA-CVD) employing $C_5H_4CH_3Pt(CH_3)_3$ gas as the Pt source. Trenches were then milled into the film and substrate. An Omniprobe AutoProbe 200 micromanipulator equipped with a standard tungsten probe tip (Ted Pella) was used to Pt-weld to the thin section to the probe tip using IBA-CVD. The specimen was then cut free from the surrounding film through additional FIB milling and affixed onto a Cu-TEM grid for analysis. High resolution TEM images were collected with a JEOL 3011 operated at 300 kV. High resolution scanning transmission electron microscopic (STEM) imaging and annular dark field STEM imaging were performed in a JEOL 3100R05 microscope at 200 kV.

A FEI Teneo field-emission scanning electron microscope (SEM) was used for all electron channeling contract imaging (ECCI). The microscope was equipped with a lens-mounted, solid-state FEI directional backscatter (DBS) electron detector, with all detector segments summed. All images were acquired with an accelerating voltage of 30 kV, a current of 13nA, and a sample working distance of 8 mm.

Cell Design. To overcome the electrocapillarity of e-GaIn which causes dewetting from the underlying substrate, a new compression cell design was necessary. The cell incorporated a set of custom components sandwiched between a top clamping plate and a solid bottom plate, two fluidic connections for the liquid metal, a wafer section with patterned photoresist, a top cell for housing the liquid electrolyte, and a 2 mm thick porous silicon carbon membrane (fsm sheet, LiqTech International) that served two separate functions (Figure 3.3a). The first function of the membrane was to serve as the top boundary of the thin cavity (where the bottom and sides were composed of the wafer section and developed photoresist, respectively) that housed the liquid metal film. The porosity of the membrane was insufficient to allow appreciable infusion by the liquid metal, even under pressure. The second function of the membrane was to permit flow of the liquid electrolyte to allow the formation of a liquid electrolyte/liquid metal interface that facilitated heterogeneous reduction of GeO_2 dissolved in the electrolyte. The flux of species through the membrane was determined by the thickness and ionic strength of the electrolyte, but current densities of 10^{-3} A cm^{-2} were routinely supported without approaching the compliance voltage limits of the employed potentiostat. The uncompensated resistance across the membrane measured before each ec-LPE experiment and was

C. Results

Although ec-LPE could be performed galvanostatically, all ec-LPE experiments performed here were potentiostatic with a constant potential applied for a set amount of time. Figure 3.4a illustrates a representative chronoamperometric response recorded during an ec-LPE experiment performed in this way. At this pH, the predominant species for an aqueous solution of dissolved GeO_2 is $HGeO_3^-$, [15] and the majority of current corresponded to the $4e^-$ reduction of this species to Ge^0 at the electrolyte/e-GaIn interface. After the initial current decay, a local maximum was consistently observed in the current transient within the first 1000 s before attaining a steady-state value. The local maximum in the current–time profile was reminiscent of electrodeposition

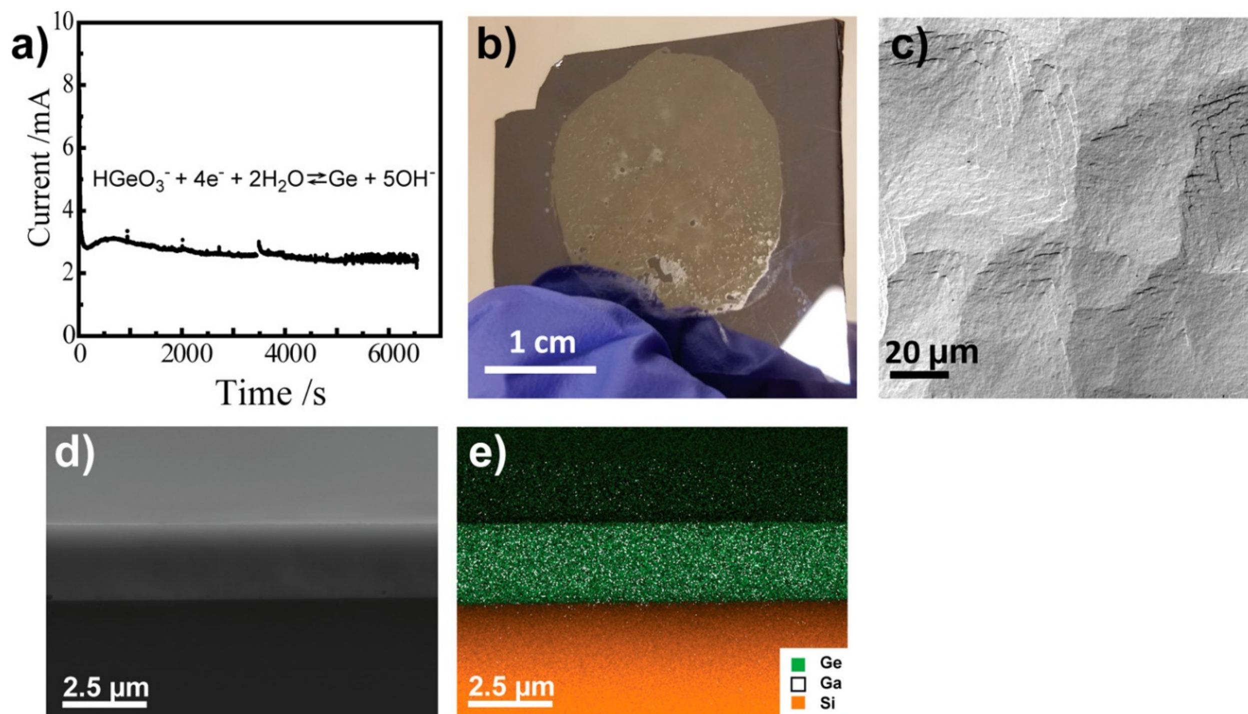

Figure 3.4. (a) Representative chronoamperometric trace of an ec-LPE deposition of a Ge film with the cell described in Figure 3.3 and the following conditions: $E = -1.6$ V vs E(Ag/AgCl), $T =$ 90 °C, and an aqueous electrolyte containing 70 mM $Na_2B_4O_7$ and dissolved GeO_2 at a formal concentration of 225 mM. (b) Optical photograph of a Ge film prepared by ec-LPE with the same conditions as in (a) on top of a n^+-Si(100) seed substrate. (c) Representative scanning confocal laser interferometry image depicting the surface roughness of the top of an as-prepared Ge film by ec-LPE with the same conditions as in (a). (d) Scanning electron micrograph of a cross-section of a Ge film prepared by ec-LPE with the same conditions as in (a). The underlying seed substrate is n^+-Si(100). (e) Overlaid elemental maps from energy dispersive X-ray spectroscopic measurements of the same section in (d).

processes involving discrete nucleation steps,[16,17] but no attempt was made to apply existing nucleation models since none describe dissolution into the electrode. Random, minor current spikes were routinely observed and were correlated to the observation of bubbles at the electrolyte/ membrane interface. Hence, the flux of Ge^0 into the liquid e-GaIn film was $< 1.5 \times 10^{-9}$ mol s^{-1} cm^{-2}.

Upon completion of an ec-LPE experiment, the cell was disassembled and e-GaIn was removed from the wafer section substrate through a selective anodic etch in acid. A hard, strongly attached film was consistently deposited over only the area where electrolyte contacted the top e-GaIn surface (Figure 3.4b). Optical profiling of the film surfaces through confocal laser differential interference contrast imaging showed the surface textured of the as-prepared films (Figure 3.4c). A tiered surface profile with steps was observed, with average step heights of 40 ± 10 nm. Select films were diced and viewed by scanning electron microscopy. A representative cross-sectional image of a film is shown in Figure 3.4d. The films appeared dense and continuous without obvious voids or cracks. Elemental analyses of these films (Figure 3.4e) showed the films were Ge throughout. Ga was detected at a concentration of 3−5 at. % evenly throughout the film without any accumulation at the surface but no other metals were observed within the limits of detection of the energy dispersive spectrometer.

The thicknesses of the Ge films were sensitive to the parameters used for ec-LPE. Figure 3.5 illustrates experiments where all deposition conditions were held constant except for the formal concentration of dissolved GeO_2. Figures 4a-c show cross sections for the fully dense Ge films deposited for the same amount of time but with formal concentrations of dissolved GeO_2 of 50, 100, and 225 mM, respectively. The thicknesses measured from the electron micrographs tracked linearly with the formal concentrations of the solution (Figure 3.5d). Similarly, integration of the current transients showed the charge-time profiles were linear. The respective magnitudes of the charge-time slopes matched the respective heights for each ec-LPE deposition, indicating both that the primary balance of current was for the formation of Ge^0 rather than H_2 and that the faradaic efficiency for reduction of $HGeO_3^-$ was invariant to the formal concentration of the electrolyte.

Two sets of ec-LPE experiments were performed with identical deposition conditions except for the crystallographic orientation of the underlying substrate (Si(100) and Si(111)). Figure 3.6 shows data for Ge films produced in these experiments. Although the majority of films and

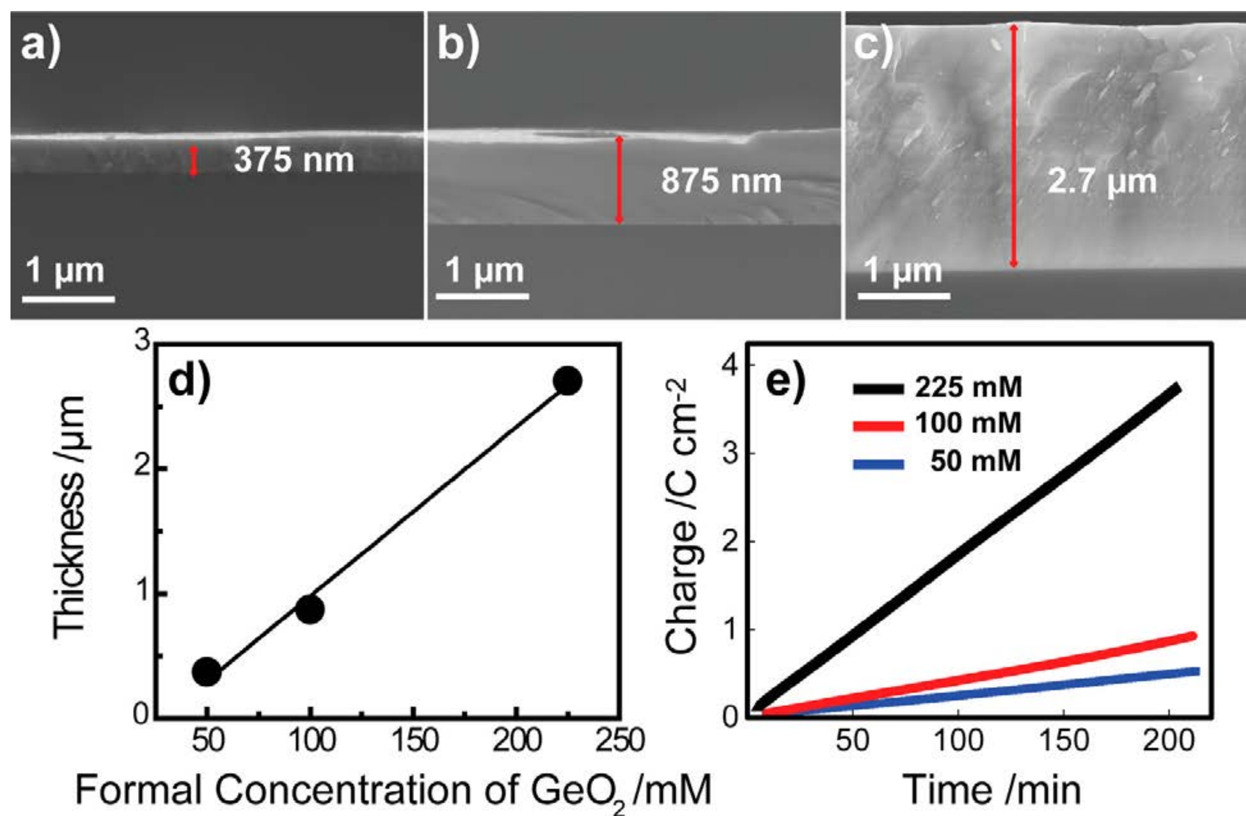

Figure 3.5. Scanning electron micrographs of cross sections of Ge films prepared by ec-LPE with the same conditions as in Figure 3.4a except formal concentrations of dissolved GeO_2 of 50, 100, and 225 mM in (a), (b), and (c), respectively. (d) Measured film thicknesses of Ge films prepared by ec-LPE as a function of the formal concentration of dissolved GeO_2. (e) Measured charge-time profiles for the ec-LPE depositions of the Ge films in (a)–(c).

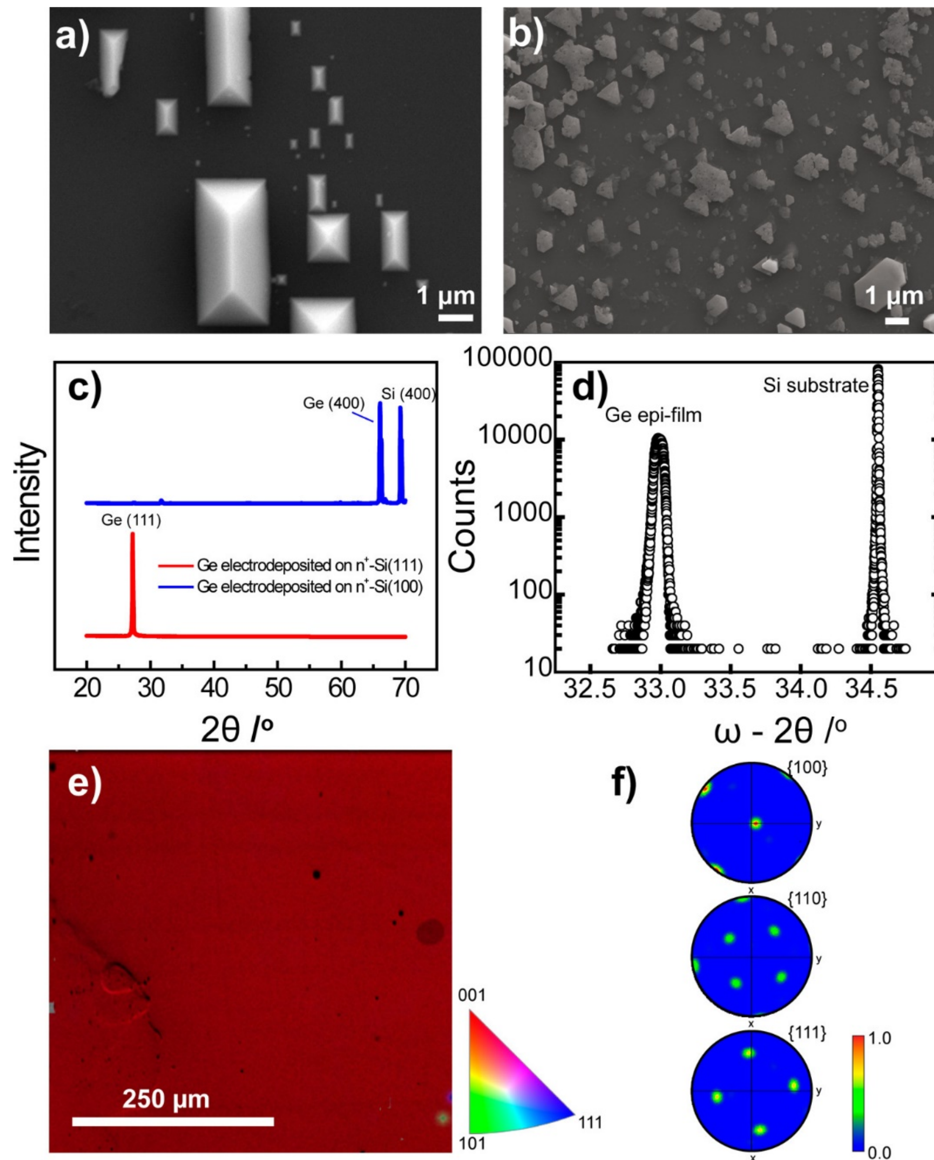

Figure 3.6. Top-down view scanning electron micrographs of initial Ge deposits in ec-LPE depositions performed with the same conditions as in Figure 3.4a with (a) n^+-Si(100) and (b) n^+-Si(111) seed substrates. (c) Grazing angle X-ray diffractograms of Ge films prepared by ec-LPE with n^+-Si(100) and n^+-Si(111) seed substrates. (d) A representative X-ray rocking curve of a Ge film prepared by ec-LPE on a n^+-Si(100) e) Color-coded electron back scatter diffraction (EBSD) map (top-down view) of a Ge film prepared by ec-LPE on n^+-Si(100). (f) Contour pole figures from the EBSD mapping shown along the 110 and 111 poles. Each pole figure is made from 5438 independently solved EBSD patterns taken from a mapped area of ~1.5 mm^2.

film areas were continuous, Figures 5a and 5b show micrographs of areas where the film was not contiguous. These undesirable instances occurred either because of incomplete wetting by the liquid metal and/or insufficient substrate surface cleaning beforehand were still useful in showing the distinct crystal habits of Ge in ec-LPE. The square and rectangular Ge prisms in Figure 3.6a are consistent with epitaxial nucleation and crystal growth off the Si(100) substrate with the fastest growth rate in the ⟨111⟩ direction. Similarly, the triangular and fused triangular nuclei with three point symmetry conform to expectations of heterogeneous nucleation and crystal growth of Ge on a clean Si(111) substrate. Replicate measurements where the ec-LPE deposition was allowed to form the solid, contiguous films shown above where interrogated by X-ray diffraction. Figure 3.6c shows representative X-ray diffractograms for Ge films deposited on the two Si substrate types. For both films, the collected patterns did not show the full set of (111), (220), and (311) diffraction peaks expected for randomly oriented polycrystalline Ge.[18] Instead, each pattern showed only one diffraction peak that corresponded to crystalline Ge and strongly implicated the films displayed a fibril (out of plane) texture. For Ge films deposited on n^+-Si(111), the only signature was located at 27.20°, consistent with diffraction from the (111) plane of crystalline Ge. For Ge films deposited on n^+- Si(100), two peaks were observed but only one was ascribable to crystalline Ge. The signal at 65.91° was consistent with diffraction from the (400) plane of crystalline Ge while the signal at 69.10° was consistent diffraction from the (400) plane of the underlying Si(100) substrate. Asymmetric coupled scan diffraction[19] data with a triple-axis diffractometer were also collected for Ge films deposited on Si(100) substrates (Figure 3.6d).[20] Although the full width at half-maximum (fwhm) of the (400) diffraction peak for the Ge film was larger than that for the Si substrate, the fwhm for the Ge (400) peak was only 0.065°, consistent with values previously observed for nearly perfect epitaxial Ge films deposited on $Si_{1-x}Ge_x$ by chemical vapor deposition[21] and smaller than fwhm values for Ge films directly on Si prepared by molecular beam epitaxy.6 Using the position of the Ge(400) reflection with respect to the Si(400) in the coupled scans, it was found that the films were 100% strain relaxed, i.e., no apparent compressive strain.[20]

To separately assess the variations of in-plane orientation in as-prepared Ge films, electron back scatter diffraction (EBSD) data were obtained. Figure 3.6e shows a top-down view scanning electron micrograph of a polished Ge film deposited on a n^+ - Si(100) substrate that has been false colored to denote the crystalline orientation of the film normal to the substrate by 5,438 local EBSD patterns sampled over the interrogated area. In this image, the predominant orientation

determined by EBSD was (001), obtained by fitting the EBSD pattern with the pattern simulated based on crystallographic data for Ge. Pole figures (Figure 3.6f) generated from the EBSD data showed only sharp poles and no discernible rings or unexpected peaks, indicating that all regions in the as-prepared films were in registry with respect to both the underlying substrate (out of plane) and the surrounding film (in plane) over the entire probed area (~1.56 mm^2).

To probe the local crystallinity and microstructure at the bottom Ge/Si interface, separate Ge films were grown on n^+ - Si(111) and then cross-sectioned for analysis by TEM. Figure 3.7a shows a low magnification micrograph of the interface. The film was continuous across the interface with no apparent voids. The bending contours were consistent with the lattice mismatch between the Ge and the underlying Si. Selected area electron diffraction patterns were collected both purely from the Ge film (Figure 3.7b) and across the interface between Ge and Si (Figure 3.7c). The diffraction patterns for Ge away from and at the interface showed the same crystalline orientation and thus a separate indicator of both the crystallinity of the Ge film and the epitaxial relationship with the substrate. Annular dark field scanning transmission electron microscopy (STEM-ADF, Figure 3.7d) showed continuous contrast in the Ge film without apparent grain boundaries or voids. The corresponding high resolution, atomically resolved STEM-ADF images from that interface (Figure 3.7e) highlighted three important findings. First, there was no amorphous/ disordered layer between the Ge film and the Si substrate. Second, the lattice ordering of the substrate and film was continuous. Third, the junction was atomically abrupt without apparent crossover of either Ge into the Si substrate or Si into the Ge film.

To further assess the content of crystallographic defects (misfit dislocations) in the as-prepared Ge films but over larger areas than are possible by (S)TEM, a diffractive imaging SEM method was used (electron channeling contrast imaging, ECCI).[22] In ECCI, the surface penetrating threading segments of the misfit dislocation loops can be observed via the diffraction contrast resulting from their strong, localized strain fields, and appear as spots with intense bright and/or dark lobes. Figure 3.8a shows an overlay of an experimentally collected low magnification electron channeling pattern (ECP) from a Ge film prepared by ec-LPE on n^+ -Si(100) on top of a simulated Ge(100) ECP. The ECP data was collected over an area approximately 2 mm wide, providing strong agreement with the EBSD measurements indicating that the entire film was a contiguous single crystal. The white circle indicates the [220] orientation used to collect the ECC image

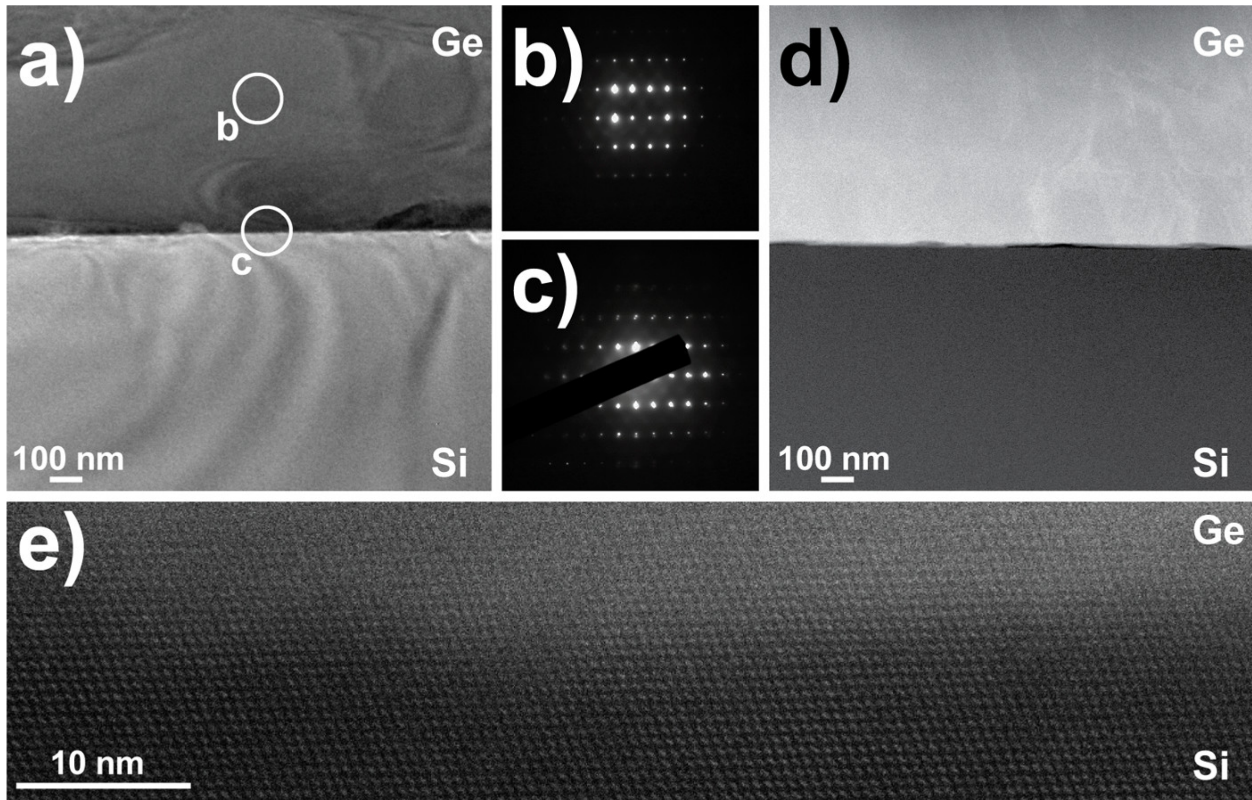

Figure 3.7. (a) Bright field transmission electron micrograph viewed along the ⟨211⟩ zone axis of a cross section of an epitaxial Ge film prepared by ec-LPE on n^+-Si(111) with the same conditions as in Figure 3.4a. Electron diffraction patterns for the Ge film and the Ge/Si interface are shown in (b) and (c), respectively. (d) Low magnification annular dark-field scanning transmission electron micrograph of a cross section of an epitaxial Ge film prepared by ec-LPE on a n^+-Si(111) with the same conditions as in Figure 3.4a. (e) Representative high resolution annular dark-field scanning transmission electron micrograph of the interface between the Ge film and Si substrate shown in (d).

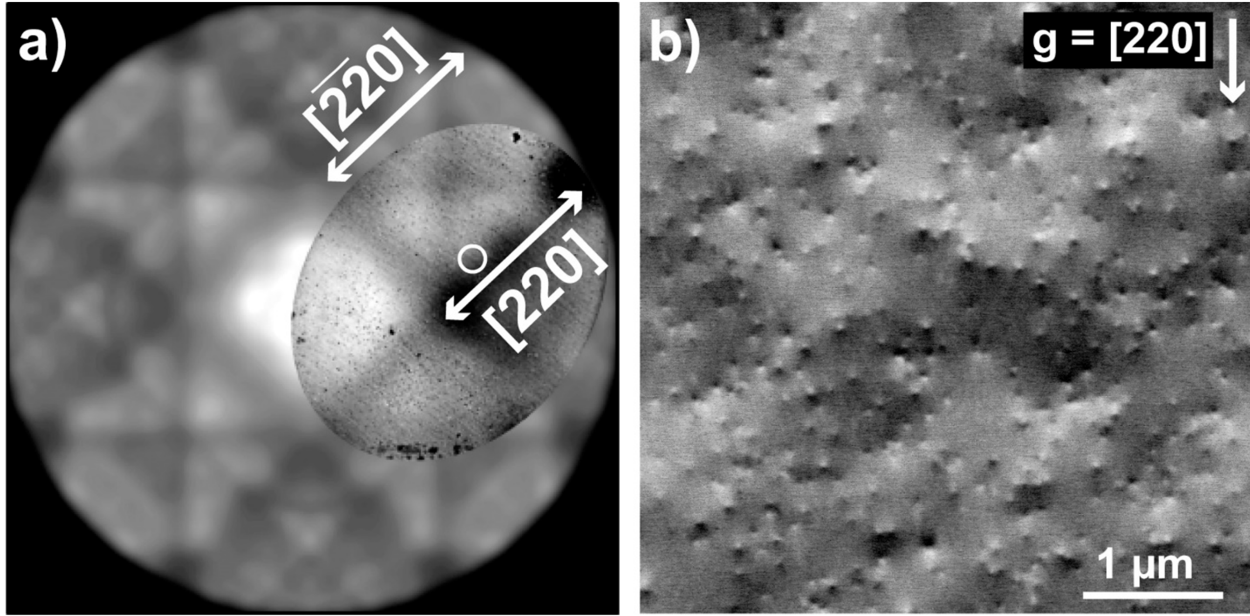

Figure 3.8. (a) Measured electron channeling pattern (ECP) collected at low-magnification (47×) from a Ge film prepared by ec-LPE on a n^+-Si(100) substrate overlaid on top of a simulated Ge ECP. (b) Electron channeling contrast image displaying a population of surface-penetrating threading dislocations (seen as bright/dark point features). Magnification: 25 000×, g = [220] diffraction condition.

provided in Figure 3.8b. From ECC imaging in Figure 3.8b, a homogeneous distribution of threading dislocations, with no obvious indications of large pile-ups, was observed. The single-defect resolution provided by ECCI, as opposed to the more common selective etch pit delineation approach, enabled an accurate determination of the threading dislocation density (TDD) of $1.7 \pm 0.2 \times 109$ cm^{-2}. Despite the very low growth temperature, the Ge films by ec-LPE possessed a TDD value comparable to, and even less than that achieved for as-grown films using more conventional methods at significantly higher temperatures.[23–25]

D. Discussion

Epitaxial Growth. The X-ray diffraction, electron diffraction, and cross-sectional and plan-view electron micrographs consistently and separately demonstrated that dissolved oxidized precursors at a liquid electrolyte/liquid interface can be electroreduced and the zerovalent product can be deterministically transported to a separate liquid metal/solid interface where crystal nucleation and growth can preferentially occur. The methodology reported here shows unambiguously that this process can occur over a macroscopic length scales and result in the formation of large area crystalline films. None of the ec-LPE trials produced materials with evidence of amorphous content, as is typical in conventional electrodeposition of Ge films at these temperatures.[26,27] Rather, the data cumulatively and strongly support the premise that the asprepared films from ec-LPE are not only crystalline throughout but also epitaxial with respect to the substrate. That is, the orientation of the support substrate at the bottom liquid metal/ solid support interface clearly affected the nuclei shape and the X-ray/electron diffraction properties of the films. The initial nucleation and crystallization of Ge occurred exclusively at the bottom interface between e-GaIn and Si. Accordingly, this work supports the contention that ec-LPE combines the strengths of electrodeposition and liquid phase epitaxy in one concerted process.

The synergy of electrochemistry and melt growth in ec-LPE method offers tangible advantages over either conventional electrodeposition or conventional liquid phase epitaxy. Conventional electrodeposition is not suitable for growing covalent inorganic crystalline semiconductor films under benchtop conditions for two inalienable reasons. First, the adatom surface diffusion on a growing crystallite is slow since the atom bond energy (Ge−Ge bonds are 178 kJ mol^{-1})[28] is much greater than the thermal energy. Second, zerovalent Ge atoms cannot be solvated by a molecular solvent, eliminating the possibility of a dynamic equilibrium between

solutes on the crystal growth plane and in solution. ec-LPE circumvents the latter issue by using the liquid metal rather than the liquid electrolyte as the growth medium. Separately, ec-LPE offers a high degree of control, in strong contrast with conventional liquid phase epitaxy. As evident in this work, the applied electrochemical potential/current can be started, maintained, stopped, and measured easily with a high degree of accuracy and precision. This is a fundamental tenet of all electrochemical methods. Conversely, the inability to initiate, to regulate, and to halt film growth with precision was the Achilles heel for conventional liquid phase epitaxy in semiconductor device manufacturing[13] rather than material quality.[13]

Requirements for ec-LPE. None of the ec-LPE experiments shown here required ancillary vacuum equipment, the application of high temperature, or exposure to regulated gaseous ambients. Rather, these experiments show that the concept of epitaxial film growth of covalent Group IV semiconductors can be performed entirely on a table top, in air using an aqueous precursor solution at temperatures below the boiling point of water.

Although temperature undoubtedly plays a strong role in determining the stages of nucleation and crystal growth,[13,29,30] the results show unambiguously that thermal gradients are not the governing factor in the ec-LPE process. This aspect strongly delineates ec-LPE from traditional liquid phase epitaxy, where supersaturation concentrations are attained through adjustment of the liquid metal temperature.[13,31] Instead, in ec-LPE, the film growth occurs isothermally and an applied electrochemical gradient drives and sustains crystal growth. The origin of the driving force for film growth (thermal vs electrochemical) is important for two reasons. First, attaining the necessary supersaturation conditions to force crystal formation solely by thermal gradients necessarily requires apparatus to regulate, stabilize, and know temperature. These requirements are difficult to do with a high degree of precision without a complex system design.[30,32] By contrast, electrochemical potential gradients are readily achieved with simple electronics. Although a computer controlled potentiostat was used in this work, in the simplest embodiment, one only needs a series combination of a battery and a load resistance to demand a precise current flow between electrodes in an ec-LPE reactor. Since the passage of current necessarily reports on the molar flux of solute produced by electroreduction at the liquid electrolyte/liquid metal interface and the diffusion of solute across a thin film is predictable, the concentration gradients prior to nucleation inside a flat, thin film of liquid metal are entirely knowable. Additionally, as shown

directly in this work, other simple chemical factors such as the concentration of dissolved GeO_2 in water can be used to affect the molar flux of Ge^0 into e-GaIn and therefore tune the rate of epitaxial film growth.

Even though the ec-LPE reactor design does not require excess ancillary equipment, it does hinge on the inclusion of a porous membrane that is selectively permeable to electrolyte but not the liquid metal. Compression by the porous membrane is crucial to maintain the thinness and flatness of the liquid metal throughout the ec-LPE process to avoid distortion by electrocapillarity.[33] At the potentials necessary for electroreduction of dissolved GeO_2, an uncapped thin film of e-GaIn breaks apart into discrete droplets. However, when constrained by a porous membrane and kept under a slight positive pressure, using a barrel apparatus (Figure 3.9), the thin liquid metal film remains continuous (Figure 3.10), enabling large area film deposition. Although the work shown here comprises films with areas ~4.8 cm^2, reconfiguring the cell to accommodate larger areas is possible.

The ec-LPE process is fully compatible with aqueous electrolytes. The presence of water is typically anathema in strategies for growing covalent inorganic crystals. Even for conventional electrodeposition, aqueous electrolytes are strongly not preferred for Group IV semiconductor materials.[34] But aqueous solutions of dissolved oxides are intrinsically much safer to handle than toxic gaseous precursors (e.g., $GeCl_4$, Ge hydrides)[9] in strongly reducing environments. For perspective, conventional liquid phase epitaxy requires H_2(g) ambients at high temperatures (>800 °C to remove oxide) to produce and maintain an oxide-free liquid metal, otherwise the crystal nucleation and growth are strongly inhibited.[35,13] However, at negative applied potentials, liquid metals like e-GaIn have clean interfaces since their oxides are fully reduced.[36] In fact, the electrochemical removal of native oxides on e-GaIn is easier in protic solvents since proton-coupled electron transfers facilitate oxide dissolution.[15] Thus, the electrochemical aspect of ec-LPE not only eliminates the need for gaseous reactants but it also offers a very straightforward and simple means to keep the liquid metal surface clean at all times.

Materials Quality in ec-LPE. The contact between Si and Ge is atomically abrupt and without strain. The lack of interdiffusion of either Ge or Si is expected since the diffusion coefficients for each element in the other material is immeasurably small[37,38] at the low temperatures employed here for ec-LPE. However, the lack of compressive strain, as noted in the peak position for the

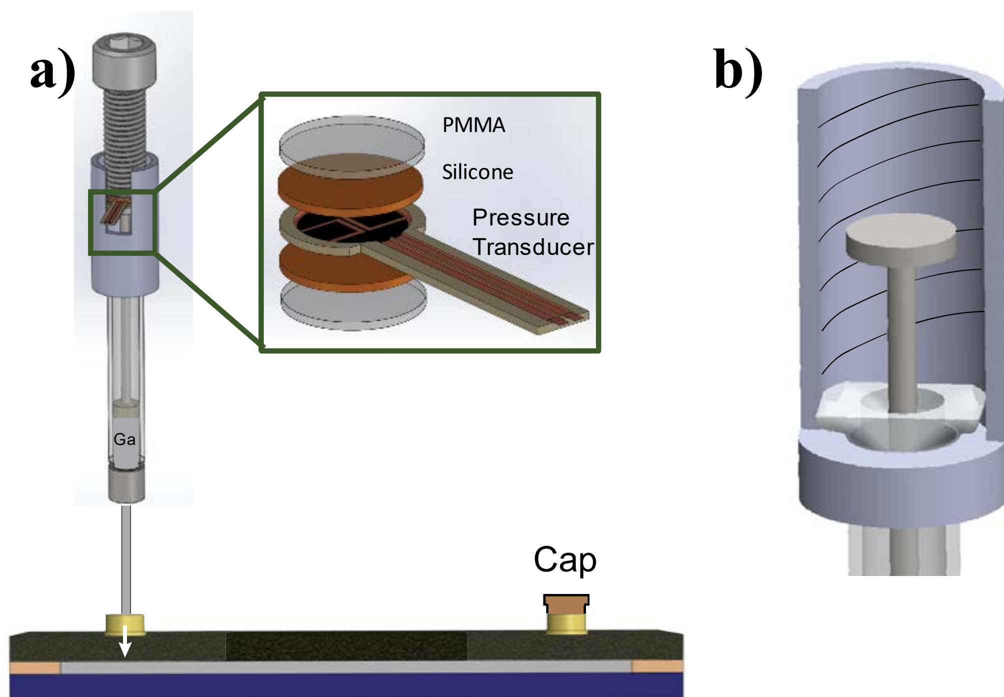

Figure 3.9. Syringe barrel used to apply a slight positive pressure to the liquid metal film. (a) Schematic shown with out ec-LPE cell and (b) schematic of the syringe barrel. A pressure transducer inserted between the bolt and syrringe plunger (a) was used to keep consistency between trials.

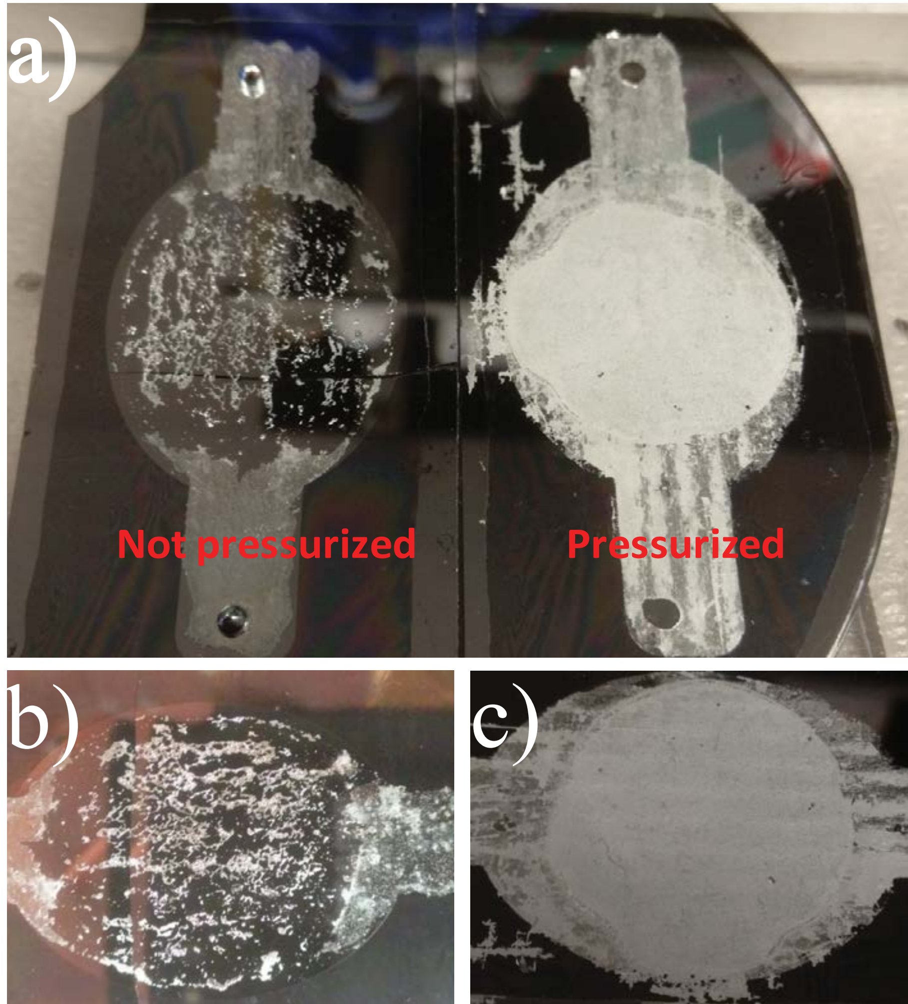

Figure 3.10. Optical photographs of frozen liquid metal films after control experiments were performed in the ec-LPE cell both without (b) and with (c) a positive pressure applied.

epifilm in the X-ray triple-axis scan, is unexpected. Typically, low temperature vapor phase deposition of Ge films on Si results in highly defective Ge/Si surfaces with large amounts of compressive strain.[20,39] Repetitive heating/cooling cycles can ameliorate that somewhat, but invariably leads to an increase in tensile strain from the different thermal expansion coefficients for Ge and Si.[8,20,40] The dark field TEM and ECCI images further confirm that, although these Ge films have a measurable level of threading dislocation defects, ec-LPE does not unavoidably introduce additional dislocation defects (as is the case with sputtering) into the film as it forms.[6] Whether this aspect, in conjunction with selective growth over smaller areas, can be leveraged to yield thick Ge films with low dislocation defects remains to be seen. Nevertheless, this aspect suggests that the normal annealing/cooling steps employed to form strain-relaxed $Si_{1-x}Ge_x$ layers[8,41] for Ge epilayers on Si may not be necessary with ec-LPE, improving the prospects for subsequent temperature sensitive device fabrication like CMOS-back processing.[8]

Based on the totality of the crystallographic analyses, the as-prepared Ge films are entirely suitable as growth platforms for subsequent materials deposition. For example, the as-prepared Ge films are of sufficient quality that they might be used as buffer substrates to deposit III−V films that otherwise have significant lattice mismatch with Si[42,43] for majority carrier devices, e.g., high performance channel materials in transistors.[44] For minority carrier devices, the purity of the Ge films, with respect to the incorporation of Ga, needs to be improved. That is, although impurities from molecular species in the electrolyte are not a concern since they cannot partition into the liquid metal, the EDS data clearly implicated high levels of Ga. At a Ga loading level of 100 at %, these Ge films had low resistivity. Although high conductivity necessarily limits minority carrier lifetimes, the inclusion of Ga in Ge is neither surprising nor unique to ec-LPE. The tendency of Ga to get trapped in growing crystals is well document in the semiconductor growth literature.[13,45−47] Although separate annealing/etching steps can purify these as-prepared Ge films, we strongly feel that a necessary improvement in the general ec-LPE concept would be to identify other low-melting-point metals that do not readily incorporate. Specific liquid metal alloys may exist that satisfy the electrochemical and metallurgical demands of ec-LPE of electronic-grade material, but their identities are not clear a priori. Nevertheless, this work strongly motivates their discovery.

E. Conclusion

This work reports the invention of ec-LPE as a new thin film strategy that directly yields high crystalline quality Ge epifilms on Si substrates without the need for high temperature, gaseous precursors, or high temperature/high vacuum equipment. Blending the best elements of liquid phase epitaxy and electrochemistry, the ec-LPE tactic is demonstratively unique and powerful in its simplicity and tunability. Although not stressed, the ec-LPE process is not limited to thin epilayer dimensions. Arbitrarily thick Ge films are possible if the ec-LPE process is continued for longer times and the lateral dimensions of the films are limited only by the patterning of the substrate. Further development along these lines could allow ec-LPE as a means to grow either crystalline Ge wafers at the 6″ scale or microscopic Ge epifilms with lowered dislocation defect densities. Additionally, although the principles described here were shown specifically in the context of Ge ec-LPE, they are applicable to any material that can be electrodeposited with a liquid metal that has the appropriate electrochemical and metallurgical properties. This work sets the stage for a Si ec-LPE process and motivates the identification and development of other liquid metal compositions.

F. References

(1) Pimputkar, S.; Speck, J. S.; DenBaars, S. P.; Nakamura, S. Nat. Photonics 2009, 3, 180−182.
(2) Ye, H.; Yu, J. Sci. Technol. Adv. Mater. 2014, 15, 024601.
(3) Nakamura, Y.; Murayama, A.; Ichikawa, M. Cryst. Growth Des., 2011, 11, 3301−3305.
(4) Lee, K. H.; Bao, S.; Wang, B.; Wang, C.; Yoon, S. F.; Michel, J.; Fitzgerald, E. A.; Tan, C. S. AIP Adv. 2016, 6, 025028.
(5) Pezzoli, F.; Isa, F.; Isella, G.; Falub, C. V.; Kreiliger, T.; Salvalaglio, M.; Bergamaschini, R.; Grilli, E.; Guzzi, M.; von Kanel, H.;¨Miglio, L. Phys. Rev. Appl. 2014, 1, 044005.
(6) Liu, J.; Kim, H. J.; Hul'ko, O.; Xie, Y. H.; Sahni, S.; Bandaru, P.; Yablonovitch, E. J. Appl. Phys. 2004, 96, 916−918.
(7) Xia, G.; Olubuyide, O. O.; Hoyt, J. L. Appl. Phys. Lett. 2016, 88, 013507.
(8) Xu, C.; Beeler, R. T.; Jiang, L.; Grzybowski, G.; Chizmeshya, A. V. G.; Menendez, J.; Kouvetakis, J. Semicond. Sci. Technol. 2013, 28, 105001.
(9) Shenai, D. V.; DiCarlo, R. L., Jr; Power, M. B.; Amamchyan, A.; Goyette, R. J.; Woelk, E. J. Cryst. Growth 2007, 298, 172−175.
(10) Fahrenkrug, E.; Maldonado, S. Acc. Chem. Res. 2015, 48, 1881−1890.
(11) DeMuth, J.; Ma, L.; Fahrenkrug, E.; Maldonado, S. Electrochim. Acta 2016, 197, 353−361.
(12) Carim, A. I.; Collins, S. M.; Foley, J. M.; Maldonado, S. J. Am. Chem. Soc. 2011, 133, 13292−13295.

(13) Capper, P.; Mauk, M. Liquid phase epitaxy of electronic, optical, and optoelectronic materials; Wiley: Chichester, England ; Hoboken, NJ, 2007.
(14) DeMuth, J.; Fahrenkrug, E.; Ma, L.; Shodiya, T.; Deitz, J. I.; Grassman, T. J.; Maldonado, S. *J. Am. Chem. Soc.* 2017.
(15) Zhao, J.; Yin, H.; Lim, T.; Xie, H.; Hsu, H.-Y.; Forouzan, F.; Bard, A. J. J. Electrochem. Soc. 2016, 163, D506−D514.
(16) Bard, A. J.; Parsons, R.; Jordan, J. Standard potentials in aqueous solution; M. Dekker: New York, 1985.
(17) Scharifker, B. R.; Mostany, J. J. Electroanal. Chem. Interfacial Electrochem. 1984, 177, 13−23.
(18) Guo, L.; Oskam, G.; Radisic, A.; Hoffmann, P. M.; Searson, P. C. J. Phys. D: Appl. Phys. 2011, 44, 443001.
(19) Wu, Y.; Yang, P. Chem. Mater. 2000, 12, 605−607.
(20) Birkholz, M.; Fewster, P. F.; Genzel, C. Thin film analysis by Xray scattering; Wiley-VCH: Weinheim, 2006.
(21) Hartmann, J. M.; Abbadie, A.; Papon, A. M.; Holliger, P.; Rolland, G.; Billon, T.; Fedé li, J. M.; Rouvie´ re, M.; Vivien, L.; Laval, S.` J. Appl. Phys. 2004, 95, 5905−5913.
(22) Denisov, S. A.; Matveev, S. A.; Chalkov, V. Y.; Shengurov, V. G. J. Phys.: Conf. Ser. 2016, 690, 012014.
(23) Carnevale, S. D.; Deitz, J. I.; Carlin, J. A.; Picard, Y. N.; McComb, D. W.; De Graef, M.; Ringel, S. A.; Grassman, T. J. IEEE J. Photovoltaics 2015, 5, 676−682.
(24) Luan, H.-C.; Lim, D. R.; Lee, K. K.; Chen, K. M.; Sandland, J. G.; Wada, K.; Kimerling, L. C. Appl. Phys. Lett. 1999, 75, 2909−2911.
(25) Kobayashi, S.; Nishi, Y.; Saraswat, K. C. Thin Solid Films 2010, 518, S136−S139.
(26) Yamamoto, Y.; Zaumseil, P.; Arguirov, T.; Kittler, M.; Tillack, B. Solid-State Electron. 2011, 60, 2−6.
(27) Huang, Q.; Bedell, S. W.; Saenger, K. L.; Copel, M.; Deligianni, H.; Romankiw, L. T. Electrochem. Solid-State Lett. 2007, 10, D124−D126.
(28) Elwell, D. J. Cryst. Growth 1981, 52, 741−752.
(29) Dean, J. A.; Lange, N. A. Pure Appl. Chem. 1973, 36, v.
(30) Kawasaki, T.; Tanaka, H. Proc. Natl. Acad. Sci. U. S. A. 2010, 107, 14036−14041.
(31) Myerson, A. S. Handbook of industrial crystallization; Butterworth-Heinemann: Boston, 2002.
(32) Small, M. B.; Barnes, J. F. J. Cryst. Growth 1969, 5, 9−12.
(33) Vonk, V.; Pontoni, D.; Cremers, M.; Kerkenaar, A.; Bode, A. A. C.; Szweryn, W.; Nowak, G.; de Jong, A. E. F.; Dosch, H.; Vlieg, E. Langmuir 2017, 33, 814−819.
(34) Bard, A. J.; Faulkner, L. R. Electrochemical methods: fundamentals and applications; Wiley: New York, 2001.
(35) Fulop, G. F.; Taylor, R. M. Annu. Rev. Mater. Sci. 1985, 15, 197− 210.
(36) Bergmann, R.; Kurianski, J. Mater. Lett. 1993, 17, 137−140.
(37) Pourbaix, M. Atlas of electrochemical equilibria in aqueous solutions; Pergamon Press: Oxford, NY, 1966.
(38) Ogino, M.; Oana, Y.; Watanabe, M. physica status solidi (a) 1982, 72, 535−541.
(39) Silvestri, H. H.; Bracht, H.; Hansen, J. L.; Larsen, A. N.; Haller, E. E. Semicond. Sci. Technol. 2006, 21, 758.

(40) Cannon, D. D.; Liu, J.; Ishikawa, Y.; Wada, K.; Danielson, D. T.; Jongthammanurak, S.; Michel, J.; Kimerling, L. C. Appl. Phys. Lett. 2004, 84, 906−908.
(41) Ishikawa, Y.; Wada, K.; Cannon, D. D.; Liu, J.; Luan, H.-C.; Kimerling, L. C. Appl. Phys. Lett. 2003, 82, 2044−2046.
(42) Bean, J. C.; Sheng, T. T.; Feldman, L. C.; Fiory, A. T.; Lynch, R. T. Appl. Phys. Lett. 1984, 44, 102−104.
(43) Lee, K.; Zimmerman, J. D.; Hughes, T. W.; Forrest, S. R. Adv. Funct. Mater. 2014, 24, 4284−4291.
(44) Ginige, R.; Corbett, B.; Modreanu, M.; Barrett, C.; Hilgarth, J.; Isella, G.; Chrastina, D.; Kanel, H. v.¨Semicond. Sci. Technol. 2006, 21, 775.
(45) Lee, M. L.; Fitzgerald, E. A.; Bulsara, M. T.; Currie, M. T.; Lochtefeld, A. J. Appl. Phys. 2005, 97, 011101.
(46) Schmidt, V.; Wittemann, J. V.; Gö sele, U. Chem. Rev. (Washington, DC, U. S.) 2010, 110, 361−388. (46) Jang, J.; Oh, J. Y.; Kim, S. K.; Choi, Y. J.; Yoon, S. Y.; Kim, C. O. Nature 1998, 395, 481−483.
(47) Yoon, S. Y.; Kim, K. H.; Kim, C. O.; Oh, J. Y.; Jang, J. J. Appl. Phys. 1997, 82, 5865−5867.

CHAPTER 4

Eutectic-Bismuth Indium as a Low Melting Point Liquid Metal for Electrochemical Liquid-Liquid-Solid Growth of Germanium Microwires and Coiled Nanowires

A. Introduction

Only four pure metallic elements are liquids at or near room temperature (mercury, francium, cesium, gallium)[1] and only mercury and gallium are stable in air and abundant enough for practical study. However, there are numerous metal *alloys* with low melting points.[2-6] The number and types of alloys that have solvation properties appropriate for semiconductor crystal growth is presently unclear due to a lack of relevant experimental data and predictive models. Identification of suitable liquid metal solvents would specifically expand the utility of ec-LLS and more generally add to the basic understanding of liquid metals as solvents for crystal growth.

Our group has previously identified mercury (Hg), gallium (Ga), indium (In), and a eutectic alloy of Ga & In (e-GaIn) as metals that can operate as electrodes and growth solvents in ec-LLS.[2,7-9] Metals without either Hg or Ga are particularly desirable since the former has high volatility[9] and the latter tends to incorporate strongly in group IV semiconductor crystals.[10] A potentially interesting alternative liquid metal is eutectic bismuth indium (21.3 at % Bi and 78.7 at. % In, e-BiIn).[11] This alloy melts at T = 72 ºC at ambient pressure[11] and has been used extensively as a solder base.[3] Figure 4.1 shows the calculated pseudo-binary phase diagram for mixtures of Ge and e-BiIn at standard pressure.[12] Both molten Bi and In are individually known solvents for liquid phase epitaxial (LPE) growth of group IV semiconductor films at elevated temperatures,[13-17] indicating that each component metal can solvate Ge. Further, the larger crystal radii of Bi (0.117 nm)[18,19] and In (0.094 nm),[18,19] relative to Ge (0.053 nm)[18,19] could impede their substitution into Ge lattice sites, limiting their potential as unintended dopants. Our past experience specifically with Ge ec-LLS using liquid metals consisting of Ga and In shows that the resultant crystals have low levels of In.[4]

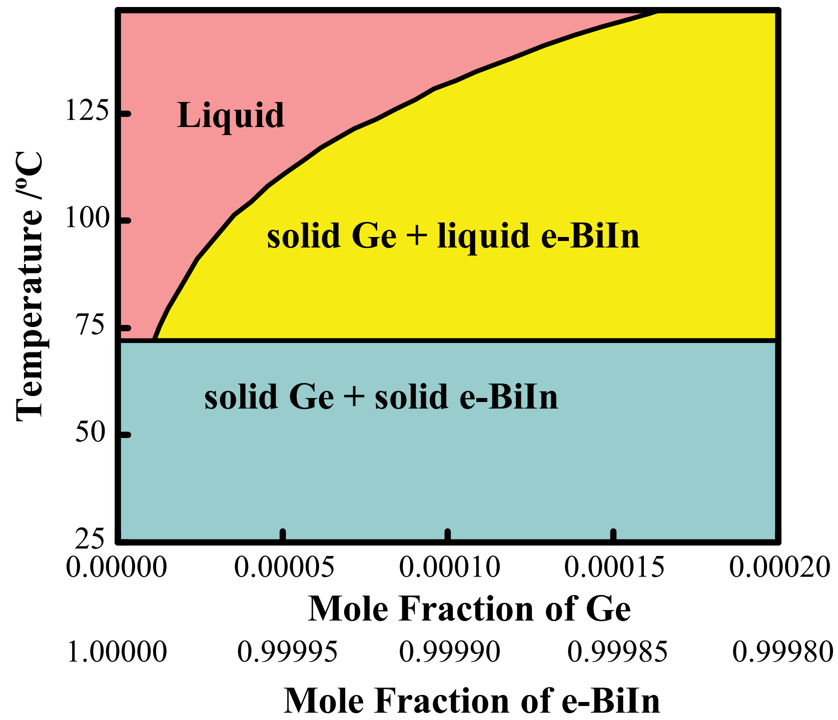

Figure 4.1. Pseudo-binary phase diagram of mixtures of Ge and e-BiIn at standard pressure. The relative fractions of Bi and In are constant as the amount of Ge is varied.

Accordingly, we show here the resultant materials produced through Ge ec-LLS using liquid e-BiIn. Nano- and microdroplets of e-BiIn were investigated over bulk pools so as to determine whether epitaxial crystal Ge nanowire and microwire growth was possible and since Ge nano- and microwires have desirable properties for a number of electronic and energy applications.[4,8,10,20] The intents of this work are to validate whether e-BiIn is a potential metal solvent for ec-LLS, to identify any characteristics that are beneficial/deleterious in the search for additional liquid metal solvents, to determine whether a non-Hg, non-Ga containing liquid metal results in a more pure resultant crystal, and to determine whether this liquid metal shows any unique crystal growth tendencies.

B. Methods

Materials Acetone (ACS grade, Fisher Scientific), indium (99.99% Gallium Source), germanium dioxide (99.998% Sigma-Aldrich), sodium borate (>99.5% Sigma-Aldrich), gallium (99.999%, Alfa Aesar), hydrofluoric acid (49%, Transene Inc.), methanol (ACS grade, Fisher Scientific), 2-propanol (ACS grade, Fisher Scientific), hexamethyldisilazane (HMDS, Fisher Scientific), SU-8-2007 (MicroChem Corp.), SU-8-2025 (MicroChem Corp.), SU-8 developer (MicroChem Corp.), Microposit S1813 photoresist (Shipley), Microposit MF-319 photoresist developer (Shipley), oxygen gas (Metro Welding, Detroit, MI), and Bi (99.999%, Kurt J. Lesker) were used as received. Degenerately doped n-type Si(100) wafers (0.625 ± 0.020 mm, $\rho < 0.007$ Ω·cm, Addison Engineering, Inc.) and n-type Si(111) wafers (0.525 mm, $\rho < 0.004$ Ω·cm SunEdison) were diced and used as substrates. Water with a resistivity >18.2 MΩ·cm (Nanopure Barnstead Water Purification) was used throughout.

Preparation of e-BiIn Two routes were employed to produce e-BiIn droplets (Figure 4.2 and 4.3). In the first method (Figure 4.2a and 4.3), photoresist films were photolithographically patterned with arrays of microwells with r = 350 nm and a pitch of 2 μm on 4" Si(100) wafers. A 700nm thick SiO_2 layer was grown using plasma enhanced chemical vapor deposition (PECVD) (Ultradep 2000, GSI Lumonics) (Figure 4.3). Prior to use, the substrates were cleaned with isopropanol, baked at T = 200ºC under vacuum (10^{-3} torr), and then vapor primed with HDMS. Then photoresist S1813 (Shipley) was immediately spin coated to a film thickness of 1.45 μm. The films were then heated for 90s at T = 120°C. Projection photolithography (GCA Autostep 200, RZ Enterprises, Inc.) with a 5x reduction optic system (21mm lens with 0.45μm numerical aperture)

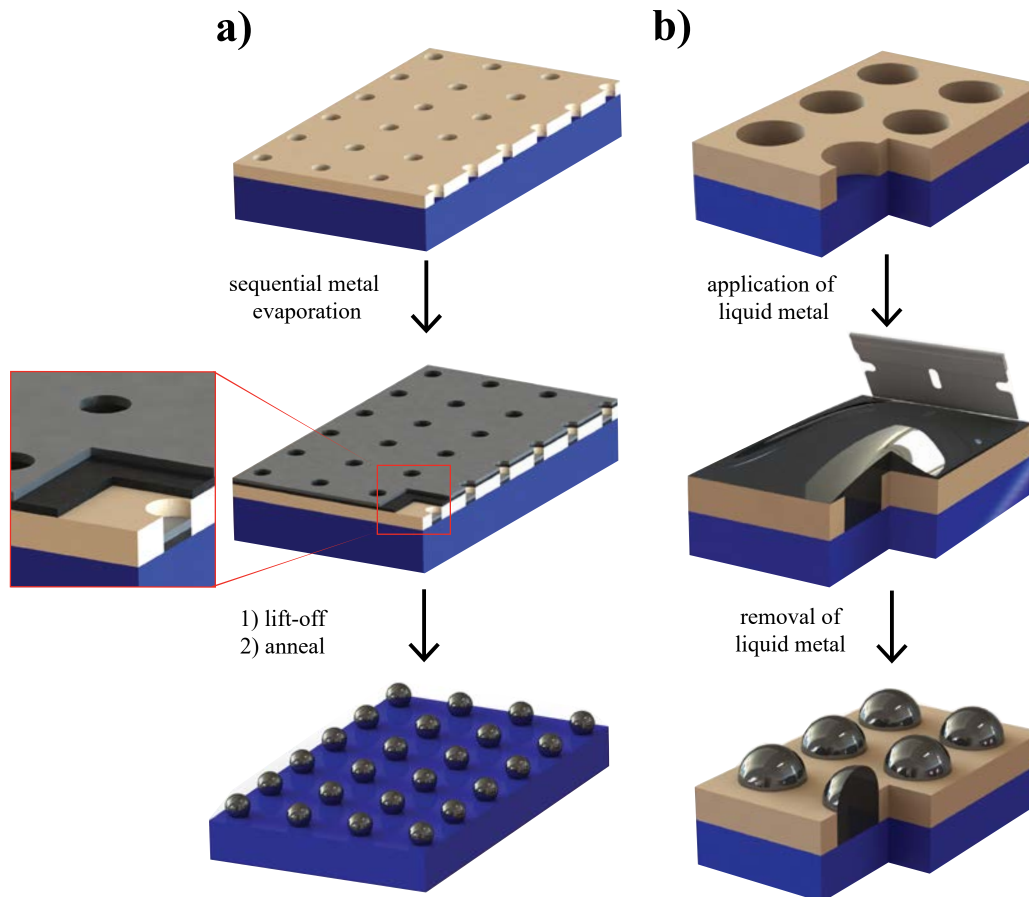

Figure 4.2. Schematic of the two methods used to produce e-BiIn droplets by (a) sequential evaporation of Bi and In and (b) spreading of the liquid eutectic. a) Arrays of nanowells were photolithographically patterned on a Si substrate followed by sequential evaporation of first Bi then In. Subsequently, the bilayers were annealed at T = 120 °C to form droplets of e-BiIn. b) Liquid e-BiIn was applied and spread over a substrate with microwells patterned in photoresist prepared by photolithography. Excess liquid metal was removed, leaving arrays of microwells filled with e-BiIn.

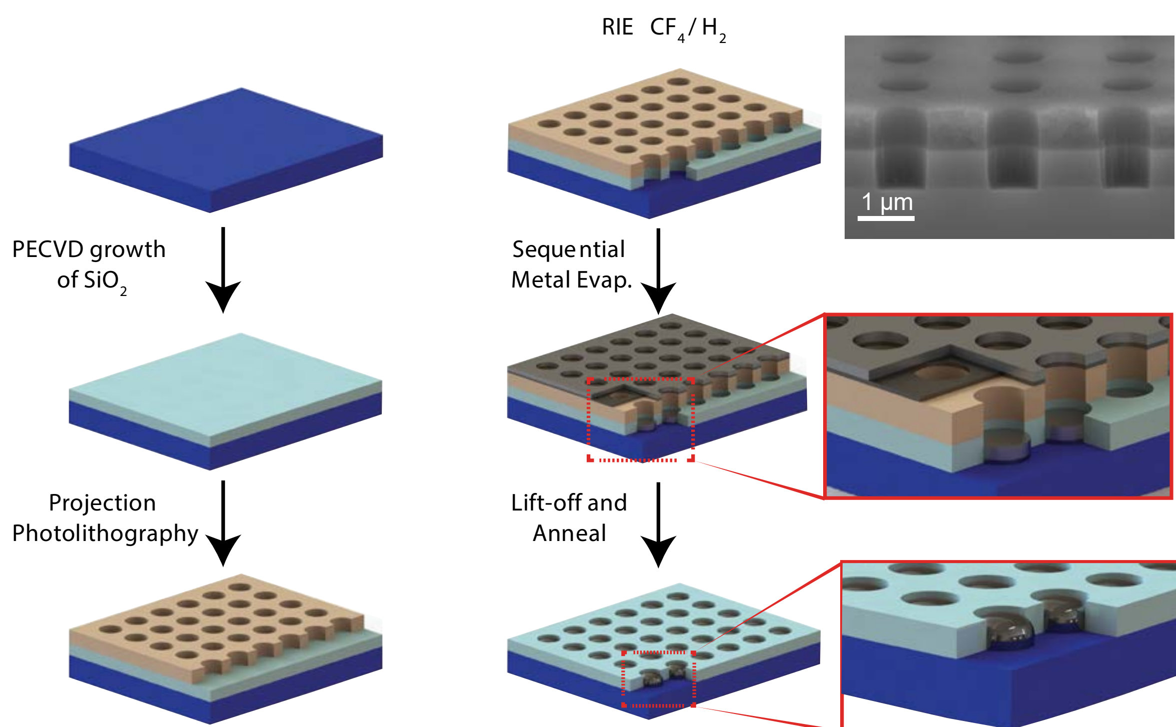

Figure 4.3. Schematic for producing e-BiIn nanodroplets in hole arrays patterned into SiO_2. Steps are same as in Figure 4.2a except an 700 nm SiO_2 is first deposited on the substrate using plasma enhanced chemical vapor deposition (PECVD) and the lithographic pattern is transferred to the SiO_2 layer using reactive ion etching (RIE).

was used to expose (~ 0.029 J at λ = 365nm) the coated substrate through a custom photolithography mask (Photon Science). Samples were then reactive ion etched (APS Dielectric Etch Tool, STS) with $CF_4(g)$ to selectively remove the oxide. Sequential thermal evaporation of Bi followed by In was performed on a custom-built metal evaporator. Afterwards, the substrate was sonicated in acetone to lift-off the metal coated photoresist leaving only arrays of droplets patterned on the Si substrate. The Si substrate was then heated at 200ºC for 20 min to melt the films into a droplet with a homogeneous composition. To ensure the droplets were homogeneous in composition large E-BiIn droplets were fabricated and a cross-sectional EDS map was taken (Figure 4.4).

In the second route (Figure 4.2b), stoichiometric amounts of metallic In and Bi were placed in an oven heated at T = 175 °C overnight. Following, the liquid alloy was mechanically mixed and stored at T = 100 °C. Immediately prior to use, the eutectic alloy was stirred again and then transferred with a glass pipet onto a substrate. A lint free cloth was used to spread the molten metal across the whole substrate and to manually tap it into each microwell. Excess liquid metal was removed with a separate damp cloth. e-BiIn film electrodes for voltammetric measurements were prepared similarly by pipetting a small droplet of the liquid metal onto a bare, freshly etched Si substrate and spreading with a lint free cloth.

Electrochemical methods Computer controlled potentiostats (CHI420A and CHI760C, CH Instruments) were used throughout. All ec-LLS experiments were performed in a three-electrode cell in lab ambient and heated to a specified temperature with an aluminum heating block. A thermocouple mounted on the underside of the Si wafer section was used to measure the temperature of the electrode. A custom-built, compression Teflon cell featuring a Viton O-ring defined the area of the working electrodes. Ohmic contact to all Si substrates was made with e-GaIn. A platinum mesh and a silver wire coated with silver chloride immersed in 4 M KCl were employed as the counter and reference electrodes, respectively. All potentials are referenced to E(Ag/AgCl).

Materials characterization Scanning electron micrographs were obtained with either a FEI Nova Nanolab Dualbeam Focused Ion Beam Workstation or a JEOL-7800FLV equipped with a Schottky field emitter filament using an Everhart-Thornly Detector (ETD) or a through–the-lens detector (TLD). Transmission electron micrographs and concomitant selected area electron

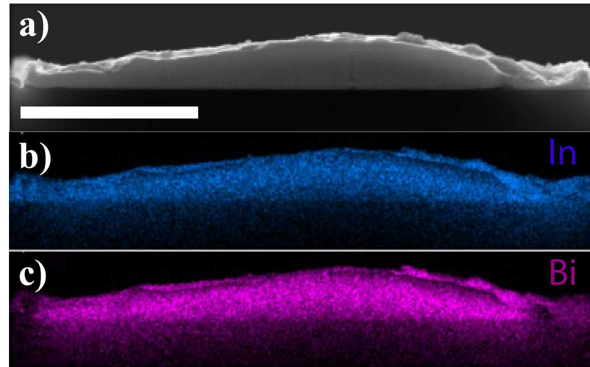

Figure 4.4. A cross sectional scanning electron micrograph (a) of a e-BiIn droplet formed by sequential evaporation followed by annealing at T = 120 °C. Corresponding EDS elemental maps of In (b) and Bi (c). Scale bar: 5 μm.

diffraction patterns were collected with a JEOL 3011 TEM using a LaB_6 filament functioning at 300 kV. Atom probe tomography (APT) data was collected using a Cameca LEAP 4000 XHR operating in laser pulsing mode. All samples for APT analysis were prepared using a FEI Helios 650 Nanolab Focused Ion Beam work station. A detailed description of the sample preparation and the data analysis for atom probe tomography is given in the Supporting Information (Figures S1 and S2, respectively).

Resistivity Measurements Ge nanowires were sonicated in 50 μL of methanol and then drop-cast onto a Si substrate coated with a 2 μm thick SiO_2 layer and pre-patterned with metal contact pads (10 nm of Ni-Cr and 190 nm Au). Pt leads connecting the individual nanowires to the metal pads were deposited by ion beam assisted chemical vapor deposition (FEI Helios Nanolab Dualbeam Focused Ion Beam Workstation). Current-potential responses were measured with a Keithley 4200 semiconductor parameter analyzer.

C. Results

Voltammetry Voltammetric measurements were first recorded with thin films of e-BiIn in 0.01M $Na_2B_4O_7$ at $T = 49 \pm 2$ ºC, i.e. below the melting point of the alloy (Figure 4.5), deliberately to identify if any surface-specific changes (oxidation, stripping, ...etc). As a solid, the complications of electrocapillarity or fast mixing between the surface and the bulk are obviated. In the absence of dissolved GeO_2, the first voltammetric scan exhibited two waves on the cathodic sweep at E = -1.05 and -1.5 V before the onset of proton reduction, consistent with the reduction of surface oxides. On the anodic sweep, a small, broad peak at E = -1.0 V and a sharper anodic peak at E = -0.85 V were observed for the re-oxidation of the surface. During the next cathodic sweep, the signal at E = -1.05 V was greatly diminished and the wave at -1.5 V was absent, implying some chemical/compositional change had occurred. On the anodic sweep, the oxidative wave at E = -1.0 V was more pronounced and the anodic peak at E = -0.85 V was diminished, again indicating the electrode surface was different. Upon addition of dissolved GeO_2, the voltammetric response changed again. On the cathodic sweep, no pronounced waves were suggestive of the reductive elimination of surface oxides was observed. Additionally, the overall current increased relative to the current measured in the blank electrolyte at potentials more negative than -1.2 V, consistent with the electroreduction of dissolved GeO_2 (eq 1) occurring in parallel with some generation of H_2(g).

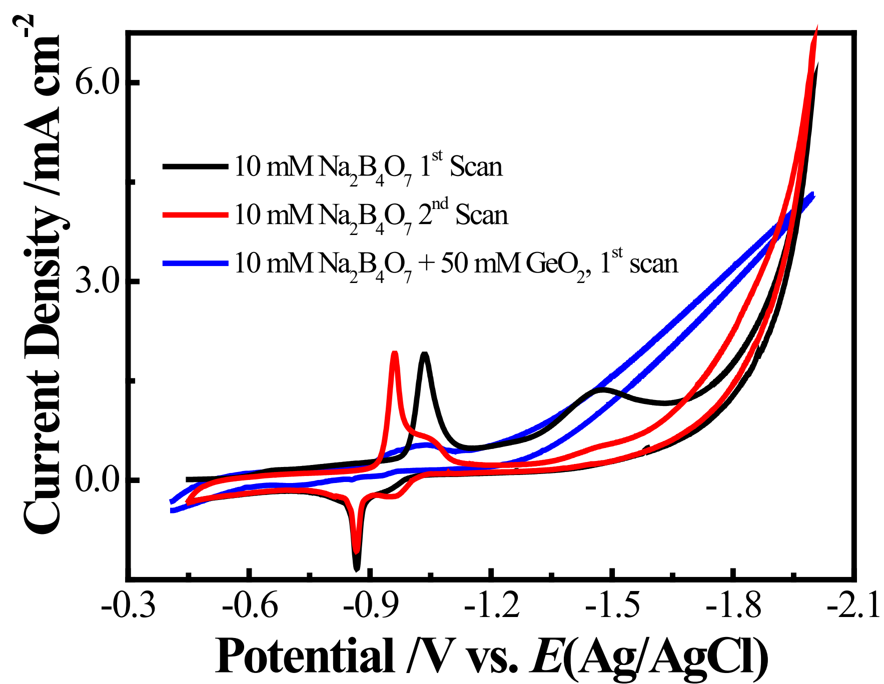

Figure 4.5. Voltammetric responses for a e-BiIn film electrode immersed in 0.01 M $Na_2B_4O_7$(*aq*) without and with 0.05 M dissolved GeO_2 at T = 50 °C. Scan rate= 0.05 V s^{-1}.

$$HGeO_3^- + 4e^- + 2H_2O \rightarrow Ge + 5OH^- \quad (13)$$

Ge ec-LLS Ge ec-LLS was performed both at T = 50 and 95 °C, i.e. above and below the melting point of e-BiIn, with a single, constant applied potential sufficient to drive reduction of dissolved GeO_2. All experiments performed at the lower temperature yielded no evidence of Ge micro/nanowire formation. Instead, scanning electron micrographs showed the e-BiIn droplets were coated with an irregular, rough deposit that readily charged under exposure to the electron beam, implying poor conductivity of the coating (Figure 4.6a). The coating included some sporadic thin nanowires but the e-BiIn droplets were not displaced upwards from the substrate to indicate any heterogeneous nucleation and growth occurred at the e-BiIn/Si interface. Additional control experiments where e-BiIn microdroplets were submerged in electrolyte at T = 95 °C containing dissolved GeO_2 but without an external applied bias showed no evidence of Ge deposition. Figure 4.6b shows the corresponding chronoamperometric responses recorded during ec-LLS with E = -1.6 V at T = 95 °C. In general, the data showed numerous current spikes that occurred randomly in time. There was no consistent current-time profile observed between experimental repetitions. Figure 4.6c shows the materials produced with e-BiIn microdroplets under the same experimental conditions. Ge microwires were apparent with metal droplets consistently located at the tip of the microwires, similar to what was observed previously in ec-LLS with Ga,[7] e-GaIn[2] and Cu-In-Ga,[4] but in contrast to earlier results with pure In nanoparticles.[8] However, the Ge microwires were coated with precipitates that also were found around the base of the microwires. Elemental analyses indicated these precipitates were composed nominally of Ge, Bi, and In (Figure 4.7). Additionally, in these experiments, each original e-BiIn droplet was partitioned into a smaller droplet with multiple smaller nanodroplets. Each of these 'satellite' droplets seeded the growth of thinner Ge nanowires.

To determine whether In and/or Bi were incorporated into the as-prepared Ge, atom probe tomography (APT) was performed on sections of Ge microwires (Figure 4.8 and 4.9). Figure 4.8a shows the APT elemental map of the Ge wire where each dot corresponds to an atom of Ga, In or Bi. Figure 4.9a shows the shape of a representative conical section that was removed from an as-prepared Ge microwire and analyzed by APT. In these sections, the top corresponds to the outer surface of the Ge microwire and the bottom represents a region 500 nm inward along the radial vector.

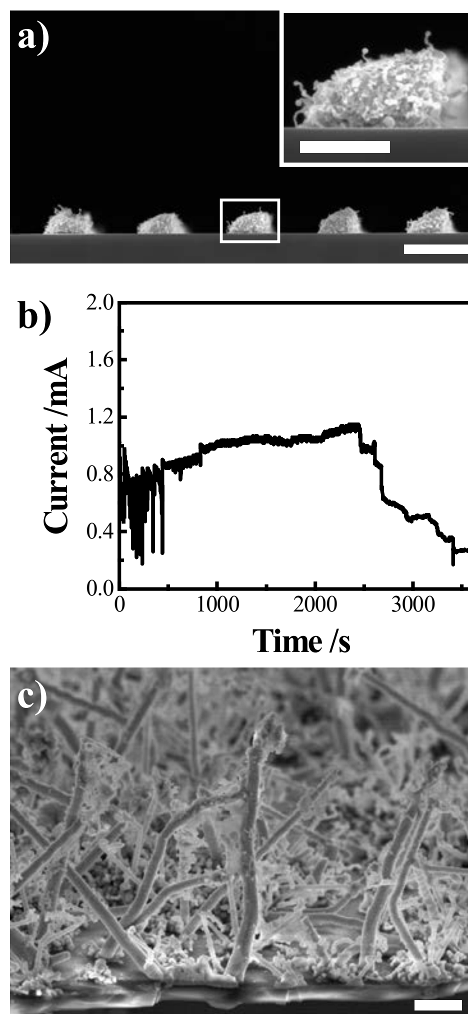

Figure 4.6. a) Cross sectional scanning electron micrograph of E-BiIn droplets on a Si(100) substrate after applying a bias of E_{appl}= -1.2V for 1 hr at T=50 ºC. b) Chronoamperometry response for Ge ec-LLS experiments on e-BiIn microdroplets in electrolyte containing 50 mM GeO_2 and 10 mM $Na_2B_4O_7$ at T=95ºC and E_{appl}=-1.6V. c) Tilted SEM image of Ge microwires obtained under the conditions from b). Scale bar: a) 2.5 µm inset 500nm, c) 10 µm.

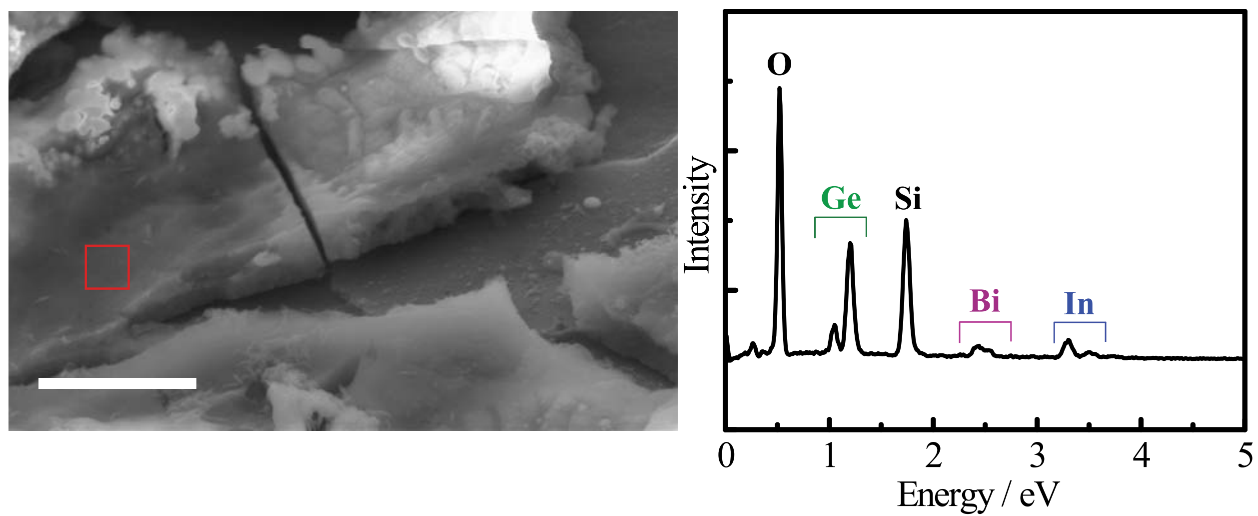

Figure 4.7. Scanning electron micrograph (left) of the precipitate that forms during ec-LLS experiments at E_{appl} = -1.6 V. EDS spectrum (right) from a selected region on the precipitate (shown in red on micrograph). Scale bar is 2.5 µm.

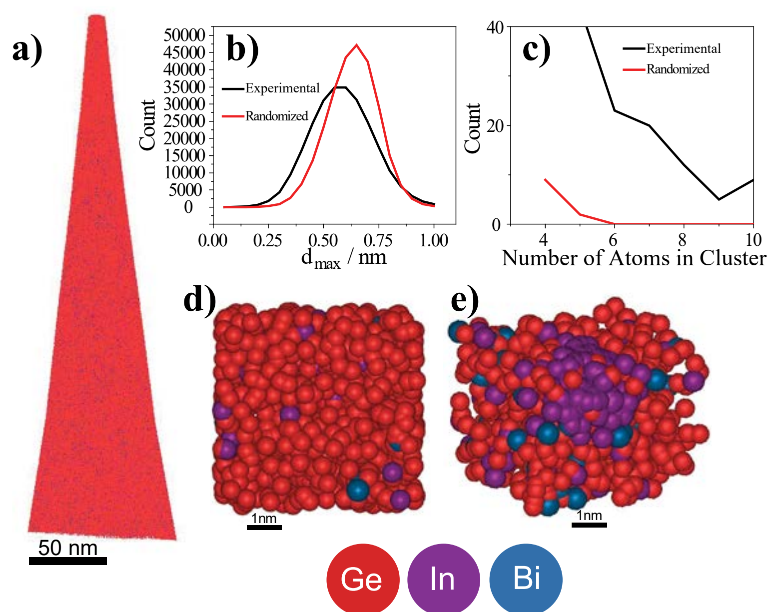

Figure 4.8. Atom probe tomography and cluster analysis of Ge wires grown from e-BiIn electrodes. (a) 3D elemental map, (b) Cluster counts as a function of d_{max} between solute atoms for the randomized and experimental data. (c) Cluster counts as a function of the number of atoms in a cluster for the randomized and experimental data for a d_{max} of 0.265 nm order. From the 3D elemental map a domain without clustering (d) and with clustering (e) were reconstructed.

Cluster analysis was performed with the Integrated Visualization and Analysis Software (IVAS) where each individual solute atom (Bi or In) is evaluated as being part of a potential cluster. The data procedure followed an algorithm previously described elsewhere[21] Briefly, to ensure that the identified clusters were not due to random composition fluctuations, a rigorous statistical test was performed using the experimentally obtained APT data and a model data set with randomly distributed atoms. Figure 4.8b shows the number of clusters that can be identified as a function of $d_{\max}$, the cluster diameter, for the randomized and experimental data. Any two solute atoms that are within a spacing equal to or less than $d_{\max}$ were considered to be within the same cluster. Two additional constraint parameters were used describing the minimum number of metal atoms in a cluster and minimum number of total atoms parameters. In Figure 4.8b, to be counted, a cluster must contain at least 3 solute atoms within a spacing of d_{max}. In addition, the minimum number of total atoms that constituted a cluster was initially set at 3. Under these constraints, as shown in Figure 4.8b, the randomized data curve approached a cluster count of 0 at d_{max} = 0.265 nm, implying that this d_{max} value was a sufficient threshold to not mistake a random fluctuation of solute distribution as an actual cluster. Figure 4.8c shows the number of clusters as a function of the number of atoms in a cluster for the randomized and experimental data. As shown, analysis of the randomized datasets showed the maximum number of atoms in a hypothetical cluster was 6 atoms (i.e. x-intercept). Therefore, the experimental APT data was analyzed assuming that clusters identified with more than 6 atoms were not from random variation and instead represented *true* clusters. Figure 4.8d and e show reconstructed domains from the 3D elemental map (Figure 4.8a). In Figure 4.8d the there was no identified cluster using this algorithm whereas Figure 4.8e shows a domain where a cluster was identified.

Figure 4.9b shows a grey-scale cluster map across the same sample, where the dark regions corresponded to regions where the local concentration of metal (Bi or In) atoms was high. As apparent in Figure 4.9b, the metal atom distribution in the Ge crystal was not uniform and featured distinct regions suggestive of metal clusters/occlusions. The size of the occlusions spanned a narrow distribution, with a mean and mode cluster size of 24 and 9 atoms, respectively (Figure 4.9c). The average composition of each occlusion (grouped by size) is shown in Figure 4.9d. As indicated, the metal occlusions were not uniformly composed of just one element, but were In-rich. Figure 4.9e presents the average atomic fractions (%) of In, Bi and Ge in the sample as a function of radial position, where the outer microwire surface corresponds to x = 0. The

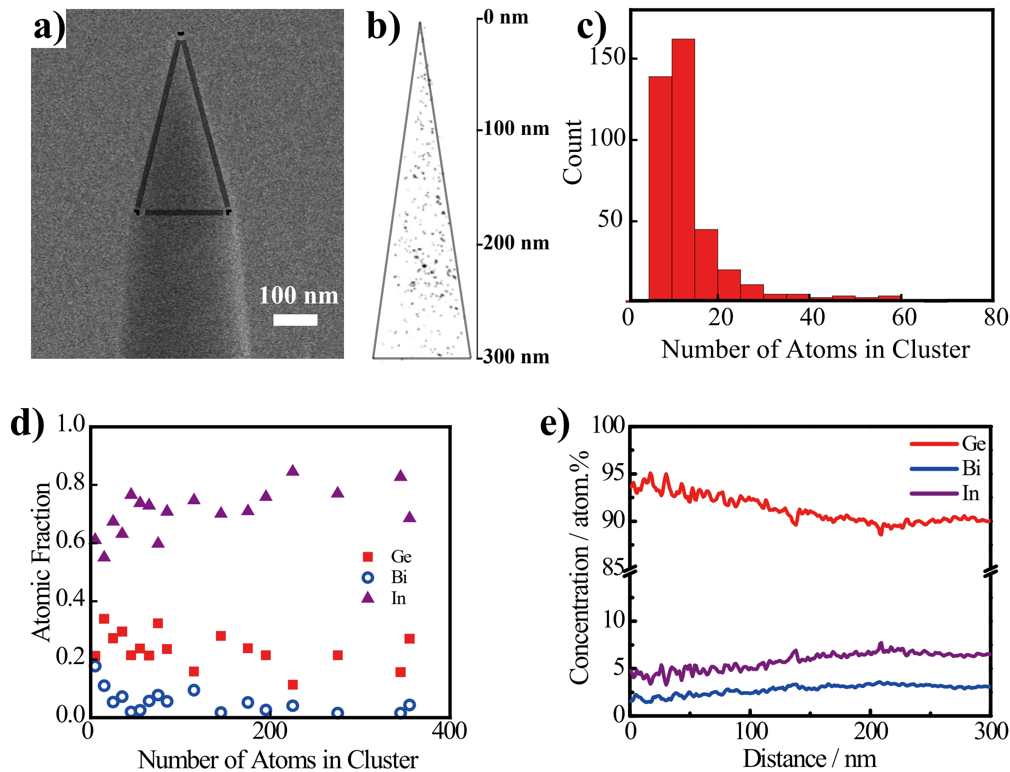

Figure 4.9. (a) Scanning electron micrograph of the APT sample taken from a segment of a Ge microwire mounted on a Si micro-post and shaped to a fine point for APT analysis. b) Map of the Ge APT sample from a) where the greyscale intensity corresponds to occlusions of solvent atoms identified from cluster analysis. c) Histogram (bin size 5 atoms) showing the size distribution (number of clusters vs size of cluster) for a majority of the identified occlusions. The full range of the cluster sizes was not shown for clarity. d) average composition of the occlusions as a function of cluster size. Atomic fractions were obtained by averaging the composition of clusters contained within a set size range (i.e. bin size 10 atoms). e) the bulk elemental concentrations of Ge, Bi and In as a function of depth into the interior of the Ge microwire. The point 0 on the *x-axis* corresponds to the tip of the APT sample as well as the surface of the Ge microwire and a distance > 0 corresponds to the radial position inward.

concentration of the metal atoms was lower closer to the surface of the microwire as compared to the interior. The ratio of In to Bi was nominally constant at 2:1, less than the nominal 3:1 ratio of the eutectic composition. The overall level of metal impurities was similar to previous Ge ec-LLS observations with a Cu-In-Ga liquid metal,[4] with the most prominent difference being that In was incorporated at a much higher concentration here than with the Cu-In-Ga alloy.

Additional ec-LLS experiments were performed at T = 95 °C but with E = -1.2 V. Figure 4.10a displays a representative chronoamperometric response for Ge nanowire ec-LLS recorded with E = -1.2 V and T = 95°C. The current transient exhibited an initial decrease; but, after 15 s the current decay slowed. After 200 s, the current increased and then reached a local maximum at 750 s before decreasing again. This general shape was similar to the current transients observed previously.[2] These experiments also produced Ge micro/nanowires but with two important differences. First, a single microwire emanated from each microwell, implying the original e-BiIn droplet did not fragment. Second, there were no observable precipitates on/around the microwires. Figure 4.10b shows representative scanning electron micrographs of experiments performed in 50 mM GeO_2(aq) with a Si electrode coated with molten e-BiIn nanodroplets at T = 95 °C and at E = -1.2 V for 30 min. The diameters of the resultant nanowires were consistently smaller than the original nanodroplets. Separately, the orientation of the nanowires relative to the surface plane was not consistent and did not necessarily follow the <111> direction. Some growth conditions did imply a net orientation suggestive of epitaxy (Figure 4.11), but the cumulative experiments indicating epitaxial growth were not readily or routinely attained. Additionally, an unexpected Ge nanowire morphology was observed. A large fraction of the Ge nanowires featured at least one segment where the nanowire was coiled with a discernible pitch (Figure 4.10d). The coiled segment often occurred after a kink that changed the principal growth direction of the nanowire.

Figure 4.12 shows a representative high resolution transmission electron micrograph of a straight segment of a Ge nanowire produced at T = 95 °C and at E = -1.2 V for 30 min. Figure 4.12 a shows the liquid metal droplet capped the tip of the nanowire, overhanging the flat top and contacting the side of the nanowire. The crystallinity of the Ge nanowire was verified by the lattice fringes viewed throughout the nanowire section (Figure 4.12b). The selected area electron diffraction pattern (Figure 7b inset) further matched a single crystal of Ge viewed along the <110> direction. This pattern was consistently measured across different regions of the nanowire,

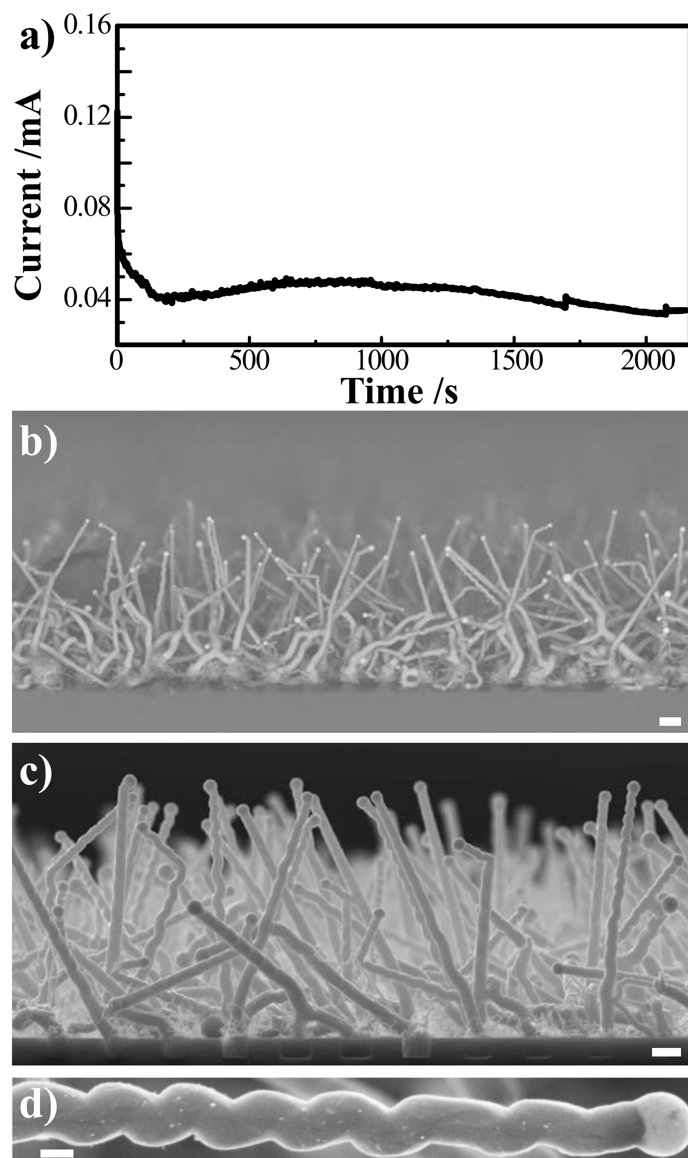

Figure 4.10. a) Chronoamperometric response of Ge ec-LLS performed in electrolyte containing 50 mM of GeO_2 50mM and 10 mM $Na_2B_4O_7$ at E = -1.2V V and T = 95 °C with e-BiIn nanodroplets on a n^+-Si(100) substrate. b) Scanning electron micrographs of Ge nanowires prepared by ec-LLS as in (a) at b) low and c) higher magnification cross-sectional view of a Ge nanowire film. d) High magnification of individual Ge nanowire highlighting a coiled section. Scale bars: b) 1 µm, c) 1 µm, and d) 250 nm respectively.

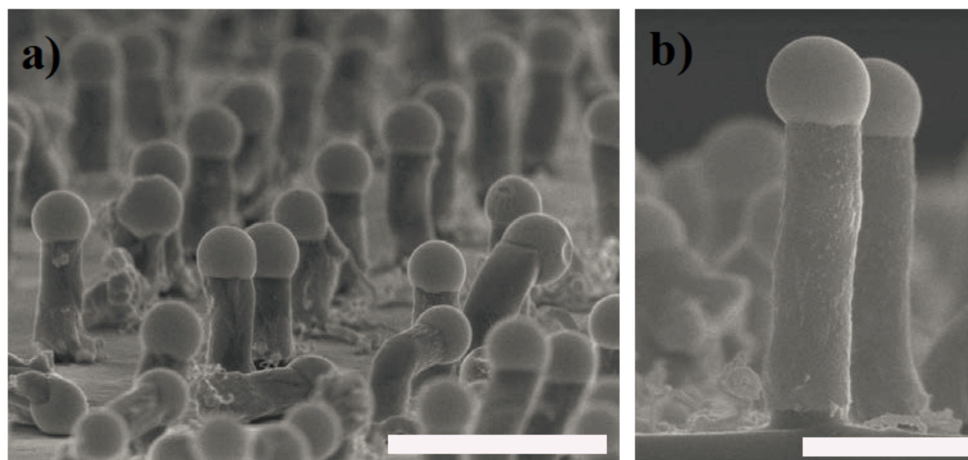

Figure 4.11. (a) Tilted scanning electron micrograph of Ge nanowires prepared by ec-LLS at *E* = -1.2 V and *T* = 90 °C following a pre-electrolysis step. (b) Cross-sectional scanning electron micrograph of nanowires in (a) indicate the propensity of the nanowires to follow the [111] growth direction of the underlying Si (111) substrate. Scale bar is (a) 2 μm (b) 1 μm.

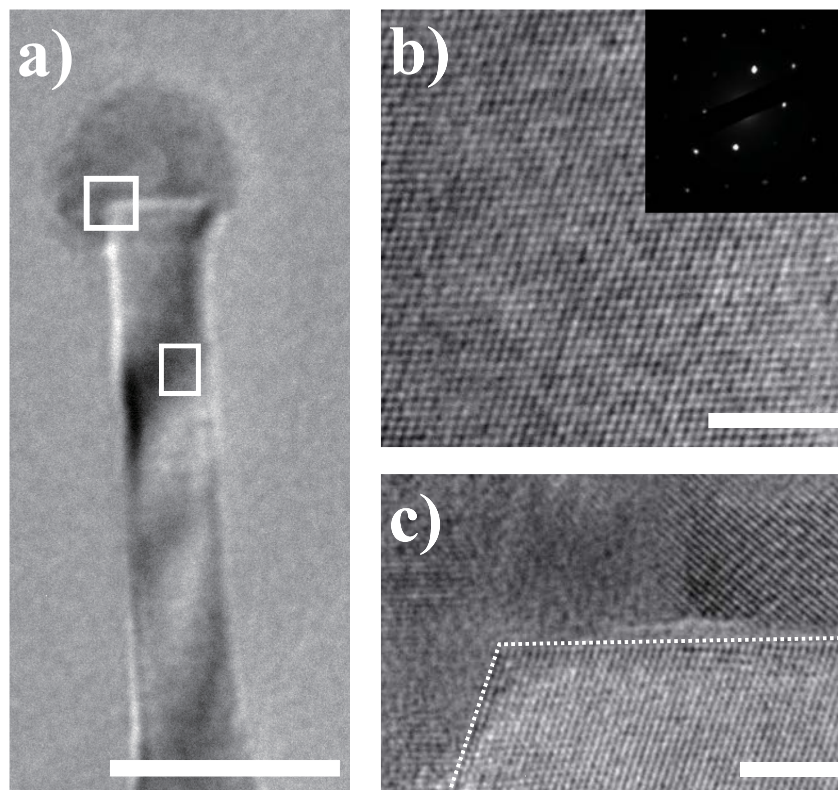

Figure 4.12. a) Transition electron micrograph of a straight section of a Ge nanowire prepared by ec-LLS with e-$BiIn_3$ at E = -1.6 V and T = 95 °C. Scale bar: 50 nm b) High resolution transition electron micrograph of the lower box in (a) highlighting the crystallinity of the nanowire section. Scale bar: 5 nm Inset: selected area electron diffraction image. c) High resolution transmission electron micrograph of the upper box in (a) that contained the interface between E-BiIn and Ge. The dashed line highlights the edge of the crystalline Ge. Scale bar: 5 nm.

indicating the nanowire was a single crystal over the entire probed area. A higher magnification electron micrograph of the e-BiIn/Ge interface was also collected (Figure 4.12c) and showed an abrupt and flat interface between Ge crystalline nanowire and the liquid metal, suggesting crystal formation by a step-flow growth mechanism.[22,23] The dashed white line in Figure 7c also highlights the 108° angle between two {111} planes wetted by the liquid metal.

Figure 4.13 separately shows transmission electron micrographs of a representative coiled section of a Ge nanowire prepared by ec-LLS with e-BiIn. Figures 4.13a and 4.13b show bright and dark-field (with the e^- beam along the <022> direction) transmission electron micrographs of the same coiled section. Two points were apparent from these data. First, the uniform contrast in the dark-field micrograph of the coiled section indicated that the entire coil segment was in fact a single crystal. Second, the crystallographic orientation of the straight and coiled sections of the Ge nanowire were misaligned and not the same since the straight section is only visible in the bright-field image, indicating the kink corresponded to a grain boundary or a change in growth direction.

Figure 4.14a shows the measured current-potential response for three straight Ge nanowires with diameters of 360 nm and various lengths. The total resistance of each nanowire, plotted as a function of the contact spacing, is shown in Figure 4.14b. The contact resistance was determined from the y-axis intercept, indicating a resistivity of $(3.2 \pm 0.3) \times 10^{-3}$ ohm·cm for these Ge nanowires[24,25] and consistent with a degenerate doping condition.

D. Discussion

The cumulative data speak to two general conclusions. First, liquid e-BiIn can fulfill the dual function requirement of electrode and crystal growth solvent required in ec-LLS. In this regard, many of the observations with e-BiIn reaffirm the basic features necessary for ec-LLS. Second, the data with e-BiIn also highlight new insights on relevant aspects of the liquid metal in ec-LLS. Specifically, the potential-dependence of complex liquid metal alloy compositions must be considered. Additionally, the same metal alloy component can either stay out of the growing crystal or strongly incorporate, depending on the other components in the liquid metal. Finally, the composition and morphology of the crystals produced by ec-LLS are strongly dictated by the metallurgy of the specific liquid metal. These points are discussed below.

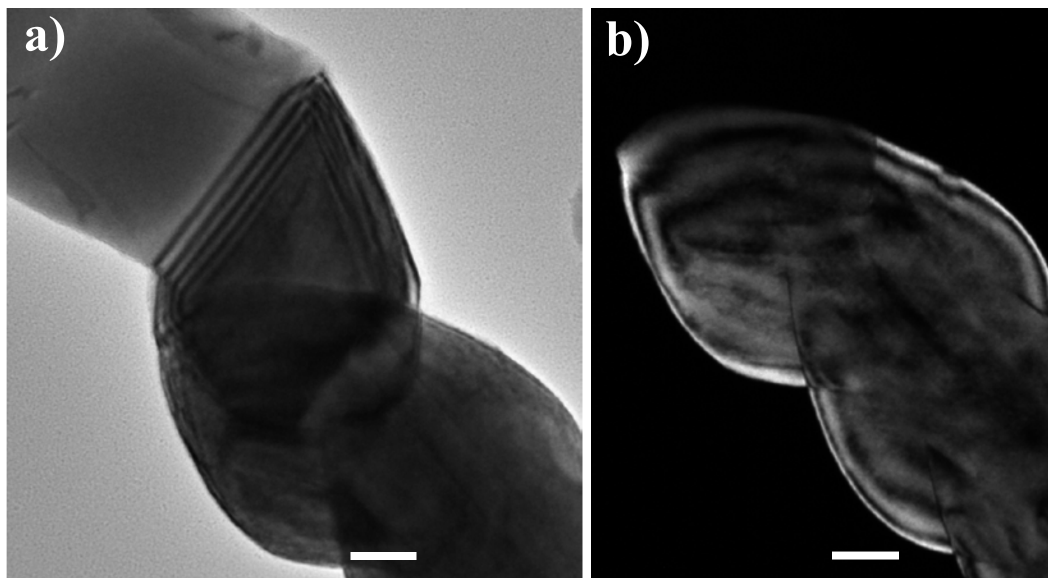

Figure 4.13. a) Bright-field transmission electron micrograph of a coiled Ge nanowire section aligned along the <220> zone axis. b) Corresponding dark-field transmission electron micrograph of the same coiled Ge nanowire section. Scale bars: 50 nm

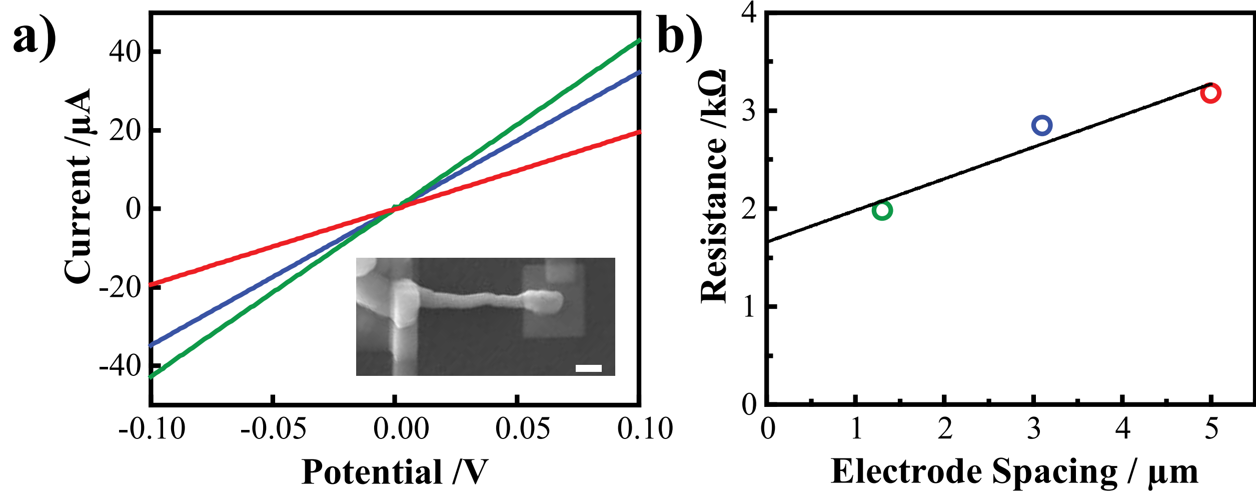

Figure 4.14. a) Current-potential responses for three separate Ge nanowire measured by two contacts. Inset: Scanning electron micrograph of Ge nanowire resistivity measurement. Scale bar: 2.5 µm b) Measured resistance vs electrode spacing for the data in (a).

In many respects, e-BiIn demonstrated several elementary features needed in ec-LLS. First, substantial crystal growth was only observed when experiments were performed above the melting point of e-BiIn. Below this critical temperature, electrodeposition experiments yielded no evidence of heterogeneous nucleation of Ge microwires or nanowires at the underlying e-BiIn/Si interface. This general observation is in accord with the premise that microwires and larger nanowires can only form by ec-LLS if the solute (Ge) is able to freely and readily diffuse from the liquid electrolyte/liquid metal interface to the liquid metal/substrate surface.[2,10] We interpret the observations below the melting point of e-BiIn to mean that the dissolution and diffusion of zero-valent Ge in solid e-BiIn is markedly slower than in liquid e-BiIn.

Second, the growth of microwires and nanowires universally featured a liquid metal cap on top of the Ge filament. The location of e-BiIn is again in accord with the premise that in ec-LLS Ge dissolves into the liquid metal, diffuses through the liquid metal volume, reaches a critical concentration at the bottom liquid metal/substrate interface, and then preferentially crystallizes at that interface. An exhaustive exploration of the temperature and size dependences in the crystallization of Ge at a Si solid surface in contact with e-BiIn was not performed here as has been done for Ge ec-LLS with e-GaIn.[2] Still, the basic observation that all of the e-BiIn caps had smooth shapes and surfaces devoid of Ge crystallites suggested that under the conditions employed here, nucleation and crystallization of Ge at the e-BiIn/Si interface was energetically more favorable than homogeneously within e-BiIn and heterogeneously at the electrolyte/e-BiIn interface. Accordingly, we consider the solvation properties of e-BiIn for Ge more akin to Ga-based liquid metals[2,7] than pure Hg,[9] where the former supports heterogeneous nano- and microwire growth while the latter does not. In this work, direct evidence of epitaxial Ge micro- or nanowire growth was not collected. However, we do not ascribe this specifically to e-BiIn. In experiments where surface oxides on e-BiIn were deliberately removed by a prolonged cathodic pretreatment prior to attempting ec-LLS, the propensity of nanowires that initially followed the <111> direction of the underlying substrate increased (Figure 4.11).

Third, the current-time transients for Ge ec-LLS experiments performed under potentiostatic control where competition with $H_2(g)$ evolution was minimized and the composition of the liquid metal was well-defined showed a familiar current decay followed by a local current maximum at long (~13 min) times. The same general shape has been observed previously in ec-

LLS.[2] Although reminiscent of the chronoamperometry of conventional electrodeposition experiments,[26] we have not attempted to extract any information on nucleation/crystal growth. All the existing models for electrodeposition processes assume no diffusion of electrodeposited species *into* the metal electrode.[26,27] This aspect, in conjunction with the moving boundary condition represented by the liquid metal droplet being displaced upwards as the micro/nanowires grow in length, is significant. Accordingly, any analysis of the chronoamperometric response in Figure 4.10 would be indeterminate at best without an appropriate model. However, the invariance of this type of chronoamperometry response with liquid metal composition suggests that a model for fitting ec-LLS data could be realized that does not necessarily include the metallurgy of the liquid metal. Such work is ongoing.

The use of e-BiIn also highlighted four interesting aspects about liquid metal electrodes in ec-LLS not previously considered. First, liquid metal alloy compositions can change at both anodic and cathodic potentials. At anodic potentials, this point has long been understood in the context of anodic stripping voltammetry,[9,28] where metals can be selectively leached out by oxidation at positive potentials. However, at cathodic potentials, the composition of a liquid metal alloy is susceptible to change, too. In the case of e-BiIn, the reductive dissolution of Bi changed the composition of the liquid metal. Specifically, we posit that Bi hydrogenation and gasification by conversion to BiH_3 occurs at potentials more negative than ~ -1.4 V. This contention is supported by the strong agreement of the more negative voltammetric wave in the first scan of Figure 4.5 with the value of $E^0(Bi/BiH_3)$ = -1.497 V predicted by the Pourbaix diagram for Bi in water[29] and the observation that the precipitate contained some Bi. The loss of the Bi-based redox waves in the voltammetry at later scans indicates that Bi is leached from the alloy, diminishing the usable potential range for Ge ec-LLS for e-BiIn. For context, this issue is likely only severe in polar protic solvents like water. If the solvent does not support any reductive leaching pathways, then the cathodic stability of this (and other Bi-based metal alloys) may be extended, providing some motivation to pursue ec-LLS in non-aqueous electrolytes.

Second, there are several preparation routes for liquid metal alloys in ec-LLS. The majority of our prior work utilized liquid metals that were molten at room temperature,[2,7,9] and droplets were prepared by forcing the liquid metal into voids with defined volumes. In this work, we demonstrate that sequential metal evaporation and subsequent melting also effects viable liquid

metal electrodes when heated above their melting point. We initially expected that there might not be uniform mixing by this method. However, elemental maps of droplet cross-sections showed uniform signals for Bi and In (Figure 4.4), indicating uniformity. With respect to formation of consistent nanodroplets, melting of discrete thin metal films is easier than the manual spreading of liquid metal when the metal melts at higher temperatures.

Third, the incorporation of metal in the crystals is nuanced. In one aspect, these data show that even with a non-Ga liquid metal composition, the resultant Ge crystal has a measurably high (~10 at %) total metal content. Although it is still premature to conclude that high metal loading is unavoidable in ec-LLS, it is nevertheless a persistent theme with the liquid metals employed thus far. As apparent in the pseudo-binary phase diagram (Figure 4.1), e-BiIn has a very low Ge solubility and the melting point is not predicted to change when saturated with Ge. We surmise that liquid metals with greater solvating power for the solute of interest and/or form mixtures with substantially lower melting points may more easily lower the residual metal content in crystals prepared by ec-LLS. Nevertheless, residual metals contents are not necessarily undesirable. With e-BiIn, as the resistivity data shown here illustrates, the high metal loading leads to strong doping character, which could be desirable if controllable. Separately, semiconductors with metal loadings in excess of the thermodynamic solubility limit are desirable for bandgap engineering in group IV semiconductors.[30]

The high metal content in these micro- and nanowires suggests solute trapping,[31-33] i.e. the growth occurred at very large supersaturation of the liquid metal that accelerated the solidification of the Ge crystal out of the liquid metal solvent. That is, when the growth rate of the crystal is fast compared to the velocity of solvent atoms at the crystal growth front, metal solvent atoms can get trapped in the crystal. The composition maps from APT analysis in Figure 5 clearly implicate the presence of metal occlusions/clusters, a feature that is indicative of crystal growth under conditions of large supersaturation. The observations from the transmission electron microscopy separately support a step-flow growth mechanism consistent with this premise. The propensity for occlusions under these conditions is well established.[32,34,35] If operative in ec-LLS, this type of crystallization suggests slower growth rates at potentials that limit the extent of supersaturation in the liquid metal ought to lead to lower levels of metal incorporation. More explicit information on the kinetics of crystal growth and the mobility of atoms on a surface immersed in a specific liquid metal would

help guide such studies. Still, the findings here strongly suggest that such ec-LLS experiments are worth exploring in the future.

In another aspect, the data here indicate there are additional, as-yet unidentified factors that affect metal content in crystals grown from liquid metal solvents. Specifically, in this study, we found that the Ge crystals had appreciable levels of both In and Bi. However, in the case of ec-LLS with e-GaIn, the amount of In that was incorporated into Ge wasnot detected by APT.[4] Apparently, the substitution of Bi for Ga strongly affects how In participates in the formation of the Ge crystals in ec-LLS. One point of relevance is the surface enrichment of individual components in liquid metal alloys. Specifically, X-ray reflectivity studies of liquid metals have shown that the surface composition can differ substantially from the bulk composition (i.e. Gibbs adsorption rule).[2,3,36] The surface compositions of both e-BiIn and e-GaIn are substantially enriched with Bi and In, respectively, because these metals have lower surface tensions relative to the other metals in each alloy.[37] Still, in the case of Bi in e-BiIn, this aspect is not sufficient to explain why Bi is present in the Ge microwires at all. From a pure size perspective, the crystal radius of Bi is much larger than either In, Ge, or Ga (0.076 nm) indicating a significant strain is required to accommodate Bi impurities into the Ge crystal lattice.[18,19]

Fourth, the coiled structure of single-crystalline nanowires has not been observed before in ec-LLS even though the same electrolyte, temperature, and potential values have been utilized previously. The data implicate that e-BiIn plays a determining factor on how the Ge crystals form. The rationale why a coiled structure is favored in e-BiIn is not clear. One possible factor is that the surface tension of e-BiIn is lower than for e-GaIn. The difference in surface tension may affect the stability/wetting of the liquid metal/Ge interface, causing greater capillary instability with e-BiIn which could affect Ge crystal growth direction.[38] The transmission electron microscopy data are consistent with this notion of the liquid metal wetting multiple crystal planes as well as the sharp change in growth direction observed in DF TEM but more work is necessary to validate this premise.

E. Conclusion

The cumulative results show that e-BiIn can be used as a liquid metal electrode that supports Ge crystal growth during ec-LLS. The physical properties of the metal impurity atoms and alloy have a significant effect on the amount of the metal impurity atoms incorporated into the

crystal and even the morphology of the nanowire. The results from this work encourage additional studies on different liquid metal alloys to better understand the impact on the morphology and the metal incorporation phenomenon. An unintended consequence was the discovery that e-BiIn supports the growth of coiled nanowires by ec-LLS, materials that may prove interesting in their own right.[39] Hence, this work encourages further studies on identifying additional liquid metals compatible with ec-LLS and understanding how their solvent properties affect crystal formation.

F. References

(1) *CRC Handbook of Chemistry and Physics*; CRC Press: Boca Raton, Fl, 2000; Vol. 122.
(2) DeMuth, J.; Fahrenkrug, E.; Maldonado, S. *Crystal Growth & Design* **2016**, *16*, 7130.
(3) DiMasi, E.; Tostmann, H.; Shpyrko, O. G.; Huber, P.; Ocko, B. M.; Pershan, P. S.; Deutsch, M.; Berman, L. E. *Phys. Rev. Lett.* **2001**, *86*, 1538.
(4) Ma, L.; Fahrenkrug, E.; Gerber, E.; Crowe, A. J.; Venable, F.; Bartlett, B. M.; Maldonado, S. *ACS Energy Letters* **2017**, *2*, 238.
(5) Zhou, J.; Sun, Y.; Xue, F. *J. Alloys Compd.* **2005**, *397*, 260.
(6) McCormack, M.; Jin, S. *JOM* **1993**, *45*, 36.
(7) Fahrenkrug, E.; Maldonado, S. *Acc. Chem. Res.* **2015**, *48*, 1881.
(8) Gu, J.; Collins, S. M.; Carim, A. I.; Hao, X.; Bartlett, B. M.; Maldonado, S. *Nano Lett.* **2012**, *12*, 4617.
(9) Zhang, T.; Fahrenkrug, E.; Maldonado, S. *J. Electrochem. Soc.* **2016**, *163*, D500.
(10) Fahrenkrug, E.; Biehl, J.; Maldonado, S. *Chem. Mater.* **2015**, *27*, 3389.
(11) Gregorczyk, Z.; Stawarz, L.; Jurzyk, E. *J. Chem. Thermodyn.* **1981**, *13*, 647.
(12) Yoo, S. J. B. *Electron. Lett* **2009**, *45*, 584.
(13) Vonk, V.; Pontoni, D.; Cremers, M.; Kerkenaar, A.; Bode, A. A. C.; Szweryn, W.; Nowak, G.; de Jong, A. E. F.; Dosch, H.; Vlieg, E. *Langmuir* **2017**, *33*, 814.
(14) Kopecek, R.; Peter, K.; Hötzel, J.; Bucher, E. *J. Cryst. Growth* **2000**, *208*, 289.
(15) Scott, W.; Hager, R. J. *J. Electron. Mater.* **1979**, *8*, 581.
(16) Kazuo, N.; Kozo, F.; Yoshitaro, N.; Noritaka, U. *Japn. J. Appl. Physics* **2005**, *44*, 5092.
(17) Mauk, M. G.; Curran, J. P. *J. Cryst. Growth* **2001**, *225*, 348.
(18) Shannon, R. *Acta Crystallogr., Sect. A: Found. Crystallogr.* **1976**, *32*, 751.
(19) Shannon, R. D.; Prewitt, C. T. *Acta Crystallogr., Sect. B: Struct. Sci.* **1969**, *25*, 925.
(20) Mahenderkar, N. K.; Liu, Y.-C.; Koza, J. A.; Switzer, J. A. *ACS Nano* **2014**, *8*, 9524.
(21) Larson, D. J.; Prosa, T. J.; Ulfig, R. M.; Geiser, B. P.; Kelly, T. F.; SpringerLink *Local Electrode Atom Probe Tomography A User's Guide*; Springer New York : Imprint: Springer: New York, NY, 2013.
(22) Wen, C. Y.; Tersoff, J.; Reuter, M. C.; Stach, E. A.; Ross, F. M. *Phys. Rev. Lett.* **2010**, *105*, 195502.
(23) Golovin, A. A.; Davis, S. H.; Voorhees, P. W. *J. Appl. Phys.* **2008**, *104*, 074301.
(24) Woodruff, S. M.; Dellas, N. S.; Liu, B. Z.; Eichfeld, S. M.; Mayer, T. S.; Redwing, J. M.; Mohney, S. E. *J. Vac. Sci. Technol., B: Microelectron. Nanometer Struct.--Process., Meas., Phenom.* **2008**, *26*, 1592.
(25) Mohney, S. E.; Wang, Y.; Cabassi, M. A.; Lew, K. K.; Dey, S.; Redwing, J. M.; Mayer, T. S. *Solid-State Electron.* **2005**, *49*, 227.

(26) Scharifker, B.; Hills, G. *Electrochim. Acta* **1983**, *28*, 879.
(27) Milchev, A. *Nanoscale* **2016**, *8*, 13867.
(28) *Electrochemical Methods: Fundamentals and Applications*; 2nd ed.; Bard, A. J.; Faulkner, L. R., Eds.; John Wiley & Sons, Inc., 2001.
(29) Pourbaix, M. *Atlas of electrochemical equilibria in aqueous solutions*; 1st ed.; Pergamon Press: Oxford, New York,.
(30) Biswas, S.; Doherty, J.; Saladukha, D.; Ramasse, Q.; Majumdar, D.; Upmanyu, M.; Singha, A.; Ochalski, T.; Morris, M. A.; Holmes, J. D. *Nature Comm.* **2016**, *7*, 11405.
(31) Allen, J. E.; Hemesath, E. R.; Perea, D. E.; Lensch-Falk, J. L.; LiZ.Y; Yin, F.; Gass, M. H.; Wang, P.; Bleloch, A. L.; Palmer, R. E.; Lauhon, L. J. *Nat Nano* **2008**, *3*, 168.
(32) Moutanabbir, O.; Isheim, D.; Blumtritt, H.; Senz, S.; Pippel, E.; Seidman, D. N. *Nature* **2013**, *496*, 78.
(33) Reitano, R.; Smith, P. M.; Aziz, M. J. *J. Appl. Phys.* **1994**, *76*, 1518.
(34) Wang, H.; Zepeda-Ruiz, L. A.; Gilmer, G. H.; Upmanyu, M. *Nature Comm.* **2012**, *4*, 1956.
(35) Brooks, R.; Horton, A. T.; Torgesen, J. L. *J. Cryst. Growth* **1968**, *2*, 279.
(36) Pershan, P. S.; Schlossman, M. L. *Liquid Surfaces and Interfaces*; Cambridge, 2012.
(37) Grosse, A. A. V. *J. Inorg. Nuc. Chem.* **1964**, *26*, 1349.
(38) Schmidt, V.; Wittemann, J. V.; Gösele, U. *Chem. Rev. (Washington, DC, U. S.)* **2010**, *110*, 361.
(39) Ren, Z.; Gao, P.-X. *Nanoscale* **2014**, *6*, 9366.

CHAPTER 5

Electrochemical Liquid-Liquid-Solid Deposition of Crystalline Gallium Antimonide

A. Introduction

Gallium antimonide (GaSb) thin films are attractive platforms for energy conversion technologies. For example, crystalline films of GaSb function as the absorber layers and /or substrate in the most efficient thermophotovoltaics [1-3], as deposition substrates for lattice matched ternary (AlGaSb, InAsSb) and quaternary (AlGaAsSb, InGaAsSb) alloys [4,5], as infrared-capturing cells in tandem solar cells [6] and as the lasing medium in low voltage diode lasers.[7] Unfortunately, the current methods (e.g. metal organic chemical vapor deposition and molecular beam epitaxy) for the production of crystalline GaSb are problematic at scale in several ways. Specifically, they rely on toxic gaseous precursors, require costly instrumentation, and do not allow high throughput [1,8]. Accordingly, a need exists to find alternative methods for the preparation of crystalline GaSb that retain quality but are better suited for rapid mass production.

In principle, conventional electrodeposition is a potential low-cost route for crystalline GaSb thin films when performed in aqueous electrolytes at/near room temperature. However, the extant literature shows several issues with conventional electrodeposition. Notably, electrodeposited GaSb is nonstoichiometric, amorphous, and contaminated with impurities from the electrolyte [9,10]. These factors individually are problematic and collectively are detrimental for electronic and optoelectronic application [11,12]. Non-stoichiometry is a direct consequence of unequal rates of incorporation of Ga and Sb in to the growing GaSb crystal. That is, the difference in the heterogeneous electroreduction rates of Ga- and Sb-containing precursors will lead to excesses/deficiencies of the constituent atoms in GaSb unless they are matched precisely. Further, electrodeposition of GaSb often results in films with high levels of impurities, both from the solvent and/or salts as well as metal contaminants in the electrolyte that were not removed prior to electrodeposition.

Finite equilibrium solubilities of both Sb^0(s) and GaSb(s) in the liquid metal permits the formation of crystalline GaSb at low temperatures. Accordingly, this chapter tests the hypothesis that an ec-LLS process can be developed for crystalline GaSb using liquid gallium electrodes and Sb_2O_3 dissolved in aqueous electrolyte. Figure 5.1 represents the ec-LLS tactic explored in this work. Through this method, we report the first demonstration of direct electrodeposition of crystalline GaSb at temperatures below the boiling point of water. Process conditions and experimental criteria for this method are identified and discussed herein.

This chapter was previously published in *Electrochemica Acta*.[13] The text and figures are reprinted with permission from Elsevier.

B. Methods

Materials. Antimony oxide (Sb_2O_3, 99% Aldrich), sodium hydroxide (NaOH, > 97%, Fisher), and Ga (99.999%, Alfa Aesar) were used as received. Water with a resistivity > 18.2 MΩ cm (Nanopure Barnstead Water Purification) was used throughout.

Electrochemical Experiments. CHI420A and CHI760C (CH Instruments) workstations and a Solartron 1286 (Solartron) potentiostat were used interchangeably for electrochemical experiments. All measurements were performed in a three-electrode Pyrex cell under ambient pressure. A liquid gallium pool housed within a glass bowl and contacted by a Pt wire that was isolated from the liquid electrolyte by a polytetrafluroethylene (PTFE) coating was used as the working electrode, Pt-mesh was used as the counter electrode, and a Pt-wire was employed as a quasi- reference electrode. All potentials were then converted to the Ag/AgCl reference potential scale through the voltammetric response of the $[Fe(CN)_6]^{3/4-}$ redox couple. Unless indicated otherwise, all potentials are reported relative to *E*(Ag/AgCl/Sat. KCl (aq)).

Materials Characterization. Raman spectra were taken using a Renishaw RM Series Raman microscope using a Nikon LU Plan 20x objective (NA = 0.4), with edge filters for the 785 nm excitation line, in a backscatter geometry. A 785 nm diode laser was used as the incident excitation source with a total radiant power of 1.12 mW over a 20 μm^2 spot which was collected for 20 seconds. The peak position of the TO mode for crystalline GaSb in the Raman spectra was obtained by fitting with a Voigt function using a max of 500 iterations with a tolerance of 10^{-15}. Scanning electron micrographs were obtained from a FEI Nova Nanolab Dualbeam Focussed Ion

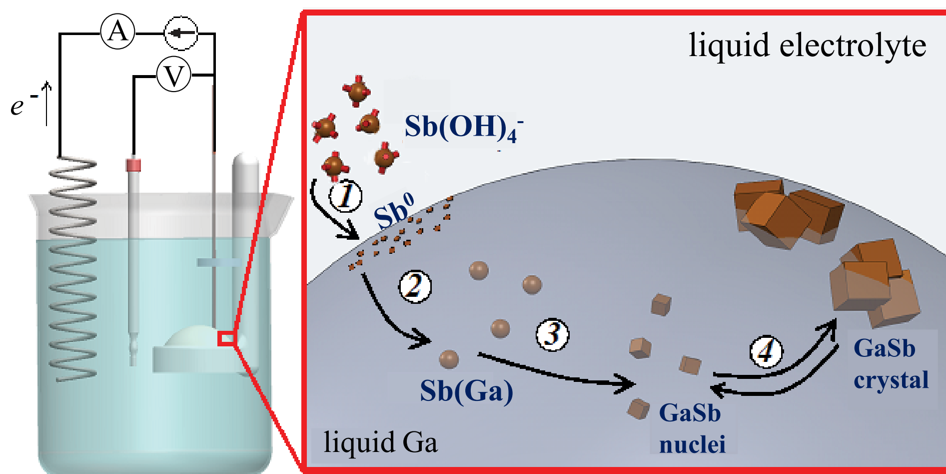

Figure 5.1. Schematic depiction of GaSb ec-LLS. (*1*) The dissolved Sb_2O_3(aq) precursor is electroreduced to Sb^0. (*2*) Dissolution of Sb^0 into the pool of Ga(l) and subsequent metallurgical alloying reaction with the liquid metal. (*3*) Supersaturation within the liquid metal phase leads to the formation of GaSb nuclei. (*4*) GaSb crystals grow and emerge from the liquid Ga pool.

Beam Workstation using a Schottky field emitter filament functioning at an acceleration voltage of 5 kV and a beam current 0.54 nA and a 1455 LEO scanning electron microscope using a tungsten filament source functioning at an acceleration voltage of 10 keV and a beam current 20 pA. The secondary electrons were collected from an Everhart-Thornly Detector (ETD) or a through–the-lens detector (TLD). Powder X-Ray diffractogram were obtained from a Bruker D8 Advance X-ray diffractometer with a Cu Kα X-ray source (λ = 1.5406 Å). The source slit was 0.6 mm using a data sampling interval of 0.040 ° for 0.7 seconds at each interval. Dark field and bright field transmission electron micrographs as well as the selected area electron diffraction pattern were collected with a JEOL 3011 TEM using a LaB_6 filament functioning at 300 kV. The TEM samples were prepared by freezing the liquid gallium (Ga(*l*)) electrode directly after the deposition and removing the surface film with a razor blade. The razor blade was then placed in a scintillation vial containing about 1 mL of methanol (190 proof, ACS spectrophotometric grade, Aldrich) and sonicating the suspension for approximately 45-60 min. A droplet of about 30 μL of the suspension was then casted onto a 400 mesh Cu TEM grid coated with an ultrathin carbon support (Ted Pella). The extensive sonication was needed due to the large particle size of the GaSb films. The SAED pattern for crystalline GaSb was simulated along the [111] space group F-43m, with the software Crystal Maker.

C. Results

Figure 5.2 shows the current-potential response at the Ga(*l*) electrode for electrolyte in the presence and absence of dissolved Sb_2O_3 at a series of different concentrations. The maximum formal concentration attainable in this electrolyte was 0.6 mM. At the electrolyte pH of 12.3, the predominant species in solution is $Sb(OH)_4^-$.[14,15] In the blank electrolyte, the liquid gallium pool electrode readily oxidized at potentials less negative than -1.2 V but was stable at more negative potentials. These liquid gallium pool electrodes showed poor electrocatalytic activity for the H^+/H_2 redox couple ($\log(J_0/\text{mA cm}^{-2}) = -10.1$, $d\log(J)/dE = -6.1\ V^{-1}$). At this pH, the standard potential for the reduction of $Sb(OH)_4^-$ is -0.720 V.[14] Upon introducing Sb_2O_3 into solution, the cathodic current increased, indicating the liquid gallium electrode is active for the electroreduction of $Sb(OH)_4^-$. However, a cathodic wave indicative of a diffusional limit for the reduction of $Sb(OH)_4^-$ was not cleanly observed. Prolonged chronoamperometric experiments at potentials $\leq$ -1.27 V resulted in the electrodeposition of a film. Figures 2b and 2c show the Ga(*l*) pool electrode before

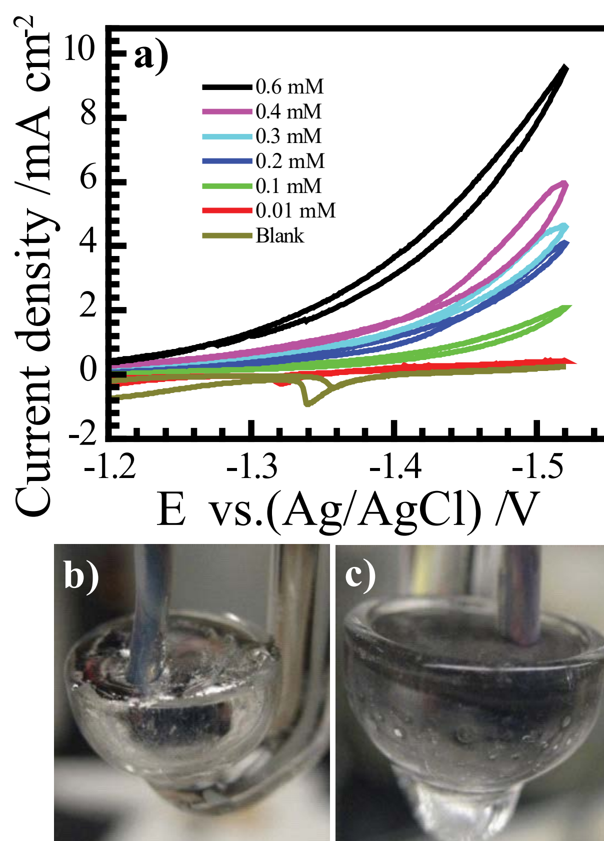

Figure 5.2. a) Voltammetric responses for a Ga(l) working electrode in an aqueous electrolyte containing 0.6 M NaOH with and without dissolved Sb_2O_3(aq) at various formal concentrations up to the solubility limit at 25 ºC with a scan rate of 10 mV/s. b,c) Optical photograph of a clean Ga(*l*) pool working electrode with a geometric surface area of 0.615 cm^2 housed in a glass bowl (V = 350 cm^3) before (b) and after (c) applying E = -1.47 V vs Ag/AgCl for 1 hour while submerged in an aqueous electrolyte containing 0.1 mM Sb_2O_3 and 0.6 M NaOH. Electrical contact was made through a top Pt wire insulated from the electrolyte by polytetrafluoroethylene.

and after being submerged in the 0.6 M NaOH electrolyte with an applied bias of -1.47 V for 60 min. After approximately 25 to 30 minutes, uniform films with a dark hue consistently appeared on the electrode surface under these conditions.

To ascertain the chemical identity of the films, Raman spectra were collected. Figure 5.3 shows Raman spectra of the films formed after electrodeposition for 60 min at 90 °C at different applied potentials. For experiments where the Ga(*l*) electrode was held at open circuit potential (E = -1.23 V), the Raman spectra showed two large features at about 115 and 149 cm^{-1}, which is consistent with phonons for crystalline Sb^0 (E_g and A_{1g}, respectively).[16,17] At potentials that induced a large net cathodic current, the corresponding Raman spectra of the film showed only a single peak at approximately 226 cm^{-1}. This signature was inconsistent with any known mode for crystalline or amorphous Sb^0. Rather, the data more closely agreed with an assignment of the transverse optical phonon mode of crystalline GaSb [18-21]. Nevertheless, there was no signal consistent with the longitudinal optical (LO) phonon mode. Unlike most other III-V semiconductors, the peak positions for the LO and TO phonons are closely spaced in the Raman spectra of crystalline GaSb (TO mode ~ 226 cm^{-1} and LO mode ~ 232).[16,20,21] In polycrystalline GaSb samples, only one peak is typically resolved.[20]

Generally, the peak positions of the optical phonon modes and the crystallite domain size are strongly correlated. However, earlier studies of the annealing of disordered GaSb films via Raman spectroscopy established that the spectral features do not directly report on crystal size as in other III-V semiconductors.[20] Specifically, although similar qualitative trends (blue shift of modes in Raman spectra and peak width narrowing) were observed with increasing crystallite size, the quantitative correlation of spectral features and the crystallite size (i.e. extent of phonon confinement) was poor.[20] Accordingly, attempts to estimate crystalline domain sizes from the collected Raman spectra were not performed here. Nevertheless, the peak position and linewidth of this signature in the Raman spectra collected did not change in experiments as a function of potential, implying a nominally constant crystallite size at different applied potentials.

The features in the collected Raman spectra were dependent on the formal concentration of Sb_2O_3 in the electrolyte. Figure 5.4 shows Raman spectra of electrodeposited films for a constant time (t = 60 min) as a function of the formal Sb_2O_3 concentration over a range of 0.01 – 0.6 mM. The cumulative spectral features are collected in Table 5.1. The peaks in the Raman spectra were

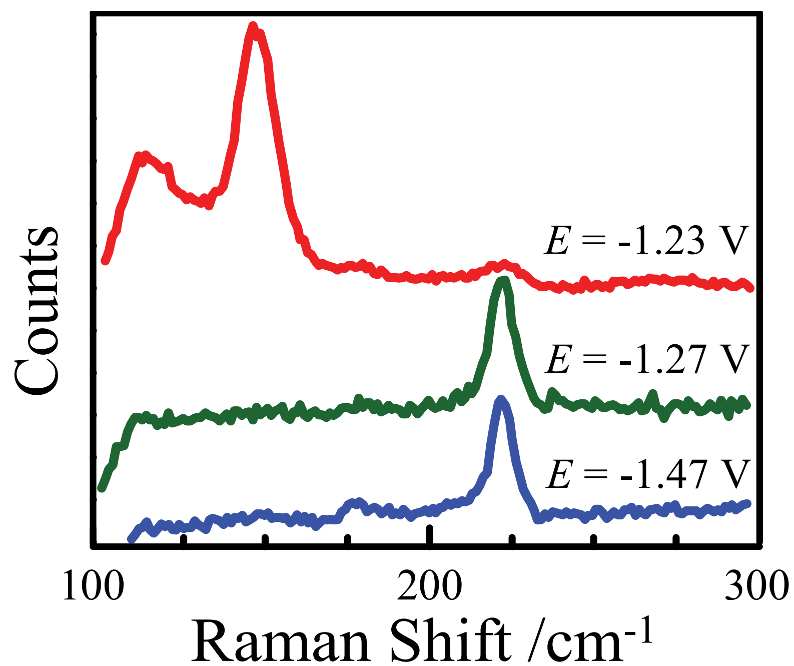

Figure 5.3. Normalized Raman spectra for films deposited on Ga(l) after being immersed in aqueous 0.6 M NaOH with Sb_2O_3 dissolved at a formal concentration of 0.1 mM while being held at a constant applied potential for 60 min at T = 90 ºC. Spectra are offset vertically for clarity.

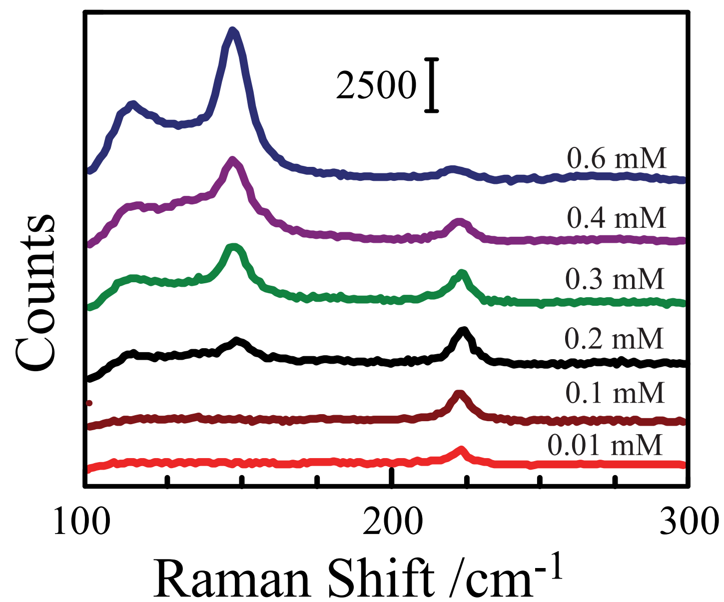

Figure 5.4. Raman spectra of films deposited on the Ga(l) electrode submerged in an aqueous electrolyte of 0.6 M NaOH with several different concentrations of the Sb_2O_3 precursor and held at E = -1.47 V for 60 min at T= 90 ºC. Spectra are offset vertically for clarity.

integrated and analyzed using Origin software. From 0.1-0.6 mM, the absolute intensity of the TO phonon mode for GaSb decreased as the concentration of Sb_2O_3 increased. For concentrations of 0.2 mM or higher, spectral features diagnostic of crystalline Sb^0 were observed. At high concentrations, these features dominated the spectra. At low concentrations ($[Sb_2O_3] \leq 0.1$ mM), the spectra indicated a 'clean' electrodeposition product of crystalline GaSb, mirroring earlier observations in the electrodeposition of crystalline GaAs at liquid gallium pool electrodes.[22] Since the peak position of the GaSb TO mode in the Raman spectra does not significantly change as the concentration is varied from 0.01 to 0.4 mM, the crystallite size within GaSb films appeared insensitive to the formal concentration of dissolved Sb_2O_3.

Figure 5.5 presents Raman spectra of electrodeposited films as a function of the electrodeposition temperature. The lower bound on the investigated temperature range was $T = 40$ ºC to ensure that the Ga was molten during the deposition ($T_{melt} = 29.7$ ºC) [23]. All spectra possessed a discernible signal (above the background) consistent with the TO phonon mode for crystalline GaSb. However, the spectra differed significantly in other aspects. First, both the intensity and the line width of the TO phonon mode was a strong function of temperature. Second, a broad mode between 110 and 175 cm^{-1} was evident at $T = 40$ and 50 ºC only. A similar feature in the Raman spectra of amorphous GaSb has been assigned as the longitudinal phonon mode.[17,20] Accordingly, we interpret this feature as diagnostic of GaSb with extremely low order (high disorder). In spectra where this mode was present, the TO mode for GaSb was redshifted, consistent with the premise of small domains of ordered GaSb. Third, the intensity of this 'disorder' feature vanished in Raman spectra where the GaSb TO phonon mode shifted to higher frequencies (Figure 5.5b). A similar temperature dependence of Raman spectral features was reported previously in annealing studies of GaSb films.[20]

Two additional experiments were performed to ascertain whether the GaSb films electrodeposited (*1*) first as amorphous thick films that were then converted thermally to crystalline materials or (*2*) directly as crystalline films, i.e. they never were amorphous. First, a series of Raman spectra were obtained for electrodepositions performed at $E = -1.47$ V at $T = 90$ °C at several durations (Figure 5.6). At the start of the experiment, there was no observable film on the electrode surface and no discernable Raman signal between 100 and 300 cm^{-1}. After 0.5 min, the background increased, with a broad profile spanning 100 ~ 250 cm^{-1}. A small fraction of the

Table 5.1. Raman spectra features at various concentrations of Sb_2O_3

$[Sb_2O_3]^a$ /mM	Peak Position cm^{-1}	FWHM /cm^{-1}	Relative Intensity[b]	Assignment
0.01				
	225.8	6.24	1	GaSb TO
0.1				
	225.8	8.16	1	GaSb TO
0.2				
	116.3	13.29	0.27	Sb^0 Eg
	150.1	11.09	1.35	Sb^0 A1g
	225.8	6.83	1	GaSb TO
0.3				
	118.6	18.43	1.13	Sb^0 Eg
	151.2	11.36	3.26	Sb^0 A1g
	225.8	7.06	1	GaSb TO
0.4				
	119.7	12.87	2.10	Sb^0 Eg
	150.1	16.85	8.55	Sb^0 A1g
	225.8	8.33	1	GaSb TO
0.6				
	117.5	21.42	14.48	Sb^0 Eg
	150.1	12.64	25.68	Sb^0 A1g
	222.5	10.01	1	GaSb TO

a. formal concentration of Sb_2O_3 dissolved in aqueous solution

b. relative to signal at 225 cm^{-1}

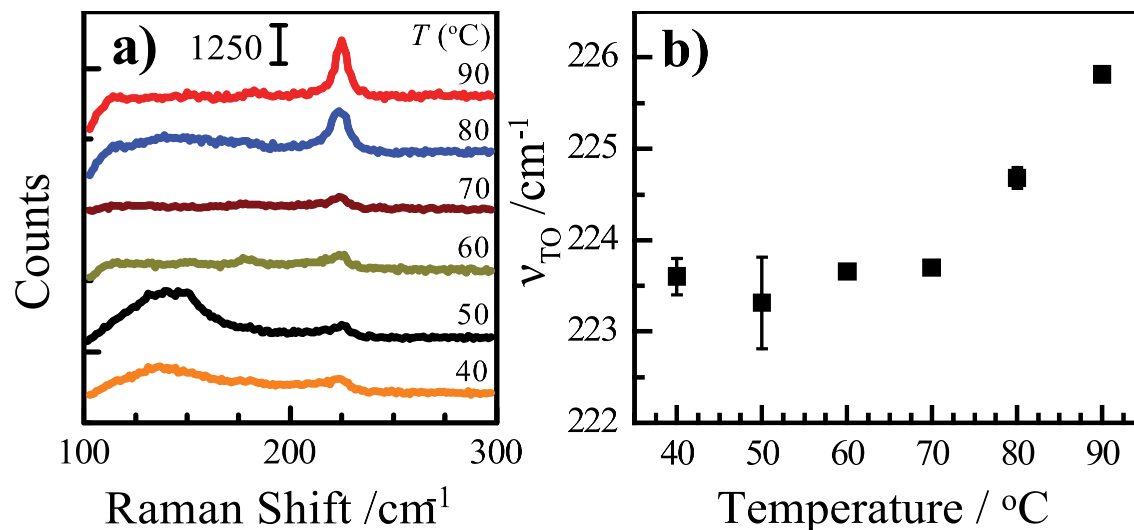

Figure 5.5. (a) Raman spectra of GaSb films deposited on a Ga(l) pool electrode with each trace corresponding to a different temperature used in the deposition. The Ga(l) was held at a constant potential of -1.47 V in 0.6M NaOH with dissolved Sb_2O_3 at a formal concentration of 0.1 mM for 60 min. Spectra are offset vertically for clarity. (b) The observed Raman shift of the TO phonon mode of bulk crystalline GaSb (ν) vs the growth temperature of each deposition. Error bars represent the standard deviation for *N* = 3.

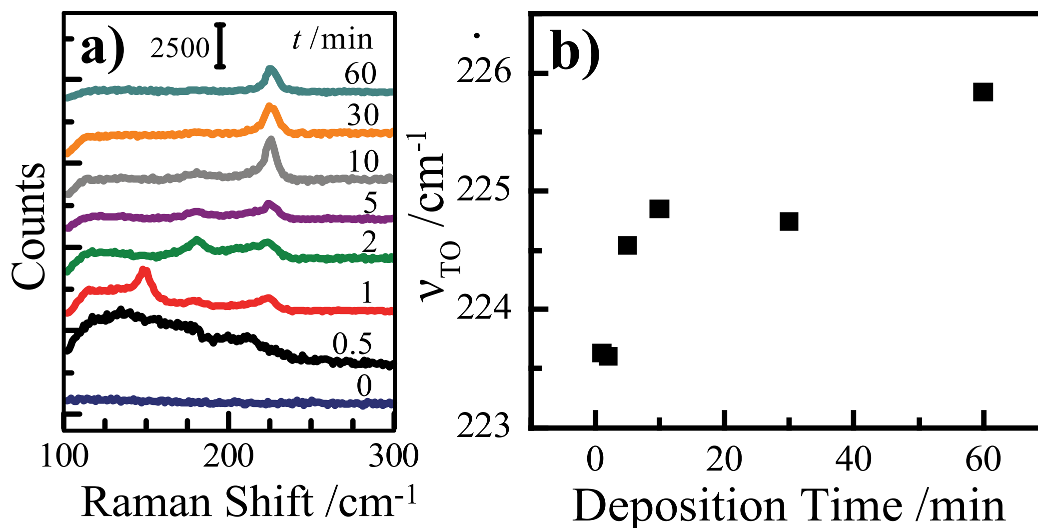

Figure 5.6. (a) Time-dependent Raman spectra of films deposited at a Ga(l) electrode at *E* = -1.47 V in aqueous 0.6M NaOH with dissolved Sb_2O_3 at a formal concentration of 0.1 mM at *T*= 90 ºC for the indicated deposition time. The intensity of the traces corresponding to the 0 and 0.5 min depositions have been multiplied by a factor of 5 and all of the spectra are offset for clarity. (b) Raman shift of the TO phonon mode of c-GaSb versus the deposition time.

surface began to show different Raman spectra. These areas showed a peak at 150 cm^{-1} while the phonon for GaSb appeared at 223.5 cm^{-1}. Although acoustic phonon modes are not typically observed for crystalline GaSb due to selection rules,[24] GaSb has a longitudinal acoustic mode at 150 cm^{-1} which has been observed in GaSb with short range order.[17] Another peak at 179 cm^{-1} was observed but was not readily assignable. After 2 min, the Raman spectra changed again and were more uniform across the electrode surface. The feature at 150 cm^{-1} disappeared. After 10 min the overall spectra remained essentially unchanged aside from a slight redshift in the TO mode of GaSb which now dominated the spectra. The measured Raman shift of the TO mode is consistent with that previously reported for crystalline GaSb ranging from 224 to 228 cm^{-1}.[18,20,21,24] Figure 5.5b shows the Raman shift in the TO mode as a function of the electrodeposition time. These data collectively imply that the GaSb crystallites were actively growing during the course of the entire ec-LLS experiment.

Second, a separate experiment was performed where GaSb films were electrodeposited at T = 40 °C for 60 min and subsequently heated at T = 60 °C for 60 min. The purpose of this experiment was to determine whether a GaSb film showing poor crystallinity could be 'annealed' in the blank electrolyte under potential control (to prevent oxide formation) to a more crystalline form and yield spectra equivalent to an ec-LLS performed at T = 60 °C. In this experiment, the broad signal between 110 and 175 cm^{-1} in the Raman spectra persisted (i.e. did not disappear) and the GaSb TO mode red shifted slightly. Both of these features were not observed in the Raman spectra of the films deposited by ec-LLS at T = 60 °C and both observations actually imply a *decrease* in GaSb crystallite size. Accordingly, the data suggest that the materials produced by ec-LLS at a given temperature are **not** the same as those electrodeposited at lower temperatures and then subsequently annealed at the given temperature.

The morphology of the GaSb crystals produced by ec-LLS was assessed through electron microscopy. The microscopic structures of GaSb films prepared by ec-LLS lasting 60 min are shown in Figure 5.7. The electrodeposits were films with a thickness of 1.06 µm +/- 6% (N = 25 measurements from 5 different regions). The films were contiguous but easily fractured into discrete, faceted particles as large as 4-5 µm in length and 8 µm in width when mechanically moved. The films yielded an X-ray diffractogram that showed all of the expected signatures for crystalline GaSb (Figure 5.8). The relative intensities of the diffraction pattern were inconsistent

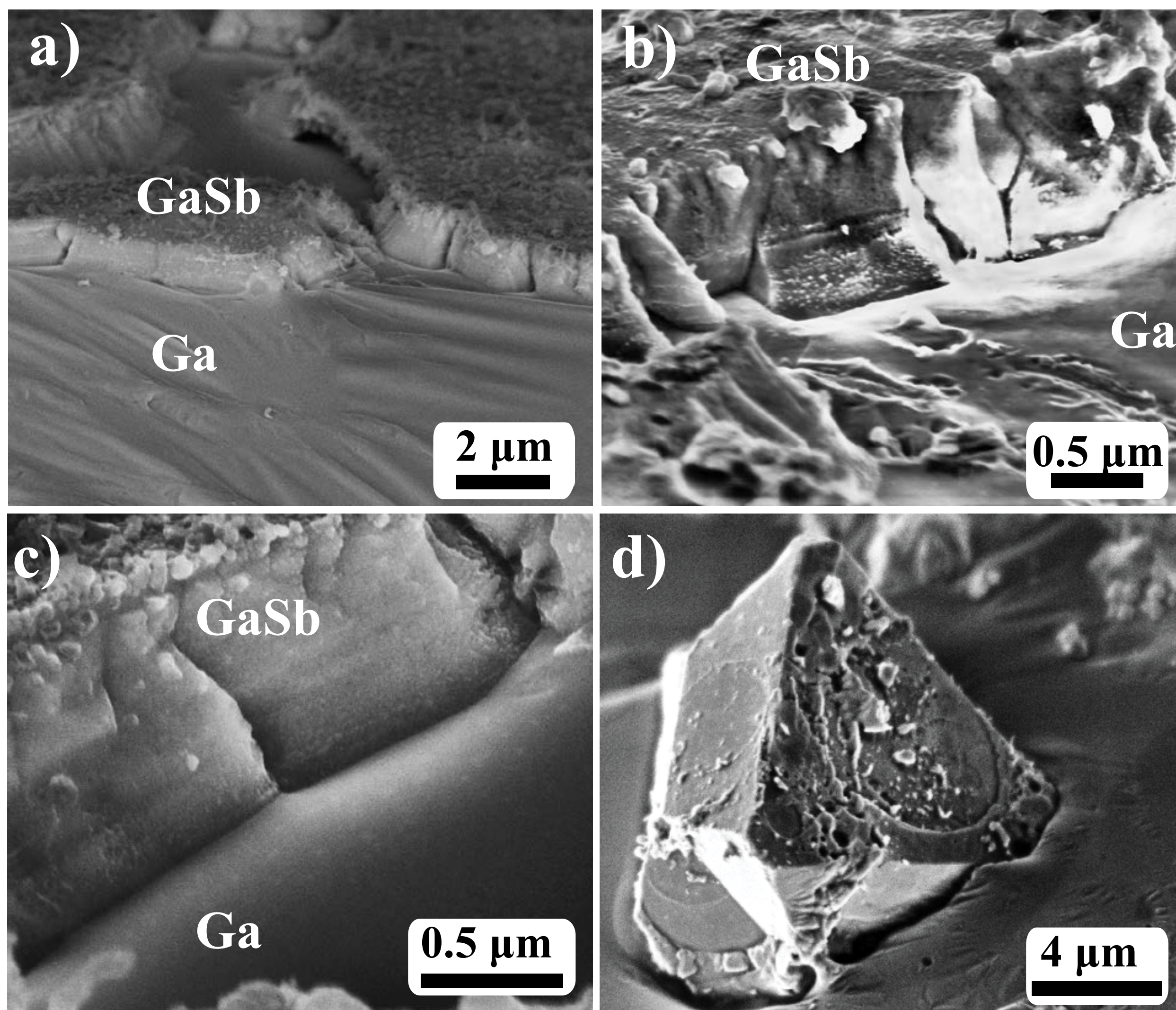

Figure 5.7. Scanning electron micrographs of films deposited on a Ga(l) pool electrode submerged in an aqueous 0.6 M NaOH with Sb_2O_3 dissolved at a formal concentration of 0.1 mM and held at E = -1.47 V for 1 hr. (a-c) Shows cross sectional images of the visible portions of undisturbed films approximately 1 μm above the liquid metal surface. (d) An individual GaSb grain after removal from the liquid metal electrode.

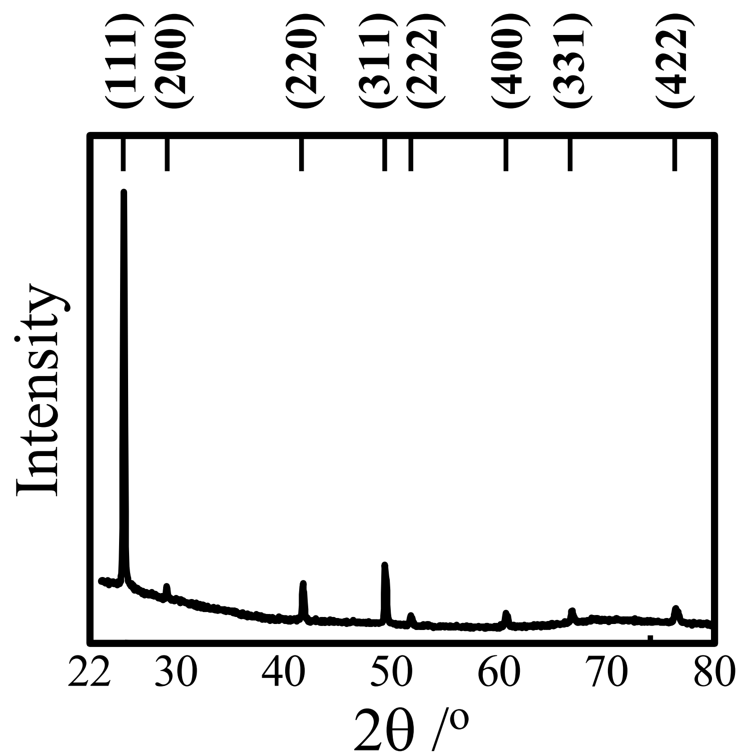

Figure 5.8. Representative Powder X-ray diffractogram collected from a film deposited on a Ga(l) pool electrode after being submerged in an electrolyte containing 0.1 mM Sb_2O_3 and 0.6 M NaOH at 90ºC while held at a constant potential of -1.47 V for 60 min. The 2θ values for the expected crystallographic planes of zinc blende GaSb are denoted at the top.

with randomly oriented isotropic crystallites, even after correcting for the attenuation in the relative diffracted intensity observed for higher angle reflections in thin films using absorption factor.[25] Rather, the data suggested that there was a texture or a preferred orientation of the {111} crystallographic planes normal to the surface plane of the Ga(l) electrodes. However, the non-flat form factor of the underlying liquid metal substrate limited quantitative assessment of anisotropy from the X-ray diffraction data. Nevertheless, the narrow peak width of the (111) signal suggests that the crystallites were larger than 0.2 μm in at least that direction.

Transmission electron microscopy (TEM) and selected area electron diffraction (SAED) were employed to directly measure the crystallite grain size in films that had been removed from the liquid gallium electrode surface, sonicated, and then recast onto a TEM grid. The prolonged sonication used to prepare the TEM sample mechanically shattered the original crystallites. Figure 5.9a shows the observed SAED pattern along the [111] zone axis. The distance between the 000 and 2-20 diffracted beams was 0.467 $Å^{-1}$, corresponding to an interplanar spacing of 2.14 Å between adjacent 2-20 crystallographic planes. The measured value is in good agreement with the interplanar spacing predicted in the SAED pattern simulated for crystalline GaSb (Figure 5.9b). Dark field (DF) transmission electron micrographs of the crystallite shown in the corresponding bright field (BF) transmission electron micrograph (Figure 5.9c and d, respectfully) showed the grain size of a section of the electrodeposited film. The DF image was obtained after selecting for the 2-20 diffracted beam and shows that the diffraction contrast from the 2-20 plane is observed throughout the crystallite with a projected domain size of about 0.2 μm x 0.1μm. The non-uniform diffraction contrast in the DF TEM image was attributed to irregular crystallite thickness.[26]

D. Discussion

The cumulative data speak to three separate points. First, the direct electrodeposition of crystalline GaSb from an aqueous electrolyte at moderate temperatures is possible and reproducible. Second, the crystalline properties of electrodeposited GaSb are a complex function of several process variables. Third, the process has strong parallels to our earlier demonstration of the direct electrodeposition of crystalline GaAs through the electroreduction of As_2O_3 at liquid gallium electrodes.

Direct Formation of Crystalline GaSb A key aspect of this work is the spontaneous formation of GaSb when Sb^0 is introduced onto/into liquid gallium. At room temperature, the ΔG_f

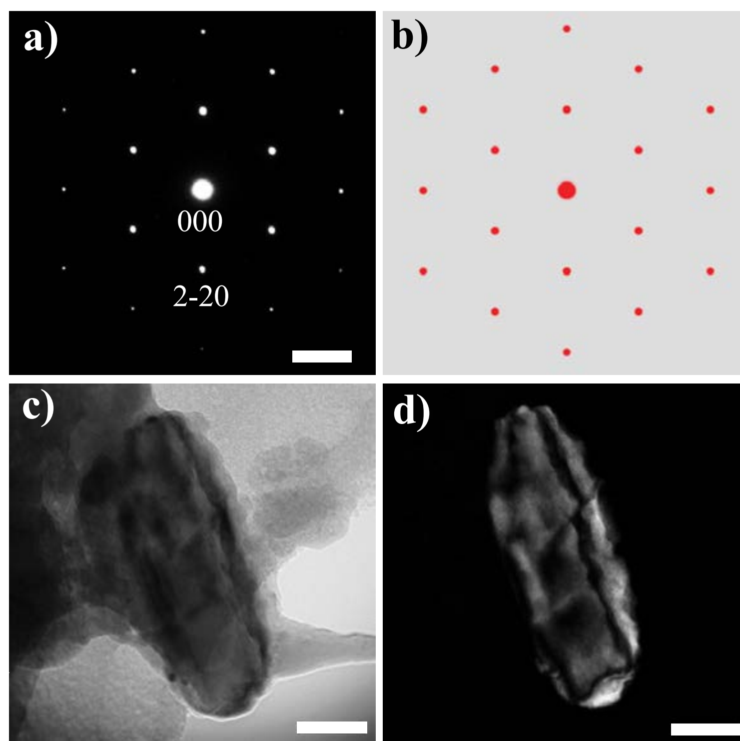

Figure 5.9. (a-d) Transmission electron micrographs and selected area diffraction patterns of GaSb crystallites prepared under conditions as described in Figure 5.6. The (a) experimental and (b) modeled electron diffraction patterns observed along the [111] zone axis of a GaSb crystallite. (c) A dark field transmission electron micrograph formed by selecting for the 2-20 diffracted beam. (d) The complementary two-beam bright field comprised of the 000 and 2-20 beams. Scale bars = (a) 0.4 $Å^{-1}$, (c and d) 40nm.

for the reaction between elemental Ga and Sb is between -51.9 and -54.3 kJ mol^{-1}.[27] That is, as long as Ga^0 and Sb^0 are in intimate contact, some amount of GaSb should be formed. A general premise in electrodeposition processes is that the size of the initial nucleus during an electrodeposition process is a strong function of both the overpotential of the electroreduction and the concentration of oxidized precursor in solution.[28] As pictorially diagrammed in Figure 5.10, our contention is that when electrodeposition is performed under conditions that favor a high density of Sb nuclei that quickly form large clusters, dissolution of Sb^0 into Ga is impeded. Conversely, when the initial electrodeposition is performed under conditions encouraging the formation of small Sb^0 nuclei that remain isolated, then the electrochemical potential gradient across the electrolyte/electrode interface is effective at driving Sb^0 dissolution to the point of supersaturation. When the formal concentration of Sb_2O_3 is large, the issue with high densities of Sb^0 accumulating at the electrode surface is apparently unavoidable. That is, crystalline Sb^0 is the main product and GaSb is only formed sparingly. In dilute solutions of dissolved Sb_2O_3, Sb^0 nuclei are discrete and readily dissolved into Ga and form GaSb, apparently outpacing the rate of accumulation of discrete Sb^0 nuclei into macroscopic clusters. At larger negative overpotentials, the heterogeneous reduction rate for the electrode reaction $[Sb(OH)_4]^-$ (aq) + 3 e^- → Sb^0(s) + 4 OH^- (aq) increases and the interspacing between discrete nuclei will decrease on the electrode.[28,29] Consequently, a more negative overpotential in a deposition would again be expected to favor the formation of Sb^0 on the Ga electrode surface rather than GaSb. However, in experiments where the overpotential for electrodeposition was made more negative the expected result was not observed. Rather, as long as the applied potential was more negative than the open circuit potential, then crystalline GaSb was always favored over Sb^0. In addition, we observed repeatedly that the formation of crystalline Sb^0 was favored over GaSb at open circuit. We propose that the formation of crystalline Sb^0 at open circuit was a result of a Galvanic displacement reaction between the $Sb(OH)_4^-$ / Sb^0 couple and the Ga^0 / GaO_3^{3-} couple.[15] We speculate that under these conditions Sb^0 forms grains too large to readily dissolve in liquid Ga, thereby precluding the possibility of extensive formation of GaSb.

Temperature Dependence For electrodepositions performed below 60 ºC, the presented data suggest that only GaSb with short range order was produced. The mode emerging at around 150 cm^{-1} tentatively assigned as the longitudinal acoustic mode [18,20] has an unusually large relative intensity. Accordingly, this feature could separately indicate amorphous Sb^0 [17] is produced below

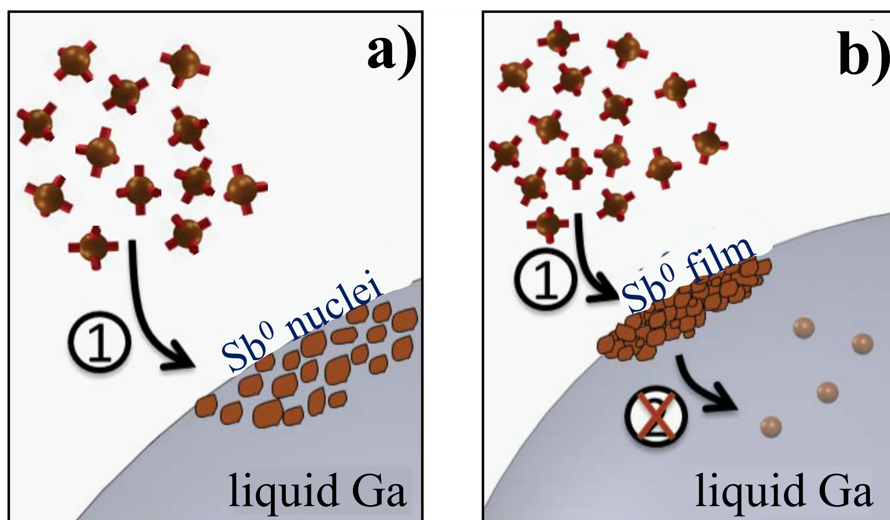

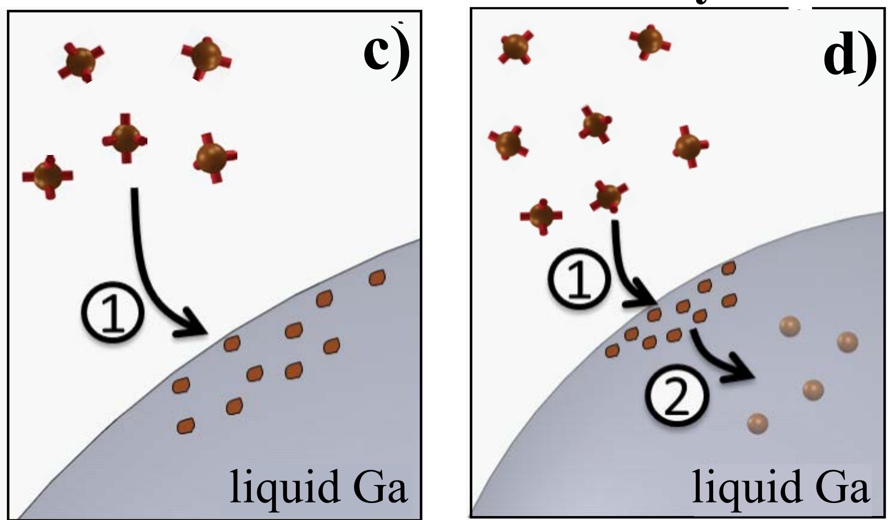

Figure 5.10. Schematic depiction of the first step and second steps in the proposed scheme for ec-LLS as influenced by conditions that favor high densities and low densities of electrodeposited Sb^0 nuclei.

this threshold temperature, i.e. the electrodeposited materials are not stoichiometric. The origin of this specific threshold temperature is unclear. We posit that some (or multiple) step(s) in the GaSb crystal growth have activation energies comparable to these temperatures. However, we do **not** believe this aspect is tantamount to electrodeposition of amorphous GaSb and separate thermal annealing as the route to crystalline GaSb. Experiments performed where GaSb was electrodeposited below the threshold temperature and then annealed just above the threshold temperature conclusively showed no increased crystallinity.

The duration of the electrodepositions performed here similarly influenced the apparent crystallinity. The Raman spectra collected at short times suggested the presence of GaSb with only short range order.[17,20] The disappearance of signatures suggestive of Sb^0 and the peak shift of the TO mode both suggest that the GaSb crystallites became more defined throughout the course of the electrodeposition. If correct, these observations support the premise of a dynamic equilibrium within the liquid metal between dissolved GaSb and solid GaSb, emphasizing the value of the metallurgical properties of the liquid metal electrode in ec-LLS.

Comparing and Contrasting GaSb and GaAs ec-LLS Three main observations were consistent between the ec-LLS processes for GaSb and GaAs. First, the concentration of the dissolved precursor strongly determined whether the electrodeposited film was composed of the target III-V compound or mainly the pure group V element. Second, the crystalline quality of the electrodeposited film was more sensitive to changes in the temperature than to changes in the applied potential. Simply, increasing the overpotential used for ec-LLS did not affect a discernible change in the observable crystallite size. Third, a temperature threshold was apparent, below which only disordered III-V films were observed. These cumulative observations support the general premise that ec-LLS for GaSb and GaAs operates by the scheme outlined in Figure 5.1. Specifically, crystal nucleation and growth occur after the initial electroreduction is evident and likely not at the electrolyte/liquid metal interface. The exact location where crystal growth initiates and continues cannot be determined from the data collected here. We have previously shown the possibility for heterogeneous crystal nucleation in ec-LLS[30,31] but that requires that the dimensions of the liquid metal electrode are small enough to ensure transport to a nucleating interface. In both the system presented here and previously for GaAs at bulk liquid Ga pool electrodes, the nucleation and crystal growth likely occurs homogeneously, i.e. within the liquid gallium electrode. The depth

from the liquid electrolyte/liquid metal interface into the bulk liquid metal at which this homogeneous nucleation occurs is not presently known.

Despite the similarities, the GaSb ec-LLS process also differs significantly from GaAs ec-LLS. Anecdotally, the formation of a visible film appeared to take longer during GaSb ec-LLS as compared to GaAs ec-LLS. That is, the Ga electrode began to change its visible hue (to yellow) within the first 10 minutes of GaAs ec-LLS[22] while in GaSb ec-LLS the Ga electrode appeared unchanged for up to 30 min. In addition, the data indicated the crystallite size is larger for GaSb than GaAs by factors of 10^2 -10^3 at the same process temperatures. Similarly, the GaSb film thickness is about 15 times larger than what was observed for GaAs electrodeposition lasting 120 min.

An important difference between Sb and As is the fact that the former is approximately 10^5 times more soluble in Ga than the latter, as determined from the corresponding phase diagrams extrapolated to the temperatures explored here.[22,32-34] The difference in the equilibrium solubility has several consequences. First, the greater solvating power of Ga towards Sb^0 means that a larger absolute concentration is needed to reach supersaturation for GaSb as compared to GaAs. Second, the rate of dissolution into Ga is necessarily different. Specifically, the rate of dissolution of a solute into a solvent is given by eq *1,* [35]

$$\frac{\partial C}{\partial t} = \frac{DS\left(C_{eq} - C\right)}{Vh} \tag{14}$$

where $\partial C/\partial t$ is the dissolution rate, D is the diffusion coefficient of the solute, S is the surface area of the solid in contact with the solvent, V is the volume of the dissolving medium, h is the height or thickness of the boundary layer (between the solid Sb^0 and the bulk liquid Ga pool), C_{eq} is the equilibrium solubility of the solute in the solvent, and C is the concentration of the solute at a specific location and time. Even when the electroreduction rates of the oxidized precursor yields similar surface concentrations and shapes/densities of As^0 and Sb^0 at the electrolyte/Ga interface, the rate of Sb^0 dissolution should be inherently faster as compared to the rate for As^0 by virtue of the value of C_{eq} (assuming D is the same). This aspect correspondingly implies the Sb^0 concentration gradient as a function of distance (i.e. from the surface to the interior of Ga) will be smaller than the concentration gradient for As^0 since the latter won't diffuse as far before undergoing homogeneous nucleation. Simply, Sb^0 ought to diffuse to a greater depth within the

liquid metal. The combination of both the larger absolute concentration needed to reach supersaturation as well as the faster dissolution rate could potentially lead to the longer time it took to optically observe the film. However, following nucleation, the crystal growth rate is a function of the absolute solute concentration,[35] where crystals grow faster and larger in solutions with a higher concentration of solute. The fact that the GaSb crystals and resultant films are larger and thicker than those observed for GaAs ec-LLS is in accord with this perspective.

These discrepancies between the deposition of GaSb and GaAs further bolster the claim that ec-LLS is a hybrid deposition process (electrodeposition + solution-based crystal growth). That is, the electrochemical driving force for electrocrystallization (the overpotential) has only an indirect effect on crystallinity but factors that affect supersaturation (the driving force for solution-based crystal growth) within Ga have a profound effect on the resultant quality and yield of the deposit. Nevertheless, a more descriptive and quantitative model of crystal nucleation/growth in ec-LLS is still needed to rationalize the particular differences in nucleation rates and total film thicknesses. Such work is ongoing in our lab.

E. Conclusions

Crystalline GaSb was electrodeposited through ec-LLS under mild process conditions. X-ray diffraction, electron microscopy, electron diffraction, and Raman spectroscopy illustrated the electrodeposited material was crystalline GaSb at $T \geq 60$ °C and at formal concentrations of Sb_2O_3 below 0.1 mM and applied potentials more negative than -1.26 V vs Ag/AgCl. The collected Raman spectra implicated Sb^0 and disordered GaSb as the major and minor products outside of these conditions. The presented analysis illustrated that temperature and electrodeposition time were the only factors that strongly affected the apparent crystallite size. In this way, the general features of the GaSb ec-LLS process followed the features for GaAs ec-LLS under the same conditions. However, clear differences in the crystals produced suggest that the metallurgical properties of the solute-liquid metal pairing have a significant impact on the nature of the resultant semiconductor crystals.

F. References

(1) Mattarolo, G. *Development and Modelling of a Thermophotovoltaic System*; Kassel University Press, 2007.
(2) Wang, C. A.; Choi, H. K.; Ransom, S. L.; Charache, G. W.; Danielson, L. R.; DePoy, D. M. *Appl. Phys. Lett.* **1999**, *75*, 1305.
(3) Juang, B.-C.; Laghumavarapu, R. B.; Foggo, B. J.; Simmonds, P. J.; Lin, A.; Liang, B.; Huffaker, D. L. *Appl. Phys. Lett.* **2015**, *106*, 111101.
(4) Milnes, A. G.; Polyakov, A. Y. *Solid-State Electronics* **1993**, *36*, 803.
(5) Dutta, P. S.; Sangunni, K. S.; Bhat, H. L.; Kumar, V. *J. Cryst. Growth* **1994**, *141*, 476.
(6) Fraas, L. M.; Girard, G. R.; Avery, J. E.; Arau, B. A.; Sundaram, V. S.; Thompson, A. G.; Gee, J. M. *J. Appl. Phys.* **1989**, *66*, 3866.
(7) Motosugi, G.; Kagawa, T. *Japn. J. Appl. Phys.* **1980**, *19*, 2303.
(8) Capper, P.; Mauk, M.; Wiley Online, L. *Liquid phase epitaxy of electronic, optical, and optoelectronic materials*; Wiley: Chichester, England ; Hoboken, NJ, 2007.
(9) Paolucci, F.; Mengoli, G.; Musiani, M. M. *J. Appl. Electrochem.* **1990**, *20*, 868.
(10) McChesney, J. J.; Haigh, J.; Dharmadasa, I. M.; Mowthorpe, D. J. *Opt. Mater.* **1996**, *6*, 63.
(11) Sopori, B. In *Proceedings-SPIE the International Society for Optical Engineering*; International Society for Optical Engineering; 1999: 2000; Vol. 2, p 1214.
(12) Mishra, U. K.; Singh, J.; SpringerLink *Semiconductor Device Physics and Design*; Springer: Dordrecht, 2007.
(13) DeMuth, J.; Ma, L.; Fahrenkrug, E.; Maldonado, S. *Electrochim. Acta* **2016**, *197*, 353.
(14) Bard, A. J.; Parsons, R.; Jordan, J.; International Union of, P.; Applied, C. *Standard potentials in aqueous solution*; M. Dekker: New York, 1985.
(15) Pourbaix, M. *Atlas of electrochemical equilibria in aqueous solutions*; Pergamon Press: Oxford, New York, 1966.
(16) Wang, X.; Kunc, K.; Loa, I.; Schwarz, U.; Syassen, K. *Phys. Rev. B* **2006**, *74*, 134305.
(17) Renucci, J. B.; Richter, W.; Cardona, M.; SchÖstherr, E. *Phys. Status Solidi B* **1973**, *60*, 299.
(18) Ferrini, R.; Galli, M.; Guizzetti, G.; Patrini, M.; Bosacchi, A.; Franchi, S.; Magnanini, R. *Phys. Rev. B* **1997**, *56*, 7549.
(19) Klein, P. B.; Chang, R. K. *Phys. Rev. B* **1976**, *14*, 2498.
(20) Demishev, S. V.; Kosichkin, Y. V.; Lyapin, A. G.; Melnik, N. N. *Žurnal ėksperimental'noj i teoretičeskoj fiziki* **1993**, *104*, 2881.
(21) Madelung, O., Rössler, U., Schulz, M. *Group IV Elements, IV-IV and III-V Compounds. Part b - Electronic, Transport, Optical and Other Properties*; Springer Berlin Heidelberg: 2002; Vol. 41A1b, p 1.
(22) Fahrenkrug, E.; Gu, J.; Maldonado, S. *J. Am. Chem. Soc.* **2013**, *135*, 330.
(23) Astrov, D. N.; Razhba, N. A.; Razhba, Y. E. *Meas Tech* **1987**, *30*, 247.
(24) Winnerl, S.; Sinning, S.; Dekorsy, T.; Helm, M. *Appl. Phys. Lett.* **2004**, *85*, 3092.
(25) Birkholz, M.; Fewster, P. F.; Genzel, C.; Wiley Online, L. *Thin film analysis by X-ray scattering*; Wiley-VCH: Weinheim, 2006.
(26) Williams, D. B.; Carter, C. B.; SpringerLink *Transmission Electron Microscopy A Textbook for Materials Science*; Springer US: Boston, MA, 2009.
(27) Brebrick, R. *Metall and Materi Trans B* **1971**, *2*, 3377.

(28) Guo, L.; Searson, P. C. *Electrochim. Acta* **2010**, *55*, 4086.
(29) Bard, A. J.; Faulkner, L. R. *Electrochemical methods: fundamentals and applications*; Wiley: New York, 2001.
(30) Fahrenkrug, E.; Gu, J.; Jeon, S.; Veneman, P. A.; Goldman, R. S.; Maldonado, S. *Nano Lett.* **2014**, *14*, 847.
(31) Ma, L.; Gu, J.; Fahrenkrug, E.; Maldonado, S. *J. Electrochem. Soc.* **2014**, *161*, D3044.
(32) Hansen, M.; Anderko, K.; Institute, I. I. T. R. *Constitution of binary alloys*; McGraw-Hill: New York, 1958.
(33) Ngai, T. L.; Sharma, R. C.; Chang, Y. A. *Bul.l Alloy Phase Diagr.* **1988**, *9*, 586.
(34) Thurmond, C. D. *J. Phys. Chem. Solids* **1965**, *26*, 785.
(35) Dokoumetzidis, A.; Macheras, P. *Int. J. Pharm.* **2006**, *321*, 1.

CHAPTER 6

Conclusions and Ongoing Work

A. Conclusions

This thesis investigates both fundamental and practical perspectives of ec-LLS and demonstrates that ec-LLS can provide a simplistic and cost-effective route in manufacturing covalent semiconductors materials. A fundamental understanding of the individual steps in ec-LLS is essential in further developing and realizing the limitations of this technique. In chapter 2 the competition between heterogeneous and homogeneous nucleation in ec-LLS was analyzed under a variety of processing conditions and the results were used in developing ec-LPE (chapter 3). Further fundamental studies on the individual steps in ec-LLS entailing the characteristics of the zero valent adsorbed species and the dynamics of the dissolution of this species into the liquid metal phase can be analyzed using *in-situ* surface sensitive techniques such as X-ray reflectivity and grazing incidence X-ray diffraction. Studies of this nature could provide the structure of the electrolyte / liq. metal interface during ec-LLS and allow for the early stages of crystal formation to be observed. Coupling these *in-situ* surface sensitive techniques with the potentiometric control of ec-LLS enables a route to study the kinetics of ec-LLS growth and is instrumental in elucidating the mechanism of the ec-LLS growth of group IV and III-V semiconductors. Gaining a better understanding the fundamentals of ec-LLS growth through these studies could enable new applications for ec-LLS and ec-LPE.

In contrast to the established epitaxial growth methods, ec-LPE offers a non-energy intensive route towards growing these technologically relevant semiconductor materials. The crystalline quality of the Ge films grown by ec-LPE is comparable to VPE Ge films grown at high temperatures with highly processed precursors under strictly controlled atmospheres (e.g. ultra-high vacuum environments). However, ec-LPE is conducted at low temperatures (~ 90 ºC) in open atmosphere using benign precursors. Therefore, ec-LPE assumes a unique role in providing a non-energy intensive method for growing epitaxial films of covalent semiconductors. As a result,

if adequately developed, ec-LPE could provide a low-cost 'greener' alternative to growing these epitaxial films.

Aside from the potential practical applications of ec-LPE, the technique challenges pre-conceived notions held on the requisites for epitaxial growth. Prior to ec-LPE, epitaxial growth of covalent semiconductors had only been achieved under stringent O_2 and moisture free conditions at high temperatures (>500 ^{o}C). However, ec-LPE is conducted in an aqueous electrolyte under open atmosphere at low temperatures. Accordingly, the work in this thesis demonstrates that these stringent conditions are not a necessity to grow large area epitaxial films of covalent semiconductors. Since epitaxial growth at these low-temperatures is unprecedented, further study on the energetics of crystal nucleation / growth and influence of experimental parameters (e.g. substrate, applied potential, temperature, precursor concentration and liquid metal thickness) in ec-LPE would be of academic interest.

While ec-LPE has only just been established in this thesis it has the potential of making a serious impact on the semiconductor industry if electronic grade material can be produced. This requires extreme purity and precise control over the dopant character of the resultant film, which ec-LPE currently lacks. One strategy to meet the purity constraint is to use a liquid metal solvent that reduces or eliminates the incorporation of the metal solvent impurity atoms into the crystal. In chapter 4 a new liquid metal solvent (E-BiIn) was employed in hopes of resolving the contamination issue. However, the E-BiIn alloy was unsuccessful in reducing the concentration of impurities incorporated into the crystal. Consequently, further work is needed to find a solvent system to reduce the liquid metal contamination.

Another important aspect in developing this technology is to increase the scope of materials that can be produced by ec-LPE. Naturally, the candidates for new ec-LPE films should follow from materials attainable by ec-LLS, such as GaSb (chapter 5). By simply changing the electrolyte in ec-LPE, prospects of growing additional group IV materials (Si), group III-V (GaAs and GaSb) and heterojunctions thereof, becomes apparent. Another appealing strategy to expand the materials scope of ec-LPE could be to change the composition of the liquid metal electrode to yield ternary and/or quaternary III-V materials (e.g. InGaAs, InGaSb and InGaAsSb). The work thus far in developing new ec-LPE films of Si and GaSb is summarized below.

B. Ongoing Work

i. Si ec-LPE

Si thin films are used as both the substrate and absorber layer in solar cells[1] and the channel in thin film transistors.[2] Si thin films are usually grown through physical vapor deposition (PVD)[3], chemical vapor deposition (CVD)[4,5] or LPE[6] processes at 700 °C.[2] A low temperature deposition process will have two major benefits. First, it allows for lower energy input. Second, it could be compatible with existing device platforms and substrates. The ec-LPE process was first established by growing epitaxial films Ge over macroscopic areas (~ 3.1 cm^2) at 90 °C from an aqueous solution of GeO_2 (Chapter 3). We hypothesize that by using a thin liquid Ga film, Si thin films can be produced via ec-LPE using $SiCl_4$ electrolyte near 100 °C.

As described in chapter 3, Ga film electrodes (10 – 20 μm thick) were created by mechanically compressing Ga liquid metal on a Si substrate using a porous SiC membrane. Figure 6.1a shows the cyclic voltammograms collected at the Ga film electrode of a propylene carbonate (PC) electrolyte with dissolved tetrabutyl ammonium chloride (TBAC) both before and after the addition of $SiCl_4$. After the addition of $SiCl_4$ there was an increase in the cathodic current around -2.3V. This current was attributed to the reduction of $SiCl_4$ (e.g. $Si^{4+} + 4e^- \rightarrow Si^0$) and thus an applied potential between -2.3 and -2.5V was chosen for chronoamperometric depositions (Figure 6.1b). The current transient showed several distinct features that were routinely observed amongst trials. Initially, the current dropped to a local minimum followed by an increase around 500 s. After reaching a local maximum (around 750 s in Figure 6.1b) the current began to gradually decrease until the experiment ended.

Following the deposition, the Si(001) substrate contained a film and/or discrete islands (Figure 6.2). The islands consistently showed a rectangular shape (2-fold symmetry) which was indicative of a deposit with a 001 orientation, similar to the islands observed in Ge ec-LPE (Chapter 3).

Electron backscatter diffraction patterns (EBSDP) were collected from films grown on a Si(111) substrate. The EBSDP's were indexed using Aztec (Oxford Instruments) software and the films were identified as crystalline Si with a (111) orientation (Figure 6.3a). EBSDP were collected over a 10 μm x 10 μm domain and the cumulative orientation data was plotted in the form of pole

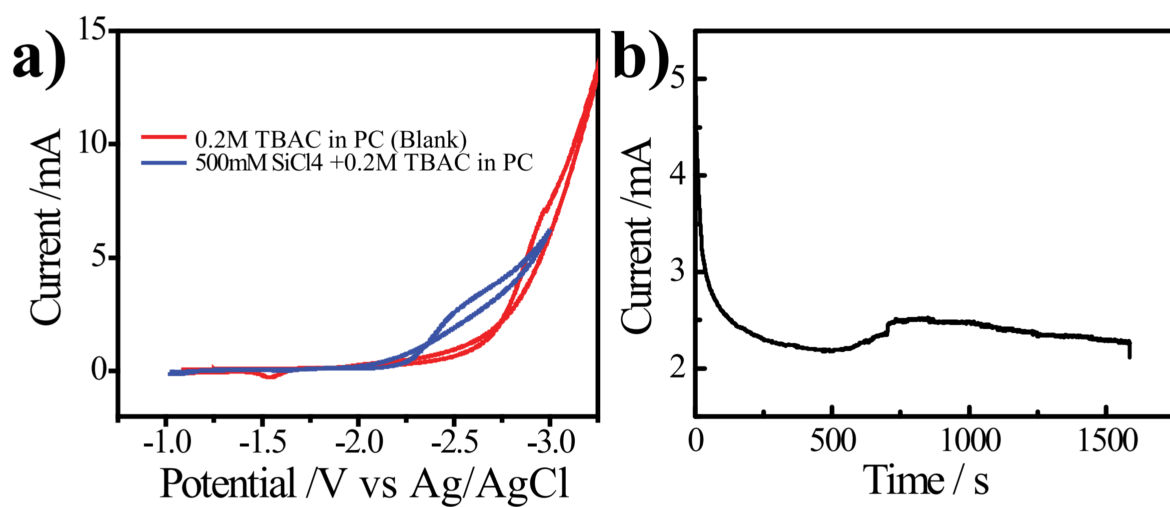

Figure 6.1. (a) Cyclic voltammogram at a Ga film electrode for 0.2M TBAC in PC (red) and after the addition of 500mM $SiCl_4$ (blue). (b) Chronoamperometric response of Ga film electrode with an applied bias of -2.5V vs Ag/AgCl in an electrolyte of 0.2M TBAC and 500mM $SiCl_4$ dissolved in PC.

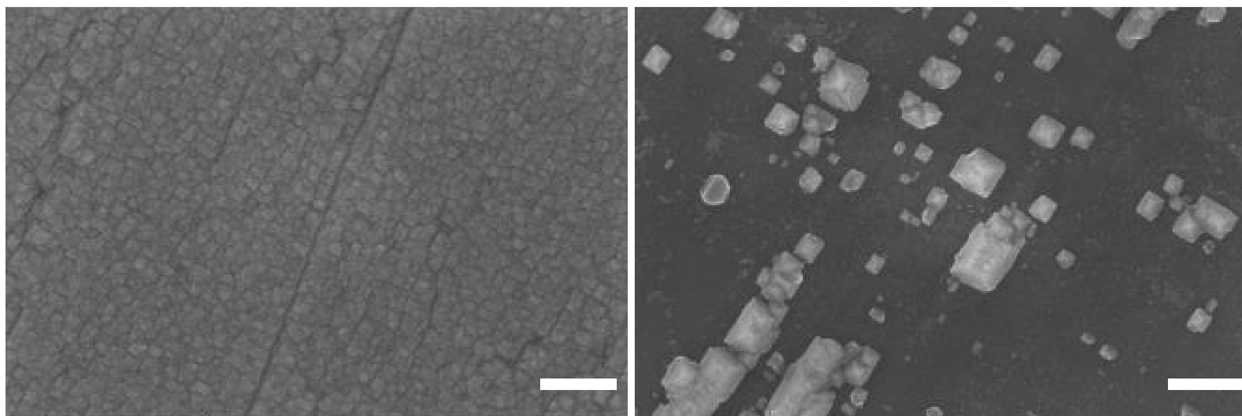

Figure 6.2. Scanning electron micrographs of Si film(left) and islands (right) deposited on a Si(100) substrate at E_{appl} = -2.3 V.

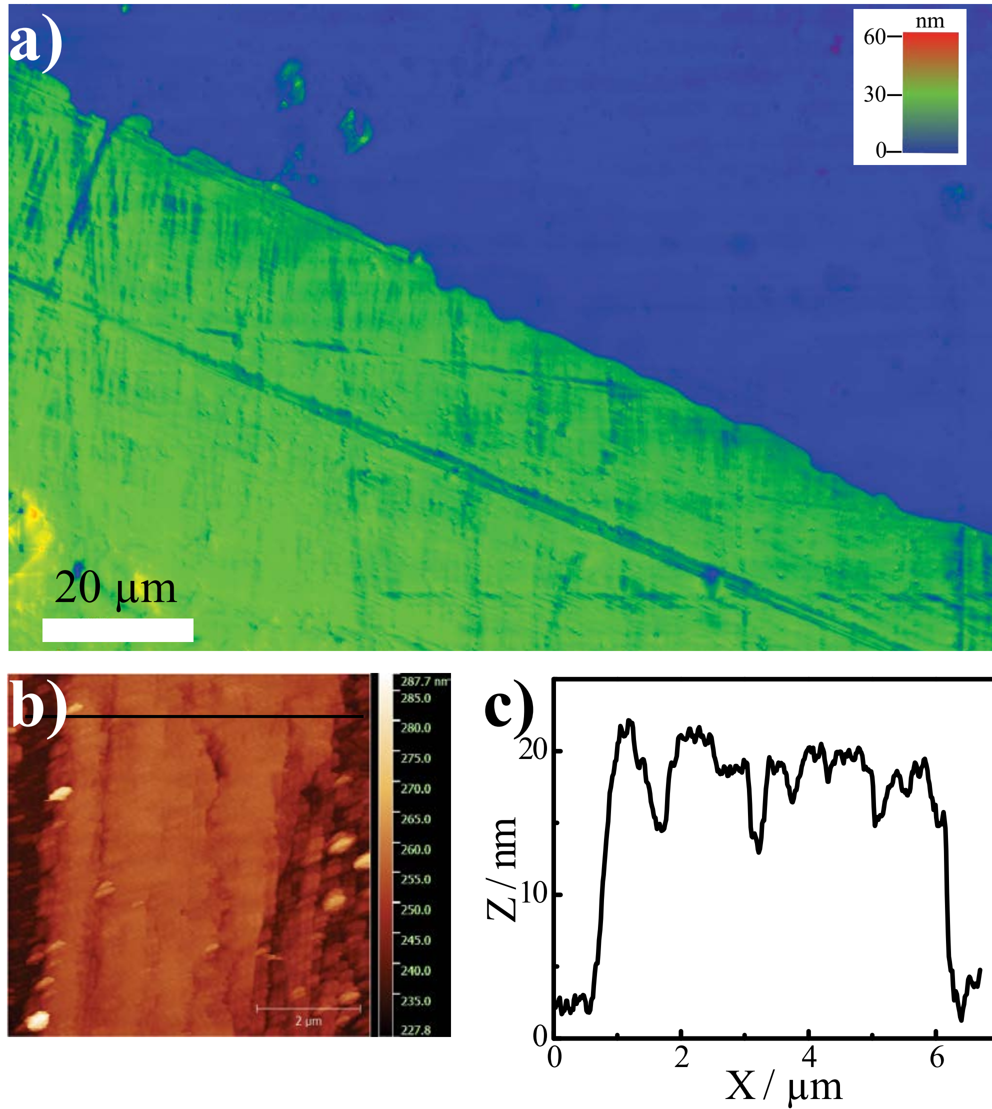

Figure 6.3. Height contrast image (a) collected using a laser confocal microscope of Si film. AFM image (b) and corresponding height profile (c).

figures (Figure 6.3b). Figure 6.3c shows a 2D projection of a cubic crystal oriented along the [111] zone axis. The location of the crystal planes, as shown in the 2D projection (Figure 6.3b), are coincident with the intensity maxima in the corresponding pole figure (Figure 6.3c). Furthermore, since no additional peaks are observed this indicates that the domain is a single crystal.

Optical profilometry and atomic force microscopy (AFM) showed that continuous films could be deposited as thin as 15-20 nm (Figure 6.4a-c). The root mean square (RMS) surface roughness was measured to be ~ 3-4 nm as measured by AFM and optical profilometry. Chronoamperometric depositions were performed for 0.5, 1 and 2 hrs. After 1 hr the thickness of the did not appear to increase. Control experiments where additional $SiCl_4$ precursor was added periodically throughout the deposition also did not increase the thickness suggesting the thickness threshold is not due to depletion of the $SiCl_4$ precursor. The cumulative observations imply there is a blocking of Si^0 from dissolving into the Ga electrode (as in Figure 1.2) preventing further film growth. This remains a problem with Si ec-LPE in that arbitrarily thick films cannot be deposited.

One explanation for the blocking layer could be due to formation of unintended side products brought on by the severe negative E_{appl}. Previously, our lab found that extended periods at sufficiently negative E_{appl} can lead to the formation of a glassy film forming on the liquid metal electrode that prevented further growth of Si by ec-LLS. The composition of the film was found to consist of Si, O and C.[7] While PC has a wide cathodic window, it is apparent from the figure 6.1a that cathodic current is present for the blank electrolyte at the E_{appl} used in Si ec-LPE (-2.3 to -2.5 V) which could indicate the decomposition of the PC solvent. The reduced PC could potentially react with the $SiCl_4$ precursor to yield a silicate species that forms the glassy film.

Two separate control experiments were performed to prevent the formation of or remove the blocking layer. First, ec-LPE experiments were conducted at more positive E_{appl} (-1.8 to -2.3V), however, either there was no Si film growth or no change in the observed Si film thickness. Second, experiments to remove the silicate species *in-situ* were also attempted. Briefly, an organic base, tripropylamine (TPA), was dissolved in PC prior to the ec-LPE experiment. However, no Si film was observed with the addition of TPA.

Crystalline Si thin films have successfully been electrodeposited using ec-LPE but there are still some remaining questions in regard to ec-LPE. Namely, Can arbitrarily thick Si thin films be deposited by ec-LPE ? and, if not, what is the reason ? Can ec-LPE be used to grow SiGe alloys

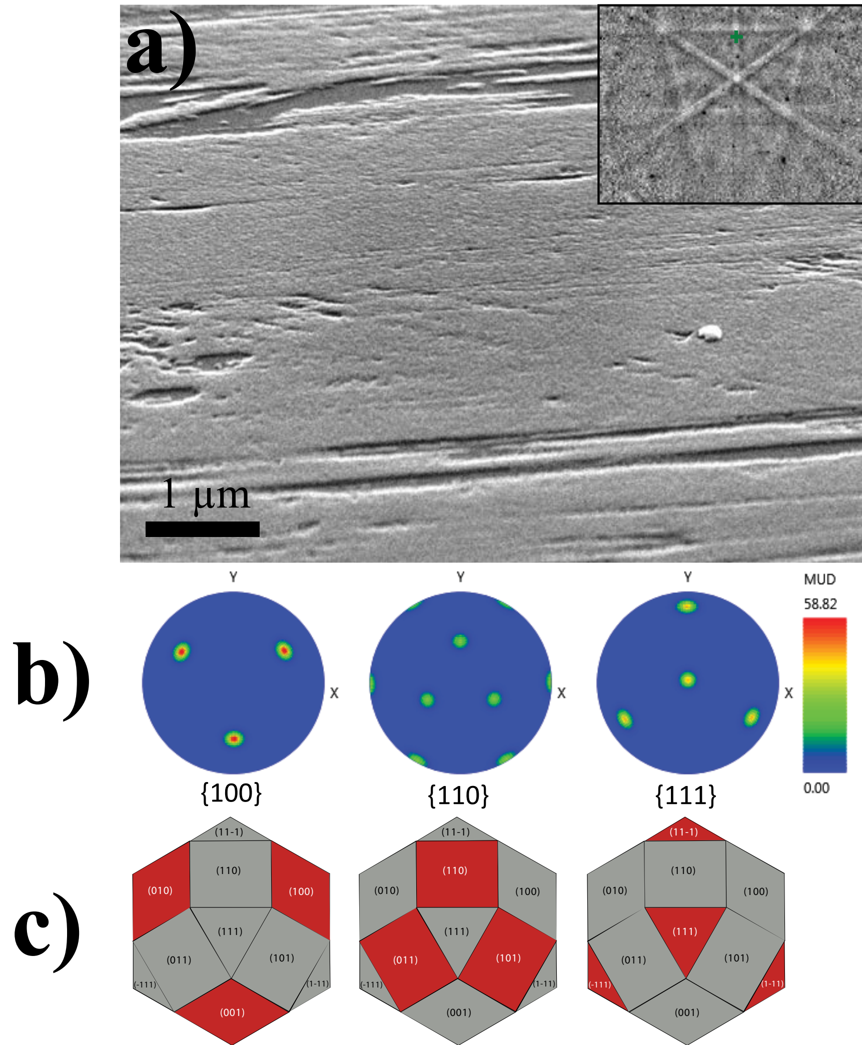

Figure 6.4. Scanning electron micrograph of film grown on an Si (111) substrate (a); inset shows EBSDP. Pole figures (b) plotted from the film in (a) and the expected location of the corresponding crystal planes for a 2D projection down the [111] zone axis (c).

if the electrolyte contains both Si and Ge precursors ? Can continuous films of group III-V materials be deposited using ec-LPE ?

ii. GaSb ec-LPE

Thin films of GaSb are used as both the substrate and active layer thermophotovoltaic devices[8-10] and multi-junction solar cells.[11] However, one bottleneck in scaling up these devices for commercial applications is the high production cost of GaSb epitaxial layers and wafers.[8] Since ec-LLS is capable of producing crystalline III-V semiconductors (Chapter 5), then ec-LPE could provide a low-cost route for producing thin film III-V semiconductor materials. Furthermore, the growth of high purity, optoelectronic grade III-V semiconductor films using Ga liquid metal solvents has already been established at high temperatures (>500 ºC) through LPE.[6] Supporting the notion that these liquid metal solvents are suitable for growing high-quality group III-V semiconductor films.

In chapter 5 the homogeneous growth of GaSb by ec-LLS is detailed using an Sb_2O_3 precursor.[12] However, to make this ec-LLS process compatible with the materials used in ec-LPE thin film cell additional considerations must be accounted for. In chapter 5 a highly alkaline (pH ~ 12-13) was needed to dissolve the Sb_2O_3 precursor. However, this corrosive electrolyte would not be compatible with the PDMS used in to ec-LPE membrane at 90 ºC. As a result, a precursor, $K_3[Sb(tartrate)_2]$ (herein referred to as $Sb(tar)_2$), with a higher solubility at neutral pH was synthesized.[13] The precursor ($Sb(tar)_2$) was formed by dissolving Sb_2O_3 in an alkaline solution and then adding two equivalence of L-tartaric acid. After two recrystallization steps in an ethanol / water solution the product $K_3[Sb(tartrate)_2]$ was formed and the compound was verified by PXRD (using Jade software).[14] $Sb(tar)_2$ was readily soluble in neutral pH (Figure 6.5a,b) and was used for electrodeposition experiments in either a phosphate buffer or sodium borate buffered electrolyte (pH ~ 7 and 8.5, respectively).

The formal reduction potential of $Sb(tar)_2$ was determined by cyclic voltammetry (Figure 6.5c). The experimental electrolyte (100 mM $Sb(tar)_2$ + 10 mM $Na_2B_4O_7$) shows an increased cathodic current when compared to the blank electrolyte (200 mM L-tartaric acid + 10 mM $Na_2B_4O_7$) for $E_{appl} < -0.75$ V. This suggests the increased cathodic current is due to the reduction of Sb^{III} to Sb^0. Therefore, any $E_{appl} < -0.75$ V would be sufficient for chronoamperometric deposition of Sb^0. Initial chronoamperometric experiments on bulk Ga pool electrodes

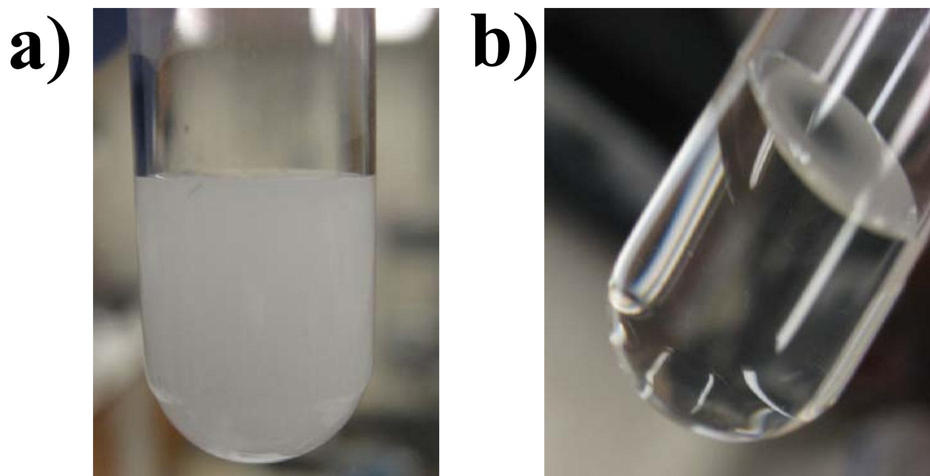

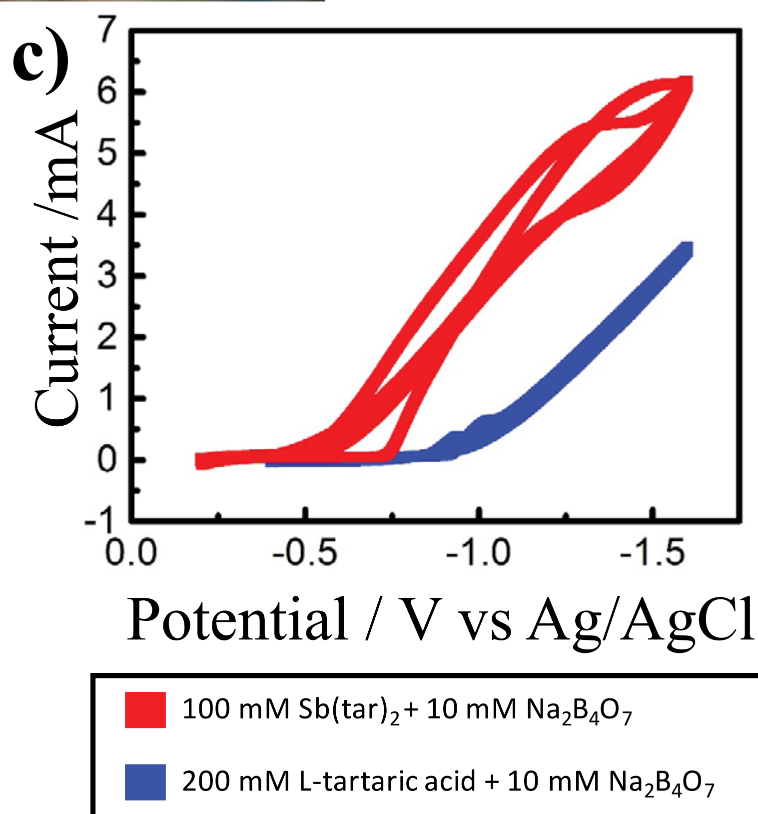

Figure 6.5. Photographs of test tube containing 0.7 mM Sb_2O_3 + 600 mM NaOH (pH ~ 13.5) (a) and 100 mM $Sb(tar)_2$ + 10 mM $Na_2B_4O_7$ (pH ~8.0) (b). Cyclic voltammogram at a Ga electrode of the blank (200 mM L-tartaric acid + 10 mM $Na_2B_4O_7$) and experimental (100 mM $Sb(tar)_2$ + 10 mM $Na_2B_4O_7$) electrolyte.

(E_{appl} = - 1.30V) showed that crystalline GaSb could be formed, via Raman spectroscopy, near neutral pH's with $Sb(tar)_2$. The observed Raman spectra were reminiscent of the chronoamperometric deposition with the Sb_2O_3 precursor in alkaline solutions (Chapter 5) under otherwise identical conditions.

Figure 6.6a shows SEM images of the silicon substrate following chronoamperometric depositions (E_{appl} = -1.30V), using e-GaIn film electrodes, as a function of the $Sb(tar)_2$ concentration. As the concentration of $Sb(tar)_2$ decreases there is a decrease in the material deposited on the surface of the liquid metal (i.e. at the electrolyte/ liquid metal interface) and an increase in the number density of islands that deposit on the underlying Si substrate. For the homogeneous growth of GaSb (Chapter 5) a similar observation was made. If the concentration of the Sb precursor was above 1 mM an excess of Sb^0 accumulated on the surface of the liquid metal instead of dissolving / reacting to form GaSb, as evident by the Raman spectra. Figure 6.6b shows the EDS spectra of the islands deposited on the underlying Si substrate (taken from red box Figure 6.6a). The EDS spectra show that the islands are composed of In, Ga and Sb. Furthermore, the Raman spectra show phonon modes around 170, 225 and 430 cm^{-1} that are consistent with GaSb[14,15] and InSb[16] (Figure 6.6c). The collective observations suggest that to get a continuous heterogeneous deposit of GaSb, a low concentration (< 1 mM) of $Sb(tar)_2$ was required.

However, the if the concentration of $Sb(tar)_2$ is kept low then the electrolyte will become depleted of the precursor at within a short time frame following the applied potential (Figure 6.7a). This was demonstrated using chronocoulometry to calculate the moles of Sb^{3+} reduced as a function of time. From these calculations, the time point at which the electrolyte will be depleted of $Sb(tar)_2$ follows (Figure 6.7a). Control experiments were conducted where the concentration of $Sb(tar)_2$ was continuously replenished by replacing the entire volume of electrolyte after the depletion point had been reached. When the precursor concentration was not replenished (Figure 6.7b) the number density of islands deposited on the substrate were consistently less than when the $Sb(tar)_2$ precursor was replenished (Figure 6.7c). This observation implied that by keeping the concentration of $Sb(tar)_2$ constant (at 0.1 mM) throughout the deposition the density of the islands would increase and would be more amenable to forming a continuous film. However, to keep the concentration consistent throughout the deposition further modifications to the ec-LPE cell were needed.

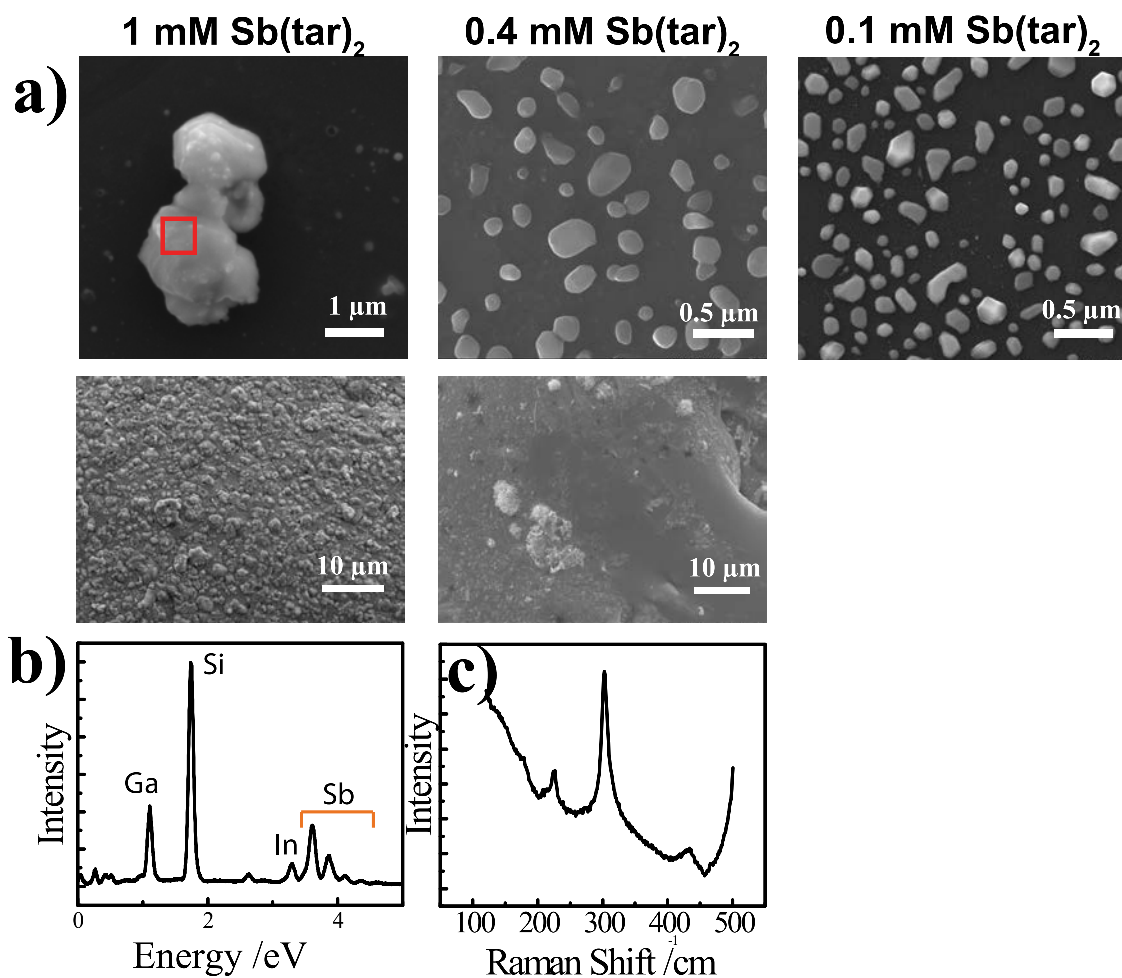

Figure 6.6. Scanning electron micrographs of GaSb ec-LPE with a E-GaIn electrode at $Sb(tar)_2$ concentrations of 1, 0.4 and 0.1 mM (a). Top panel shows SEM islands that formed on underlying substrate and bottom panel shows SEM of liq metal surface after deposition. EDS (b) and Raman spectra (c) of the islands that formed on the substrate where the EDS was taken from the location shown in (a) by the red box.

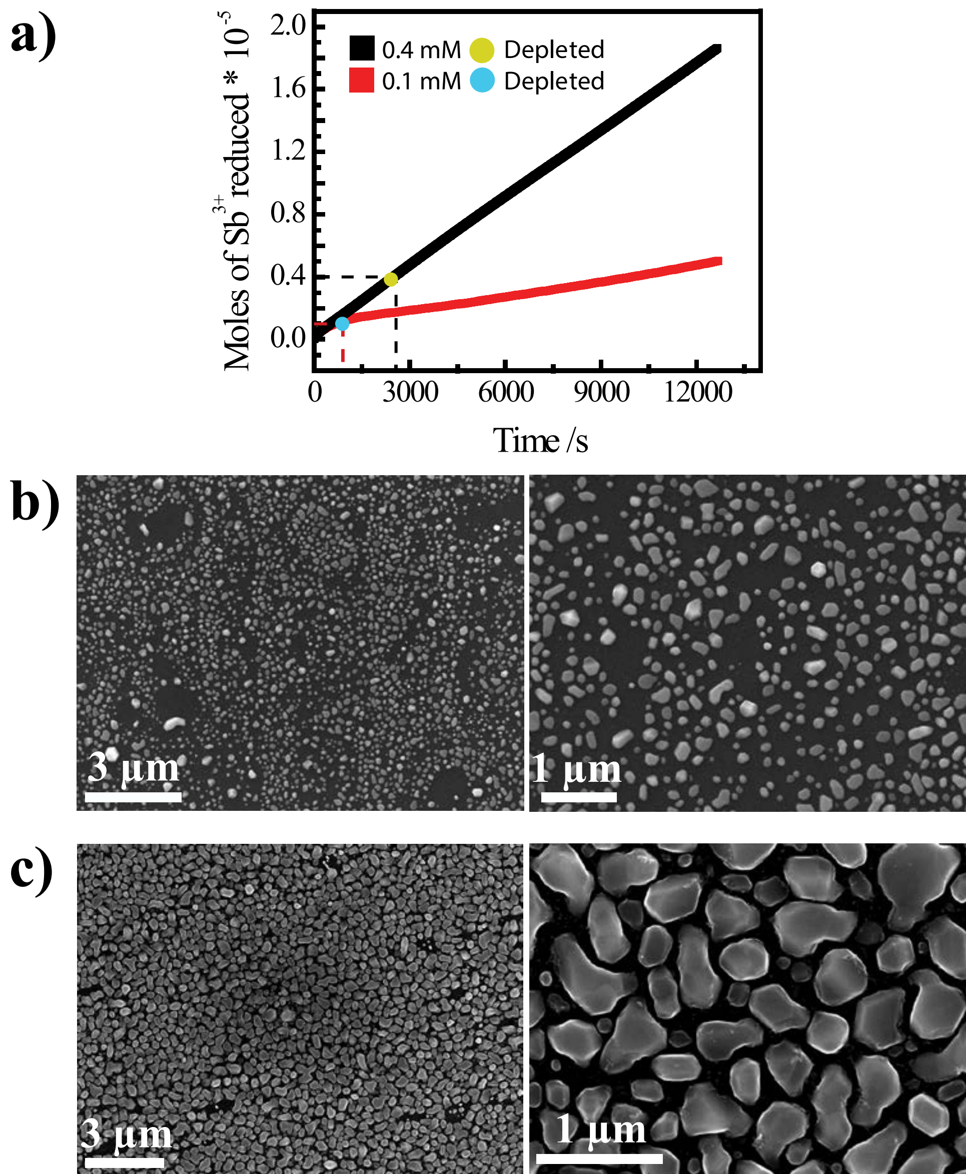

Figure 6.7. Moles of Sb^{3+} reduced as a function of time (a) for chronoamperometric depositions with 0.4 and 0.1 mM $Sb(tar)_2$. The point at which the electrolyte becomes depleted of $Sb(tar)_2$ is indicated for each concentration. Scanning electron micrographs of underlying substrate after ec-LPE deposition for 3 hrs in 0.1 mM $Sb(tar)_2$ (b). Under identical conditions the entire volume of the electrolyte was replaced (c) to replenish the $Sb(tar)_2$ concentration.

Figure 6.8a-c show the ec-LPE flow cell that was used to keep the concentration of $Sb(tar)_2$ constant at 0.1 mM. A peristaltic pump was used to flow a heated electrolyte (0.1 mM $Sb(tar)_2$ +100 mM $Na_2B_4O_7$), contained in a separate beaker, into the bottom of the electrolyte cell reservoir in the ec-LPE cell. A separate pump then removed the spent electrolyte at the top of the cell. Figure 6.9a, b detail the results of using the ec-LPE flow cell. The SEM image (Figure 6.9a) shows that the deposits have coalesced into a continuous film. Raman spectra taken of the films showed a sharp peak near 226 cm^{-1} which is consistent with the TO mode of crystalline GaSb.[14]

Despite depositing a film, a significant amount of excess Ga remained adhered to the surface (Figure 6.10a). In Ge ec-LPE (Chapter 3) the remaining liquid metal could be removed using a selective anodic etch or a by extended periods of sonication in an acidic solution. These two methods were not applicable for removing Ga adhered to the surface of the GaSb films. Finding a selective etch to remove Ga but leave the GaSb film intact remained difficult due to the similar etch chemistries and extended periods of ultra-sonication removed both the excess Ga and the GaSb film. The methods attempted to selectively remove the Ga are summarized in table 6.1. Mechanical methods of removing the Ga either did not completely remove the liquid metal or removed the GaSb film as well as the liquid metal. This suggests the films were less adherent to the Si substrate in comparison to Ge (Chapter 3) which could be attributed to the ~12% lattice mismatch between GaSb and Si compared to the 4.2% mismatch between Si and Ge. Therefore, to make the films more adherent a lattice matched substrate (e.g. InAs and AlSb) could be used in the GaSb deposition. To further characterize the structural and electrical characteristics of the film the excess liquid metal must be removed.

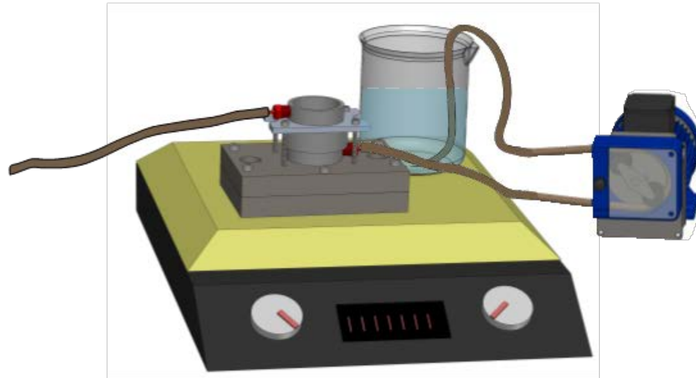

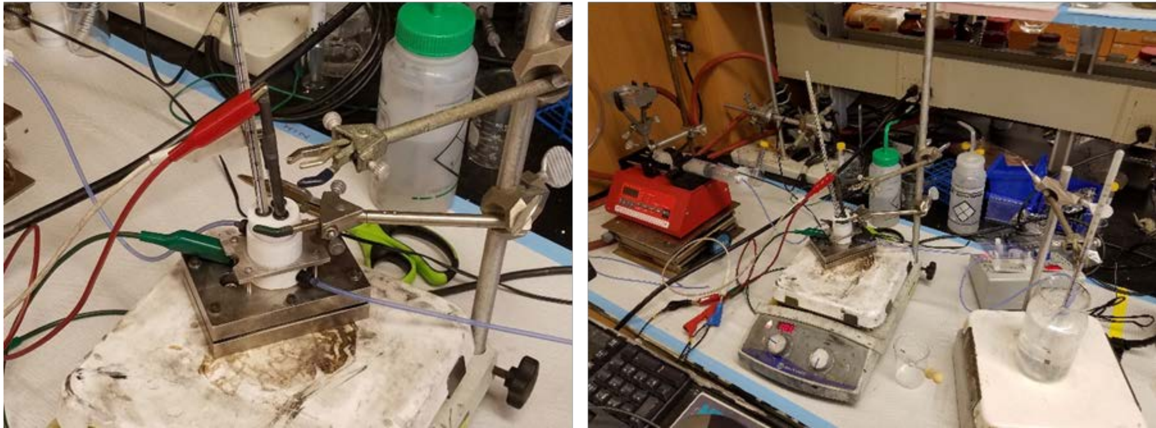

Figure 6.8. Thin film flow cell used for deposition of GaSb. (a) Schematic, (b) and (c) optical photographs of actual setup during a deposition.

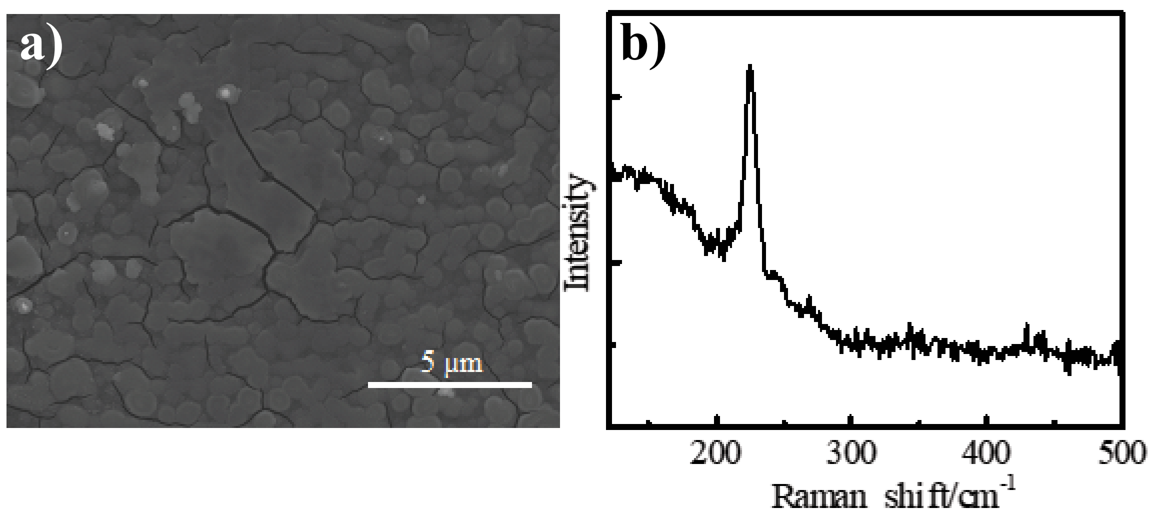

Figure 6.9. Scanning electron micrograph (a) and Raman spectra (b) of films obtained from the deposition in the thin film flow cell.

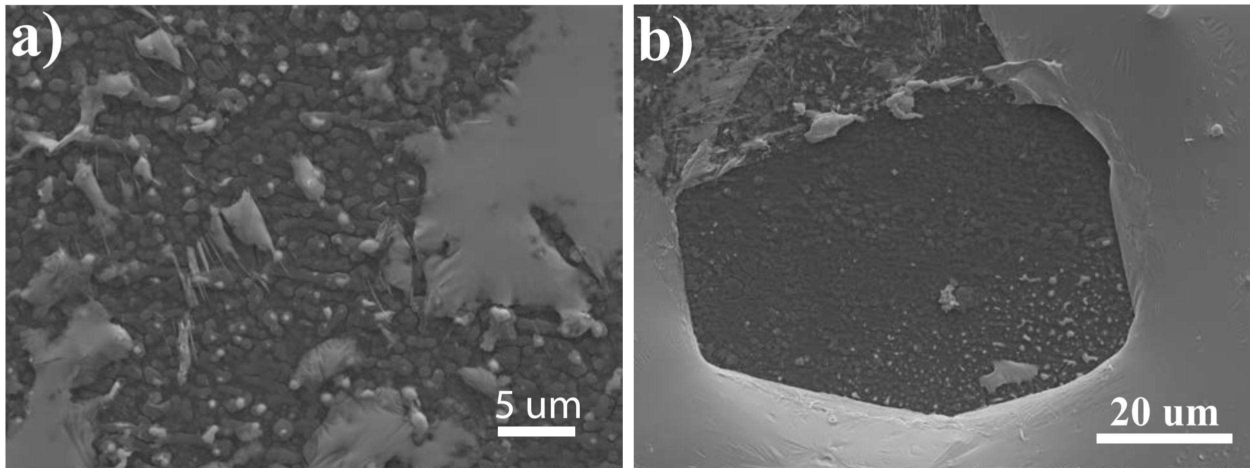

Figure 6.10. Scanning electron micrographs of the GaSb films covered in liquid Ga after the deposition in the thin film flow cell.

Table 6.1. Methods attempted to selectively remove excess Ga(l)

Method	Description	Results
Mechanically wiped	Used lint free cloth soaked in MeOH to mechanically wipe the liquid metal.	Some of the GaSb film remained but residual Ga remained as well.
Sonication	Sonicated film in water and separately in 0.1M HCl	Both methods completely removed GaSb film
Acid etching	Etched in acid. Also applied anodic potential while in acid	Both methods completely removed GaSb film
Al alloy trick	Altered reactivity of liquid metal by alloying with Al then soaked in water. Repeated cycle until no more alloy could be removed.	Method removed some of the liquid metal but left residual impurity.

C. References

(1) Shah, A.; Torres, P.; Tscharner, R.; Wyrsch, N.; Keppner, H. *Science* **1999**, *285*, 692.
(2) Xiao, H.; Society of Photo-optical Instrumentation, E. *Introduction to semiconductor manufacturing technology*; SPIE: Bellingham, Wash. (1000 20th St. Bellingham WA 98225-6705 USA), 2012.
(3) Hirayama, H.; Tatsumi, T.; Ogura, A.; Aizaki, N. *Appl. Phys. Lett.* **1987**, *51*, 2213.
(4) Meyerson, B. S. *Appl. Phys. Lett.* **1986**, *48*, 797.
(5) Wolkow, R. A. *Phys. Rev. Lett.* **1995**, *74*, 4448.
(6) Capper, P.; Mauk, M.; Wiley Online, L. *Liquid phase epitaxy of electronic, optical, and optoelectronic materials*; Wiley: Chichester, England ; Hoboken, NJ, 2007.
(7) Gu, J., University of Michigan, 2014.
(8) Mattarolo, G. *Development and Modelling of a Thermophotovoltaic System*; University Press: Kassel, 2007.
(9) Wang, C. A.; Choi, H. K.; Ransom, S. L.; Charache, G. W.; Danielson, L. R.; DePoy, D. M. *Appl. Phys. Lett.* **1999**, *75*, 1305.
(10) Juang, B.-C.; Laghumavarapu, R. B.; Foggo, B. J.; Simmonds, P. J.; Lin, A.; Liang, B.; Huffaker, D. L. *Appl. Phys. Lett.* **2015**, *106*, 111101.
(11) Laghumavarapu, R. B.; Moscho, A.; Khoshakhlagh, A.; El-Emawy, M.; Lester, L. F.; Huffaker, D. L. *Appl. Phys. Lett.* **2007**, *90*, 173125.
(12) DeMuth, J.; Ma, L.; Fahrenkrug, E.; Maldonado, S. *Electrochim. Acta* **2016**, *197*, 353.
(13) Palenik, R. C.; Abboud, K. A.; Palenik, G. J. *Inorg. Chim. Acta* **2005**, *358*, 1034.
(14) Demishev, S. V.; Kosichkin, Y. V.; Lyapin, A. G.; Melnik, N. N. *Zurnalėksperimentalńoj i Teoretičeskoj Fiziki* **1993**, *104*, 2881.
(15) Klein, P. B.; Chang, R. K. *Phys. Rev. B* **1976**, *14*, 2498.
(16) Pinczuk, A.; Burstein, E. *Phys. Rev. Lett.* **1968**, *21*, 1073.